Dynamics of hard and soft colloids at aqueous interfaces

Louis Keal

THÈSE DE DOCTORAT
DE L'UNIVERSITÉ PIERRE ET MARIE CURIE

Spécialité

Physico-chimie des matériaux

(ED 397)

Préparée aux LABORATOIRES :

SCIENCES ET INGÉNIERIE DE LA MATIÈRE MOLLE (UMR 7615)

Pour obtenir le grade de

DOCTEUR de l'UNIVERSITÉ PIERRE ET MARIE CURIE

Dynamics of hard and soft colloids at aqueous interfaces

Présentée par

Louis Keal

le 17 Novembre 2016

devant le jury composé de :

Mme	**VON KLITZING**	**Regine**	**Rapporteur**
M	**BENYAHIA**	**Lazhar**	**Rapporteur**
M	**TROMP**	**Hans**	**Examinateur**
Mme	**RAVAINE**	**Valérie**	**Examinateur**
Mme	**ROZES**	**Laurence**	**Examinateur**
Mme	**MONTEUX**	**Cécile**	**Directrice de thèse**

Contents

Chapter 1

Introduction

Emulsions in industry and the home

As most schoolchildren will know, when oil and water are brought together, they don't mix. But add the right third ingredient, ordinary washing up liquid for instance, and you can obtain something like a mixture. In fact, droplets of oil are now suspended within the water, with soap molecules sitting at the interfaces between the two, stabilising the interface. It's this stabilisation that allows oils to be washed away, and dishes to be cleaned. But stabilisation and destabilisation of emulsions are important in a huge variety of products and situations. Pharmaceuticals, cosmetics and personal hygiene products very frequently contain emulsions that must last without separating for many months between uses. In petrochemical oil recovery, a strong, stable emulsion is desired that can be transported at high pressures, but that can be destabilised on demand to extract the oil. In food, emulsions contribute a great deal to texture, for instance in yoghurt, mayonnaise and ice cream. These emulsions must be stable on the shelf, but not too stable on the tongue so the flavours and textures in the oil are experienced.

In each system and each situation, different properties are desired from the stabilisers used. Some foods, such as yoghurt and sauces, require only a few days' stability before other components will expire. Some however such as long-life milk might be expected to last many months. In medicine, targeted delivery of an encapsulated substance is sometimes needed, in which case the stabiliser must allow the emulsion to be destabilised on demand.

The first part of this thesis examines just such a stabiliser - soft polymer microgel particles that form strong emulsions, but shrink when heated, destabilising the emulsion.

But sometimes, the properties of an emulsion are desirable in a system, but the presence of an oil phase is not. For instance in seeking to make low-calorie foods, oils are high in calorific content, but are sorely missed if simply not included. Alternative methods for providing an oil-in-water-like texture from more healthy components are being sought. One candidate for such a system is a 'water-in-water' emulsion formed from non-mixing aqueous polymer solutions. However, unlike oil-water emulsions where each phase consists of sub-nanometre scale molecules which should always be smaller than any stabiliser molecule used, a non-mixing polymer solution will be formed of polymer chains many tens to hundreds of times the size of water or oil molecules. As such, large stabilisers must be used. Solid particles have been known to stabilise emulsions for over a century [86, 91], and can be much larger than surfactant stabilisers. They are therefore excellent candidates for

stabilising such systems, but little is known about their behaviour in such complex systems. The second part of this thesis focuses on the behaviour of model spherical particles in a non-mixing aqueous polymer solution to better understand how particles behave and what influence they may have upon the emulsions formed from such systems.

Microgels: Soft stabilisers

Micron-scale balls of cross-linked polymer, swollen with water, are called microgels. The properties of microgels depend upon the properties of the polymers they are made from. If a polymer that goes to the oil/water or air/water interface is used, a so-called 'surface active' polymer, the microgels will also be surface active. Additionally, if the polymer can respond to temperature or other stimuli, the microgel will respond likewise. Microgels formed from Poly-n-isopropyl-acrylamide (PNiPAM) unite both properties, stabilising emulsions very well, but shrinking and destabilising upon increasing the temperature above a 'volume phase transition temperature' (VPTT) of around 33 °C. These properties, along with the temperature's proximity to body temperatures, make such microgel-stabilised emulsions of great interest for a variety of applications from oil recovery to drug delivery.

However, microgels are also more complex than simple molecular surfactants, and understanding how to most effectively make emulsions from them or predicting the stability and other properties of microgel-stabilised emulsions therefore requires that we study the behaviour of microgels in these systems. Specifically, how the thin films that form when droplets approach each other interact and drain, and how microgels from each opposing interface interact, can determine the flow properties and stability of emulsions under mechanical disturbance. Other works have examined microgel emulsions through freeze-drying and fracturing samples, and studying the structure of microgel layers with electron microscopy [29, 30]. But little was known about the dynamic behaviour of such films.

In this thesis, the drainage dynamics of microgel-stabilised thin films in air are revealed using white light reflectometry. The influence of the microgel concentration is explored. Additionally, Destribats et al. showed that the softness of the microgel has an influence on emulsion stability - softer, less crosslinked microgels stabilise emulsions more effectively. To understand the origin of this effect, we studied two different cross-linking densities of microgel.

Water-in-water emulsions

As mentioned above, the second focus of this thesis is the stabilisation of novel 'water-in-water' emulsions with solid colloidal particles. Some recent studies [81, 111] have successfully used colloidal particles to stabilise such emulsions, however in each case the particle used was quite complex (not as simple as a model sphere), so deep-level understanding of particle dynamics and behaviour in such systems is difficult. In this work, we sought to stabilise a water/water system consisting of food-grade biopolymers fish gelatin and dextran using spherical colloidal particles, and in the process gain understanding of the general behaviour and interactions of these particles.

Aside from emulsions, another key scientific application of water/water interfaces and systems is that they can exhibit many of the same phenomena as oil/water interfaces, but at much slower timescales and larger lengthscales. This is due to the fact that surface tension in such systems, the

driving force for many of the phenomena, is far smaller than in oil/water systems. Also, viscosity is often higher. Many behaviours too fast and/or too small to observe at the oil/water or air/water interface become experimentally accessible with a water/water system. Examples include the use of a non-mixing polymer/colloid system to directly observe capillary waves (the thermal fluctuation of an interface) [3, 25], or the rupture of a thin film separating droplets [3].

Also too fast for complete experimental observation in oil/water systems are the dynamics of adsorption of spherical particles to the interface. Or to put it another way, the velocity of a particle after breaching an interface as it finds equilibrium height through the interface, which is determined by its relative preference for each phase. When creating a solid-stabilised emulsion, the dynamics of adsorption are very important, as the forces experienced by particles due to the mixing of emulsification are typically much smaller than the capillary driving force [117], meaning that the particles' adsorption to the interface cannot be sped up by vigorously mixing the emulsion. Recently, Kaz et al. observed experimentally that colloidal particles' relaxation to their equilibrium height through the oil/water interface is unexpectedly slow [62], which they explained with a model based on thermal hopping of the contact line over nanoscale surface defects. Colosqui et al. used theory and simulations to improve upon this model, with the result that they predict two stages of this adsorption motion. The first stage, called 'snap-in', is dominated by capillary forces and occurs extremely quickly. The second stage is far slower and is dominated by surface effects, and it is this stage that Kaz et al. were able to observe. At the oil/water interface, for a typical colloidal particle this 'snap-in' stage is over in less than a microsecond.

In this work, we capture for the first time with particle tracking techniques the 'snap-in' phase of a colloidal particle, using the same fish gelatin/dextran system mentioned above. Additionally, we observe a transition to a slower stage of dynamics, as expected from the model. However, due to the different length scales, time scales and surface tension between the two systems, the origin of these slower dynamics cannot be precisely the same as at the oil/water interface. This in fact serves to give us more clues about the behaviour of particles in the water/water system.

In this thesis

In Part I, we introduce the key concepts, background knowledge and previous work necessary for understanding the results of this study. Chapter 2 covers thin liquid films, their thermodynamics and drainage. Chapter 3 introduces the physics of particles at interfaces, beginning with hard particles such as the spherical colloids used in the water/water experiments, including an overview of the current understanding of adsorption dynamics as discussed above. Then soft particles are introduced including the previous studies into PNiPAM microgels at interfaces. Chapter 4 introduces water/water emulsions, beginning with the thermodynamics of demixing, and continuing to a discussion of the specific properties of the fish gelatin/dextran system. Finally the current results in stabilising such systems are summarised. At the end of this part, the objectives of the project will be provided in greater detail.

Part II presents the work with PNiPAM microgel thin films, beginning in Chapter 5 with an introduction to the experimental techniques and materials used, including the thin film balance technique used to study film drainage. Chapter 6 presents the results of the work, first discussing

the ‘soft’ microgels with a low crosslinking density, then comparing that to the ‘hard’ microgels. For each crosslinking density, a ‘high’ and a ‘low’ concentration case are considered.

Part III covers the results exploring colloidal particles in the water/water system. Chapter 7 introduces the materials and methods used. Measurements of the viscosity and calculations for the surface tension of the polymer systems are found in Section 7.4. Then Chapter 8 introduces particles to the picture, including particle/polymer phase contact angles, polymer adsorption measurements and particle aggregation results. Attempts to stabilise the fish gelatin/dextran system with colloidal particles are detailed in Chapter 9. Finally Chapter 10 presents and examines the results of the tracking of particle adsorptions. The models fitted to the trajectories are explored, and at the end of the chapter some discussion of the implications of the results is given.

Some general conclusions are presented at the end of the thesis, and some follow-up experiments are suggested. This is followed by appendices which include lists of figures and tables.

Part I

State of the Art

Introduction

In Part I, we will introduce the most important and relevant background, theory and published work relating to the topics of this thesis. There are three key topics; the drainage dynamics of thin films in emulsions and foams, the behaviour of soft and hard colloidal particles at fluid/fluid interfaces, and the properties of aqueous two-phase systems (ATPS) and attempts at using them to make 'water-in-water emulsions'.

Chapter 2 will introduce the key concepts of thin liquid films. Namely, it will explain interfacial tension, disjoining pressure isotherms, and explain relevant theories for the drainage of thin films.

Chapter 3 adds colloidal particles to the picture, explaining their behaviour at interfaces. Firstly hard particles are explored, specifically spherical particles. The energy required to remove such a particle from the interface is large, as is explained in this chapter. This strong adsorption is also used to stabilise so-called 'Pickering' emulsions, the properties, advantages and disadvantages of which are described. Finally, the dynamics of particles as they adsorb to fluid/fluid interfaces are explored with both experimental and theoretical works.

Chapter 4 introduces the ATPS, firstly briefly explaining the thermodynamics that allow non-mixing polymer solutions or polymer-colloid solutions to coexist. Then some examples of non-mixing polymer solutions and non-mixing polymer/colloid solutions are shown. Further, the specific non-mixing polymer pairing experimentally studied in this work is thoroughly examined, namely non-gelling fish gelatin and dextran, with both theorertical and experimental works. Finally the current state of attempts to stabilise ATPSs with the Pickering mechanism introduced earlier is shown.

Chapter 2

Liquid interfaces and thin films

Contents

This chapter will introduce the key concepts in the theoretical understanding of liquid interfaces and thin liquid films, as well as the key experimental techniques for creating, controlling and examining thin liquid films.

2.1 Interfacial Tension

When one fluid phase meets another and does not mix, an interface will be formed between the two phases. For example, oil and water, or air and water. Depending on the miscibility of each phase in the other and the size of the component molecules, this interface, representing the transition in composition from one phase to the other, can be broad ($\gtrsim 10\,\text{nm}$) or narrow ($\sim 1\,\text{Å}$).

Within the bulk of each phase, there are interactions between neighbouring molecules. As each molecule is surrounded on all directions, these interactions are symmetrical. At the interface however, molecules no longer have neighbours of their own phase in one direction. This results in an imbalanced force at the interface, which has a free energy cost per unit area, γ, as illustrated in Figure 2.1. To minimise this cost, systems tend to minimise the surface area of their interfaces.

This minimisation of area gives droplets their spherical shape, and defines the structure of foams.

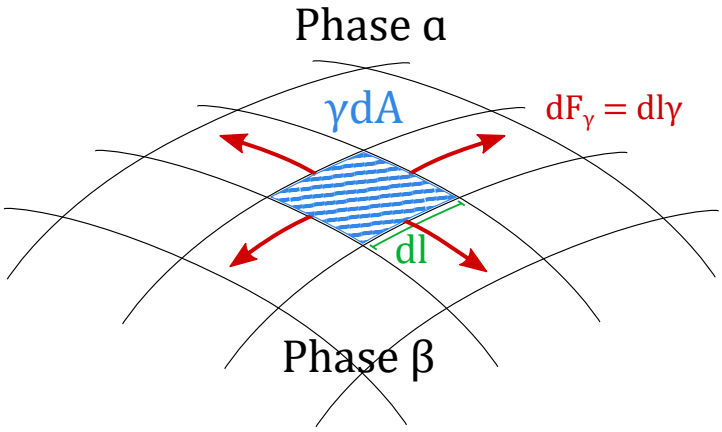

Figure 2.1: Interface between phases α and β. The free energy cost of the interface for an infinitesimally small area $dA = dl \times dl$ is γdA. Alternatively, every point along the perimeter of dA experiences a force per unit length of γ in the direction parallel to the interface, perpendicular to dl. The force experienced by each line is therefore $F_\gamma = \gamma dL$.

2.2 Disjoining Pressure

In an emulsion or a foam, when two droplets or bubbles approach each other, a thin film is formed between the two interfaces. There are forces, both attractive and repulsive, that act between the interfaces. The sum force of all their contributions, per unit area, is called the disjoining pressure. Convention dictates that this pressure is given the direction opposing the approach of the interfaces, else 'conjoining' pressure would be described.

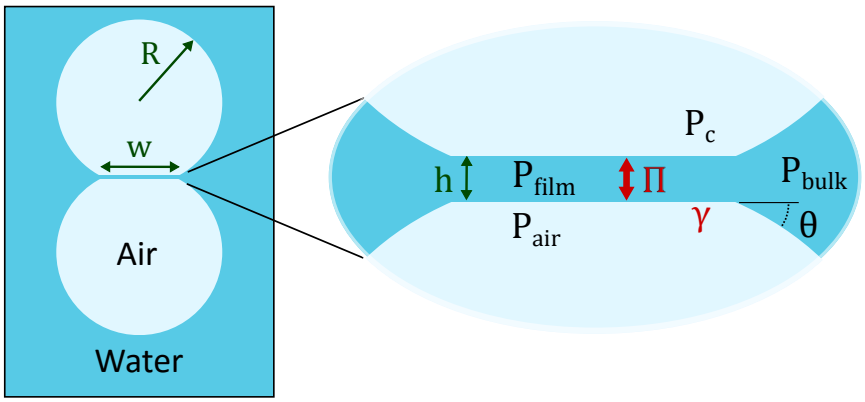

Figure 2.2: Schematic of a thin film between air bubbles in water, however water droplets in oil or oil droplets in water would show the same definitions. R is the droplet radius, w the film width and h the film thickness. P_{film}, P_{bulk}, P_{air} and P_{c} are the pressures in the film, within the bulk solution, in the air and at the plateau border due to the interfacial curvature, respectively. Π is the disjoining pressure, γ the interfacial tension and θ the contact angle in the plateau border.

The forces experienced by molecules at a single interface, ie. the forces that cause surface tension, derive from the environment around molecules at interface differing from around molecules in bulk. As a film becomes sufficiently thin, the environment around molecules even in the bulk of

the film starts to be affected, as the regions that are close to an interface begin to overlap. To make the film thinner would require work. This contributes to the disjoining pressure.

2.2.1 Thermodynamics of the thin film

The Gibbs free energy of the thin film of surface area A and thickness h is given by Eriksson and Toshev [34]:

$$dG_{\text{film}} = -S_{\text{film}}dT + Ah\,dP_{\text{bulk}} + 2\gamma dA - \Pi A\,dh + \sum_i \mu_i dn_i \tag{2.1}$$

γ is the film surface tension, S_{film} is the excess entropy of the two film interfaces, and μ_i is the chemical potential of the ith component.

The thermodynamic definition of the disjoining pressure then is the rate of change of this free energy, per unit area of the film, with changing film thickness [6, 34]:

$$-\left(\frac{\partial(G_{\text{film}}/A)}{\partial h}\right)_{T,P_{\text{bulk}},A,n_i} = \Pi(h) \tag{2.2}$$

2.2.2 Disjoining Pressure Isotherm

The variation of disjoining pressure Π with film thickness h is known as the disjoining pressure isotherm. The theoretical shape of this function is quite well known, and has many contributing factors. When calculating the disjoining pressure, these factors are commonly represented as additive components, as in:

$$\Pi(h) = \Pi_{\text{dl}} + \Pi_{\text{VdW}} + \Pi_{\text{steric}} + \Pi_{\text{supra}} + ... \tag{2.3}$$

where the subscripts represent: dl = electrostatic double layer forces, VdW = Van de Waals forces, steric = steric forces e.g. from surfactant head groups within the film, supra = supramolecular structuring forces e.g. surfactant micelles or self-assembled layers. The assumption of additive components is usually, but not always, valid - anomalous results are sometimes recorded [8, 9].

The first two components, Π_{dl} and Π_{VdW} are modelled by DLVO theory, named for Derjaguin, Landau, Verwey and Overbeek, which describes the interaction of charged surfaces through a liquid, summing van der Waals attraction and the electrostatic repulsion due to the double layer of counterions that form at charged surfaces.

Considering first this electrostatic double layer component, as illustrated in Figure 2.3, its range will be determined by the characteristic length of the decay of the electrostatic potential from the ions at interface, due to screening of the charge by electrolyte. This is given by the Debye length λ, which from classic Debye-Hückel theory is given by [18]:

$$\lambda = 1/\kappa = \sqrt{\frac{\epsilon k_{\text{B}} T}{8\pi n_0 e^2}} \tag{2.4}$$

where n_0 is the number density of ions, e the elementary charge, ϵ the dialectric constant of the medium, and $k_{\text{B}}T$ is Boltzmann's constant multiplied by temperature (the thermal energy). An

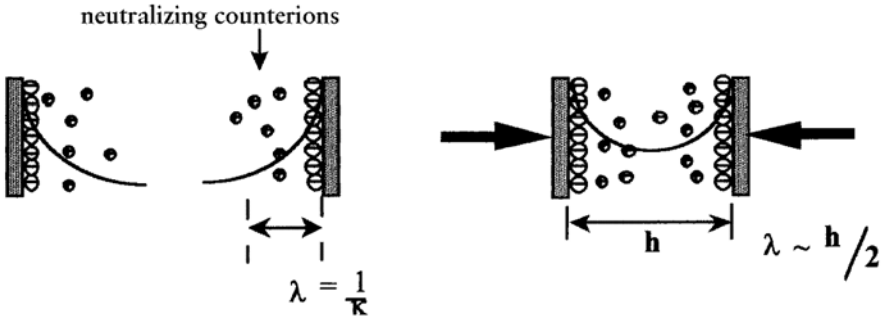

Figure 2.3: Schematic of counterion layer formation near charged surfaces, from [12]. The surfaces begin to interact electrostatically when their separation, h, becomes similar to twice the Debye length, λ.

important result from this is that the decay length of this force decreases as electrolyte concentration increases, ie. increased salt or other electrolyte concentration reduces the range of the double layer force.

To calculate the strength of the force, linear Poisson-Boltzmann relations can be used for small surface charges, and for small potentials and large separation distances the following result is found [54]:

$$\Pi_{\mathrm{dl}} = 64 n_0 k_{\mathrm{B}} T \gamma^2 \exp(-\kappa h) \tag{2.5}$$

where κ is the inverse Debye length, $1/\lambda$.

The van der Waals component is calculated according to the Hamaker method [49], based on pairwise summation of the individual attractions between molecules. In a simple model, two plane-parallel surfaces are separated by a force

$$\Pi_{\mathrm{VdW}} = -\frac{A_{\mathrm{H}}}{6\pi h^3} \tag{2.6}$$

where A_{H} is the Hamaker constant, which depends upon the refractive indices and permittivities of the phases, and is typically within the order of 10×10^{-20} J for foam films. This can be calculated with Lifshitz theory [69].

Combined together, these elements comprise DLVO theory. The shape of the resulting disjoining pressure isotherm $\Pi(h)$ determines the interaction. If a decrease in thickness results in a decrease of the repulsive pressure (increased attraction), then the thinning will accelerate. Therefore, the film thickness is then stable only when total pressure Π plus any applied pressure is zero (hence no net force), and $d\Pi(h)/dh$ is negative.

However without a steric contribution term Π_{steric} as would be contributed by surfactants, as h approaches 0, $\Pi(h)$ is strongly negative due to the dominating van der Waals contribution. This means the film would rupture as its thickness becomes small. Steric or entropic forces provide a strong barrier against this thinning, as illustrated in Figure 2.5. When steric, short-range forces are taken into account, $d\Pi(h)/dh$ is negative at small h, as shown in Figure 2.4, which plots the contributions of the three terms.

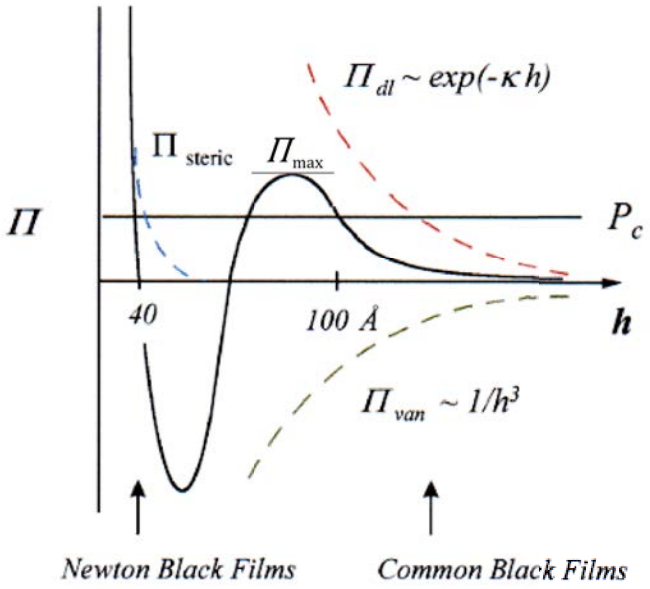

Figure 2.4: Schematic representation of a disjoining pressure isotherm $\Pi(h)$, including contributions from Pi_{steric}, Π_{dl} and Π_{VdW}, adapted from [12]. Π_{max} is the maximum pressure of the peak and P_c is the applied pressure due to curvature in the plateau border.

2.2.2.1 Common and Newton Black Films

The pressure shown P_c is the applied pressure, in this case the pressure due to the curvature in the plateau border, shown in Figure 2.2. The applied pressure changes the equilibrium thickness on the isotherm. If a film begins with large thickness h, and as shown in Figure 2.4 P_c is less than the initial peak Π_{max}, then the film will reach a metastable state there. This type of film is called a common black film, and its thickness depends strongly upon applied pressure, as can be seen from the small gradient of $d\Pi(h)/dh$ above 100 Å. Here the stability is due to the strength of electrostatic double layer forces preventing further thinning.

If the applied pressure momentarily or permanently rises above Π_{max}, the film will enter the thinner region where films of around $\sim$ 30 Å to 70 Å are observed, called Newton black films. In this region, the head groups of surfactant molecules are in close proximity to one another, meaning the steric forces are responsible for stability. The thickness depends upon applied pressure, surfactant type, salt concentration and other factors.

2.2.3 Experimental Studies

The primary method of observing thin film thickness under applied pressure, statically or over time, is with a Thin Film Balance (TFB) apparatus, originally designed by Mysels and Jones [77]. A typical set-up is shown in Figure 2.6a. The film is formed in the fritted glass disk, connected to a vertical reservoir capillary tube. This assembly is placed in a sealed pressure vessel with the other end of the capillary tube open to the air. The pressure inside the pressure vessel is controlled using a syringe pump, and measured using a transducer.

The disjoining pressure can be measured with this apparatus, as shown by Bergeron and Radke [11], through measuring the physical quantities in Equation 2.7:

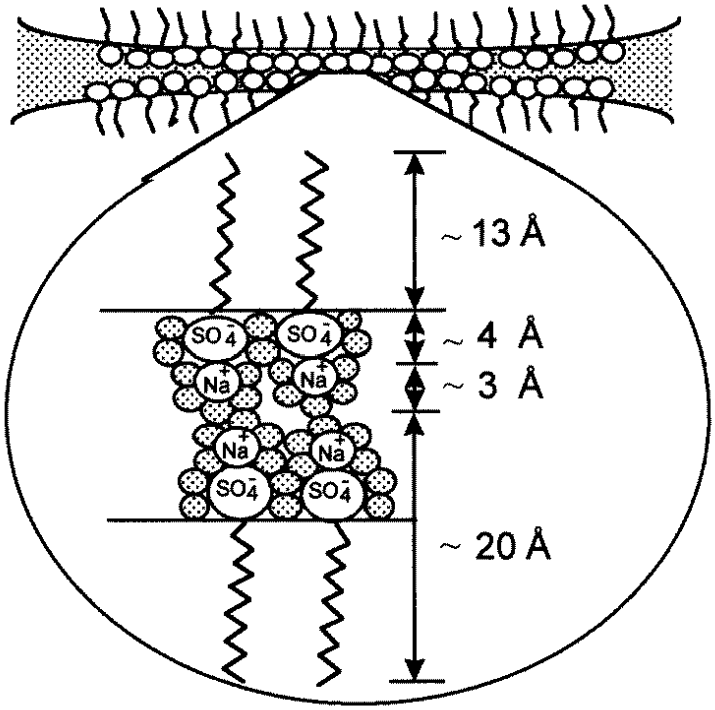

Figure 2.5: Schematic of the profile of a Newton black film stabilised by sodium dodecyl sulphate (SDS), from [12]. Filled circles correspond to water in the first hydration shell, surfactant head groups are labelled and the hydrocarbon chain is depicted by the irregular lines.

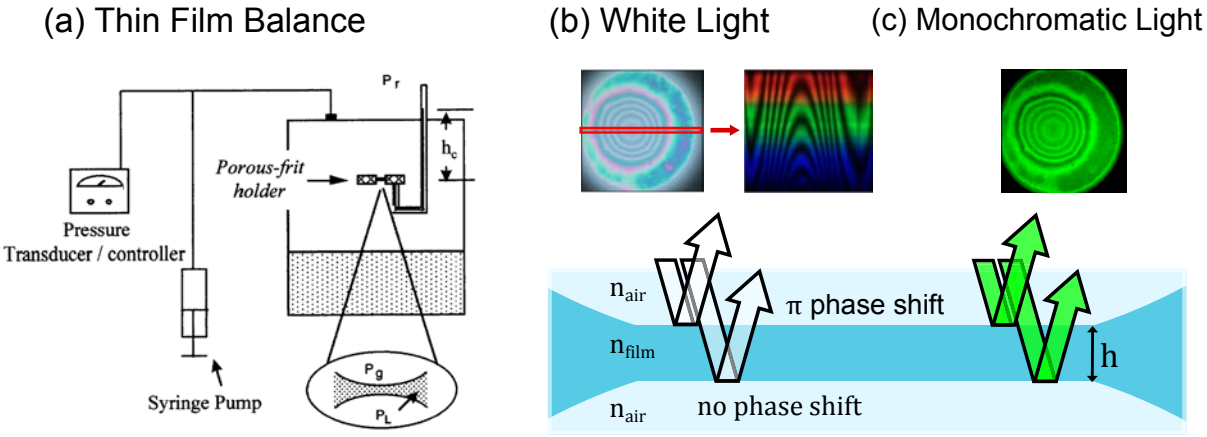

Figure 2.6: (a) Schematic of a thin film balance apparatus from [12]. (b) and (c): Measurement of the film thickness h through interferometry. A microscope objective in reflection mode is focused upon the film. The light is usually perpendicular to the film, shown here at an angle for visual clarity. Light incident upon the film reflects from the top and bottom, and the interference depends upon the optical path length difference between the paths. If the refractive index n_{film} is known, the thickness can be calculated. (b) White light results in Newton colours in a film image, and a spectrometer can give the wavelength-dependent intensity. (c) Monochromatic incident light can be used with a photomultiplier or other precise instrument to measure the intensity across the film.

$$\Pi = P_g - P_r + \frac{2\gamma}{r_{\text{cap}}} - \Delta\rho g h_c \tag{2.7}$$

where P_g and P_r are the pressures inside the vessel and the reference (atmospheric) pressure, as shown in Figure 2.6a. The third term is the Laplace pressure contribution due to the curvature in the capillary tube, r is the radius of the capillary tube. $\Delta\rho$ is the density difference between the solution and the gas, and h_{cap} is the height of the liquid in the capillary tube above the height of the film.

The thickness of the film can be measured using interfereometric techniques, as illustrated in Figure 2.6b and c. A microscope objective is focused upon the film in reflection illumination mode, and either a white light source (b), or a monochromatic source such as a laser or filtered lamp (c) can be used. The light reflects from the top and bottom of the film, and is collected by the objective. Typically the objective focus plane is parallel to the film. As such, the optical path length difference between the light from the top and bottom of the film is OPL $= 2n_{\text{film}}h$. Typically $n_{\text{air}} < n_{\text{film}}$, so the top reflection undergoes a phase shift of π while the bottom reflection does not. From the resulting interference pattern, the thickness h can be extracted.

If white light is used as in Figure 2.6b, a spectrometer will give the wavelength-dependent intensity of the signal for a line across the film, assuming uniform refractive index throughout the film. The wavelengths of the maxima and minima in brightness are calculated using equation 2.8, with $m = 1, 2, 3, ...$ representing the 'order' number (ie. the number of complete wavelengths that fit within the optical path length):

$$\begin{aligned} \text{OPL} \;=\; 2n_{\text{film}}h \;&=\; (m + \frac{1}{2})\lambda_{m,\,\max} \\ &= m\lambda_{m,\,\min} \end{aligned} \tag{2.8}$$

If instead monochromatic light is used as in Figure 2.6c, the precise intensity must be measured, and a standard Scheludko interferometric equation yields the thickness (again assuming uniform refractive index):

$$h = \left(\frac{\lambda}{2\pi n_{\text{film}}}\right) \arcsin\sqrt{\frac{\Delta}{1 + 4R(1-\Delta)/(1-R)^2}} \tag{2.9}$$

where $\Delta = (I - I_{\min})/(I_{\max} - I_{\min})$, I being the measured value of the reflected intensity, and $I_{\min}$ and $I_{\max}$ are the minimum and maximum intensity of the previous trough and peak in intensity respectively, which are observed as the film thins to the current point. $R = (n_{\text{film}} - n_{\text{air}})^2/(n_{\text{film}} + n_{\text{air}})^2$.

Using these methods and equations for the film thickness, and the above method for measuring the disjoining pressure, the disjoining pressure isotherm can be plotted. Additionally the dynamics of film drainage can be studied for a given applied pressure. This will be discussed in more detail in the following section.

2.3 Thin film drainage

Drainage dynamics, i.e. the rate by which the thickness h of a film changes over time, is a key property of systems involving thin films such as foams and emulsions, especially during foaming or emulsification. The microscopic study of drainage dynamics for a single model thin film can indicate the stability of a macroscopic system. It can be used to examine the origins of its behaviour, along with ways to control it, more easily and with greater precision than in-situ experiments.

2.3.1 Reynolds Law

The drainage of a thin film upon the application of pressure is essentially a hydrodynamic problem, especially early in drainage when the interfaces are sufficiently far apart for the contribution of the disjoining pressure to be minimal.

The simplest model for the drainage of a thin film is the Reynolds law for the symmetrical and homogeneous drainage of a liquid squeezed between two parallel disks [93]. This is given by:

$$V_{\mathrm{Re}} = \frac{2h^3 \Delta P}{3\mu R^2} \tag{2.10}$$

where μ is the viscosity, ΔP the pressure difference between the capillary and disjoining pressure driving drainage, and R the film radius. However, this requires tangentially immobile, plane-parallel film surfaces and an equilibrated Plateau border.

2.3.2 Dimples

Real films, especially large films, have a tendency to form dimples. This is due to the imbalance in pressure between the centre of a film and its plateau border, and the hydrodynamics of drainage. Figure 2.7a shows a schematic of a dimpled film, where the dimple in the centre is surrounded by a thinner barrier ring. This thinner region slows drainage of the dimple, and the Reynolds law drainage velocity V_{Re} is then an upper bound on the velocity of drainage.

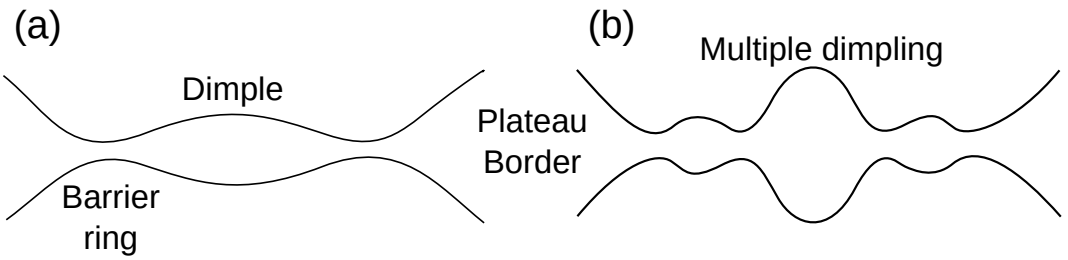

Figure 2.7: Schematic of a single (a) and multi (b) dimpled thin film.

Whether a film will form a dimple or not depends upon many factors, but becomes more likely the thinner a film is. Tsekov et al. derived an expression for a transition thickness whereupon a dimple will begin to form in a symmetrical film:

$$h_{\mathrm{d}} = \sqrt{\frac{3\mu Q}{4\pi\gamma \cos^2\theta}} \tag{2.11}$$

where Q is the fluid flow rate, μ the liquid viscosity and θ is the contact angle made between the Plateau border and the film holder. Note that increased flow rate increases the minimum thickness for a dimple, as does a contact angle approaching $\theta = 90°$.

Tsekov extended the Reynolds law from assuming plane-parallel films to allow any local film thickness [105]. By setting the condition that the film thickness always had to be positive, Tsekov put the following limit on the use of the Reynolds law:

$$R \leq \sqrt{12\gamma h/\Delta P} \tag{2.12}$$

where h is now the average film thickness. This implies that only small films that are relatively homogenous in thickness can be explained with the Reynolds equation, and larger films are much more complex. This is consistent with experimental work, for instance Radoev et. al [89] reported that films with $h = 250\,\text{nm}$, $\Delta P = 35\,\text{Pa}$, $\gamma = 35\,\text{mN/m}$ and $\mu = 1\,\text{mN}\,\text{s}\,\text{m}^{-2}$ only obey Equation 2.10 if their radius is smaller than 50 µm, which is the value predicted by the inequality above.

Above this cutoff radius, the film behavour increases in inhomogeneity with increasing film radius [89]. Indeed, dimples in thin films become unstable, often breaking up into multiple smaller structures [70]. This drains more quickly due to more favourable hydrodynamics [105]. Tsekov proposes an alternative model for dimpled thin films:

$$V = \frac{1}{6\mu}\sqrt[5]{\frac{h^{12}\Delta p^8}{4\gamma^3 R^4}} \tag{2.13}$$

The $V \propto R^{4/5}$ scaling is in excellent agreement with experimental results [104]. However, this formula only works for symmetrical films, which again are most common for low film radii.

2.3.3 Asymmetric Drainage

The above models all assume symmetry about the film's centre point. If this is not the case, as in large films, films with aggregation of stabilisers at the surface, or otherwise, the system becomes hugely more complex. Joye et al. [61] performed numerical simulations of the instabilities in foam films that lead to asymmetric drainage. Their results confirmed that asymmetric drainage leads to a rapidly increased drainage rate. They conclude that "asymmetric drainage is the result of an instability involving surface-tension-driven flow that is stabilised by surface dilational viscosity, surface diffusivity, system length scale, and, especially, surface shear viscosity".

Chapter 3

Hard and Soft Particles at Liquid Interfaces

Contents

3.1 Hard particles at interfaces

Using hard colloidal particles to stabilise interfaces in place of traditional surfactants was first scientifically documented by Pickering [86] and Ramsden [91]. Since then, a multitude of applications of this phenomena along with other uses of particles at interface have emerged. Food science, flotation technology and emulsion polymerization all make use of the so-called Pickering mechanism of solid-stabilised emulsions. The fluid-fluid interface can also be used to assemble 2-D crystals, which than can be coated onto substrates (Langmuir-Blodgett technique [92]). This chapter will first examine the behaviours of hard particles at interfaces, individually in terms of single-particle adsorption and desorption, and in Pickering emulsions.

3.1.1 Desorption Energy

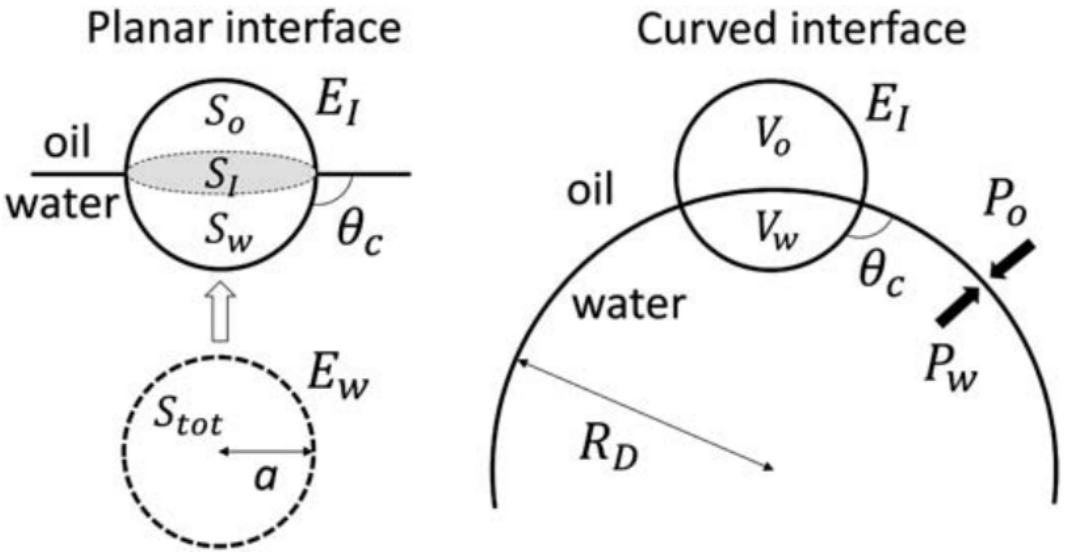

Figure 3.1: Spherical colloidal particle adsorbed to a fluid/fluid interface, from [83]. Contact angle of the three-phase contact line determines resting height of the particle through the interface, which in turn determines the area of interface that the particle displaces.

In free energy terms, fluid interfaces are costly. If one desires to create new interface, eg. for creating an emulsion, an oil-water interface will require energy input of $\sim 40\,\mathrm{mJ\,m^{-2}}$, which is very large compared to the thermal energy $k_\mathrm{B}T$ at room temperature. But that same high energy contributes to keeping particles covering the interface. When a hard particle adsorbs to a liquid interface from the aqueous phase, as shown in Figure 3.1, an area of the liquid-liquid interface is now covered by the particle. For colloidal particles, typically their mass is sufficiently low that the interface is not bent due to gravity, but remains flat. Mathematically, a flat interface can be assumed if the Bond number, ($\mathrm{Bo} = \Delta\rho\, g R^2/\gamma$ where $\Delta\rho$ is the difference in density between the particle and the liquid, g the gravitational acceleration, R the radius of the particle and γ the fluid-fluid surface tension), which represents the ratio of the gravitational force to the surface tension, is low ($\mathrm{Bo} \ll 1$). The size of the displaced area is determined by the particle shape, size and contact angle with the two fluids. In order to remove the particle, that interface must again be created, which has a free energy cost. For a spherical particle at a planar interface, the cost in free energy terms of removal into the aqueous phase ΔG_w, or the oil phase ΔG_o are given by Equation 3.1 and Equation 3.2 respectively:

$$\Delta G_w = \pi R^2 \gamma (1 - |\cos\theta|)^2 \tag{3.1}$$

$$\Delta G_o = \pi R^2 \gamma (1 + |\cos\theta|)^2 \tag{3.2}$$

where R is the particle radius, γ the surface tension between the liquid phases and θ the equilibrium contact angle the particle makes with the phases. This energy is plotted in Figure 3.2.

To contextualise this with some typical values for the oil/water interface, a hydrophobic 1 µm diameter particle making a contact angle of 110° with the oil/water interface (surface tension $\gamma \approx 40\,\mathrm{mN/m}$, and θ defined as in Figure 3.1) results in a desorption energy of 1.36×10^{-14} J, or $10^6 k_\mathrm{B}T$ at room temperature, to remove the particle into the oil phase. Since this energy scales with the

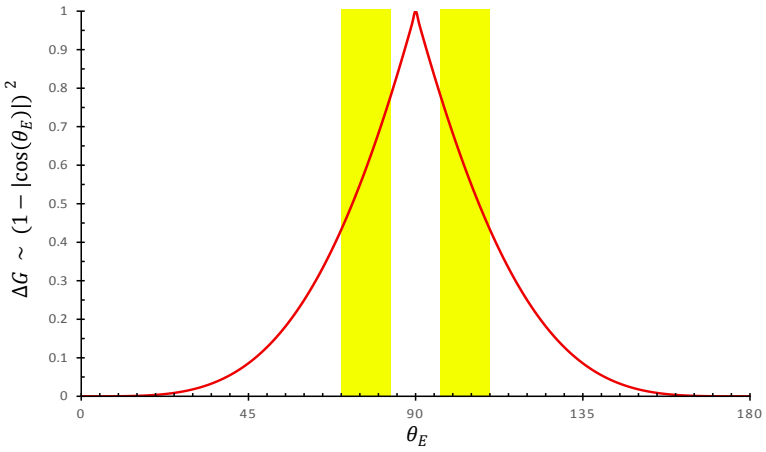

Figure 3.2: The cost in free energy to desorb a particle for a given equilibrium contact angle θ_{E}. The most common range for Pickering stabilisation is approximately shown in yellow.

particle radius squared, even for low-tension interfaces, micrometer-scale colloidal particles can still reach energy values of tens to thousands of $k_{\mathrm{B}}T$. For instance, if the surface tension were instead 40 µN/m as in polymeric aqueous phase-separating systems, and the contact angle 30°, the desorption energy would still be $10^2 k_{\mathrm{B}}T$. As such, the adsorption of colloidal particles that are sufficiently large to fluid/fluid interfaces can be seen as effectively irreversible.

3.1.2 Features of solid-stabilised emulsions

There are many possible stabilisers for emulsions, including surfactants, amphiphilic polymers, and solid particles (Figure 3.3). However, Pickering emulsions can offer a degree of mechanical stabilisation that the others do not. Also, due to the wide variety of possible solid particles, from soft microgels (as in part of the present work) to nano-fabricated solid colloids of a specified shape, or even Janus particles that have multiple areas with different surface properties, Pickering stabilisers may be the most diverse. This section will provide an outline of the properties of such emulsions.

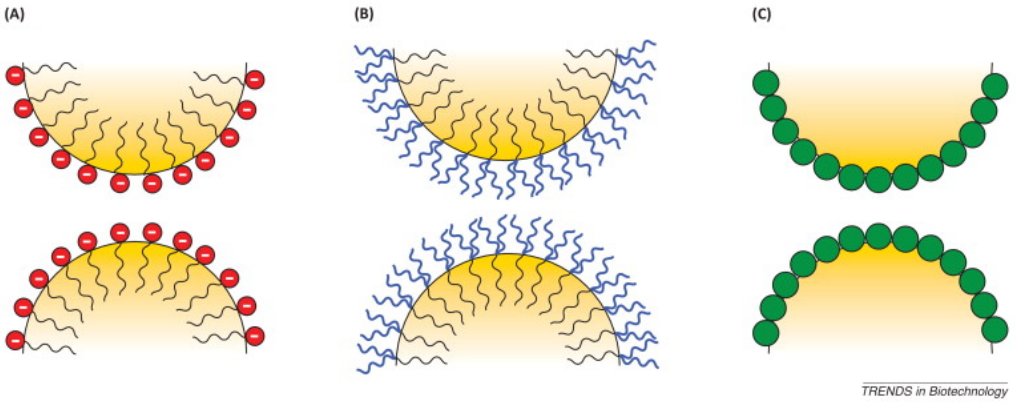

Figure 3.3: Examples of droplet stabilisation, from [51]. **A)** Charged surfactants offer stabilisation through electrostatic repulsion of other droplets. **B)** Large, neutral surfactants offer steric protection. **C)** Colloidal particles provide mechanical stabilisation.

3.1.2.1 Finkle Behaviour

The contact angle the particles make with the interface, and therefore the phase in which most of the volume of the particle sits, determines the preferred curvature of the interface, as curvature limits the available volume on the inside. This in turn generally determines which phase is the dispersed phase, and which the continuous, as droplets will ideally match the preferred curvature of the interface. This is known as 'Finkle' behaviour [35]. To optimise the wetting of the particle for stability, 90° is therefore not the best contact angle despite having the strongest attachment to the interface, as it will prefer a flat interface. Figure 3.2, the dependence of the free energy upon equilibrium contact angle, also shows the commonly-chosen range for emulsions marked in yellow.

3.1.2.2 Limited Coalescence

With high shear of emulsification and irreversible adsorption, once shear has ceased there will often be a large excess of interface not covered by particles, despite all particles being at interface. The small partially-covered droplets will coalesce, reducing the total surface area of interface, until the particles cover the larger droplet. This process is known as limited coalescence, and tends to produce highly monodisperse emulsions with a tunable and deterministic average droplet diameter $\bar{D}$, which will be inversely proportional to the concentration of stabiliser used m_p (Figure 3.4) [4, 103]:

$$\frac{1}{\bar{D}} = \frac{s_f}{\tau}\frac{m_p}{6V_d} \tag{3.3}$$

s_f/τ is the final droplet surface area divided by the surface coverage τ, and is dependent solely upon the mixing intensity, and insensitive to the method of mixing or volume fractions [4]. V_d is the total volume of the droplets. This dependence of the inverse droplet diameter on concentration is a sign in more complex systems that the Pickering mechanism is playing a role.

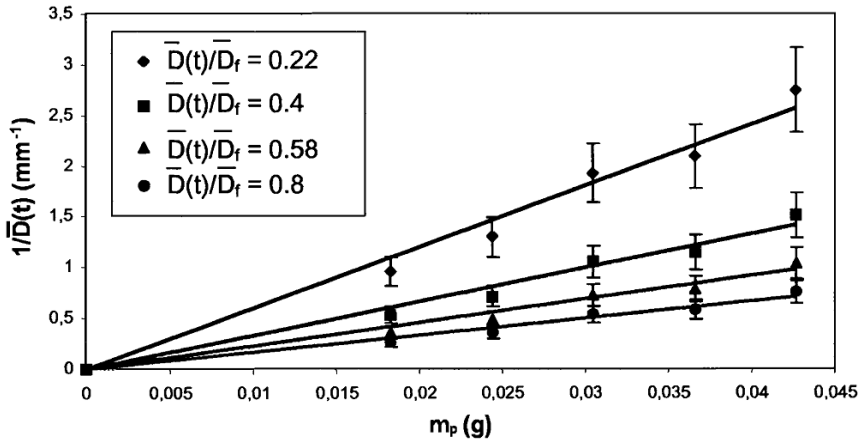

Figure 3.4: For Pickering emulsions where all particles may be at interface, the average droplet diameter $\bar{D}$ is inversely proportional to the concentration of stabiliser m_p, shown here for oil/water emulsions stabilised by solid mineral particles, from [4]. Slope of the graph gives surface coverage τ, which is determined by mixing intensity.

3.1.2.3 Interface protection

Protection of the interface, in terms of thin films between droplets resisting drainage or the interface resisting rupture when droplets come into contact, can delay or prevent coalescence. Pickering stabilisers are often somewhat effective at providing this form of protection. However, that can also be provided by (and may even be stronger for) charged surfactants [103].

Interfacial Rheology
The interface can be given increased viscosity or elasticity through the addition of interacting particles, which can provide protection against rearrangement of adsorbed particles under mechanical stress or shear, or increase the solid-like behaviour of the interface [75, 106].

Ostwald Ripening
Where Pickering emulsions have a true advantage over surfactant-stabilised emulsions is in protection against Ostwald Ripening. Ostwald ripening is the process of diffusion of the dispersed phase through the continuous phase, from smaller droplets to larger droplets. This is driven by the Laplace pressure difference between the two droplets, with the pressure inside the droplet due to the surface tension γ: $P = 2\gamma/R$ increases with decreasing droplet size, causing diffusion of the dispersed phase along the pressure gradient. When the interface of a droplet is covered with irreversibly adsorbed particles, interacting with each other sterically, through electrostatics or otherwise, a well-covered interface will begin to behave like a 2-dimensional solid, resisting any change in size [7]. Additionally, the thickness of the interfacial layer and reduction in area of liquid interface can reduce the ability of the enclosed phase to diffuse out.

3.1.2.4 Stability of emulsions under mechanical disturbance

Pickering emulsions are very stable at rest, from months to years. However, under mechanical stress (eg. handling), the particle layers at the interface can be disturbed or disrupted, or the thin films between droplets can rupture. Additionally, in emulsions stabilised with spherical colloidal particles, high shear can create new interface in the system, leading to imperfect coverage. Once two imperfectly-covered droplets come into contact, bridges can form where particles are shared between both interfaces [39]. Much lower shear is then all that is needed to rupture the thin film and cause the droplets to coalesce.

Further illustrating the issue of shearing Pickering emulsions, simulations using the Lattice Boltzmann method by Frijters et al [40] showed that under high shear, the reduction in surface energy due to the presence of particles can cause droplets to break that under the same shear without particles would not, as illustrated in Figure 3.5.

The authors expect this to breakup to lead to shear-thinning behaviour in Pickering emulsions. The simulations also showed that particles tended to bunch in dense patches at areas of high curvature, which may be an issue for particles that aggregate at interface or have low mobility.

3.1.3 Adsorption dynamics of particles at interfaces

To create a particle-stabilised interface for emulsification, or a particle-laden interface for self assembly, coatings, 2-D colloidal crystals etc., the particles must be brought to the interface and allowed

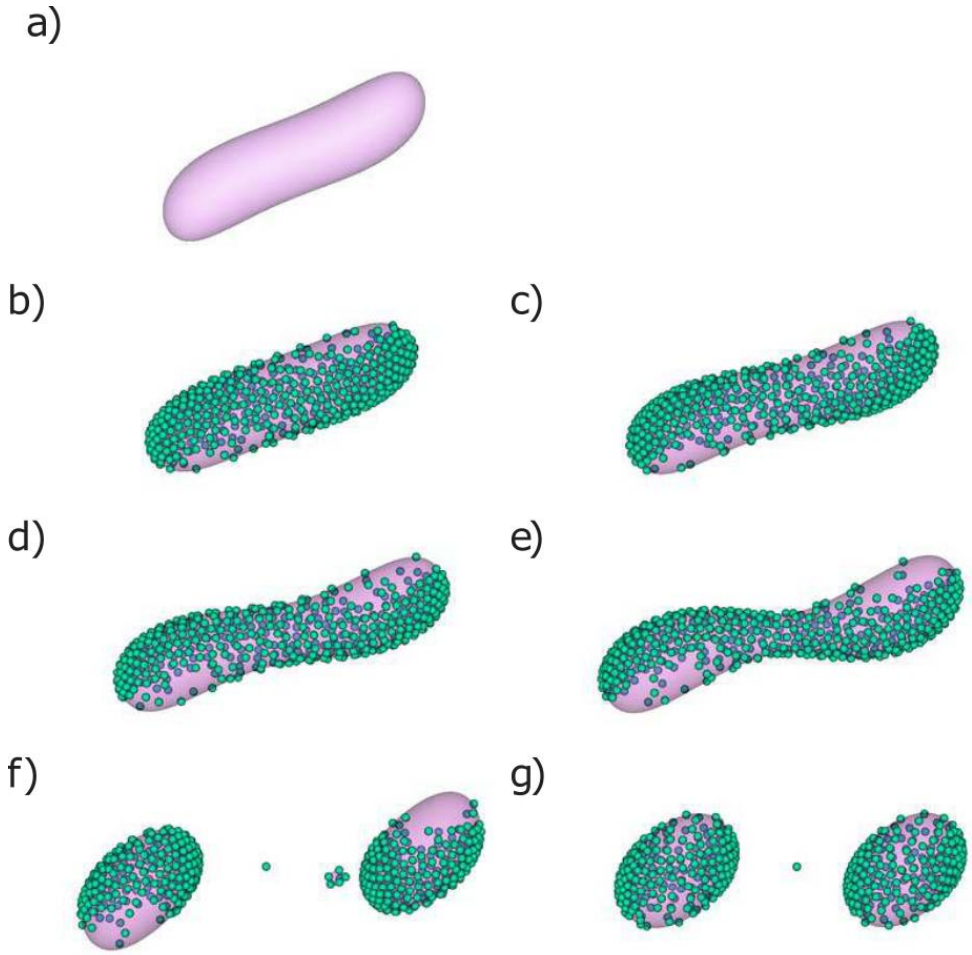

Figure 3.5: Lattice Boltzmann simulation results of a droplet under shear flow with ((b) - (g)) and without (a) neutral-wetting particles, from [40]. Without particles, droplet (a) has reached a steady state shape by timestep 100 000. Images (b) to (g) represent the deformation and splitting of the droplet at timesteps 50 000, 70 000, 80 000, 90 000, 100 000 and 150 000 respectively.

to adsorb. To be able to predict and control the behaviour of particles at interface, the precise dynamics are very important.

For example, when emulsifying, the rate of particle adsorption must be sufficiently fast for the particles to adsorb during the shearing process, or else particles may be left in bulk. When creating 2-D crystals of self-assembled structures, the interactions between particles (especially capillary, electrostatic or Van-der-Waals interactions) can be highly dependent upon the contact angle of the particles. However, the relaxation to equilibrium contact angle as a particle adsorbs is a dynamic process, and if the timescale is slower than that of the accumulation of particles at interface, unexpected results may occur. Finally, for complex systems, for example demixed aqueous polymer-polymer systems (discussed in greater detail in Chapter 4), measuring the adsorption dynamics can give insight into the forces experienced by particles in the vicinity of the interface between the polymer phases.

The dynamics of adsorption of a particle to a fluid-fluid interface is a deceptively complex problem, involving not only bulk and chemical properties such as viscosity, surface tension and equilibrium contact angle, but molecular-scale dynamics of fluctuating interfaces interacting with nanoscale surface defects of particles.

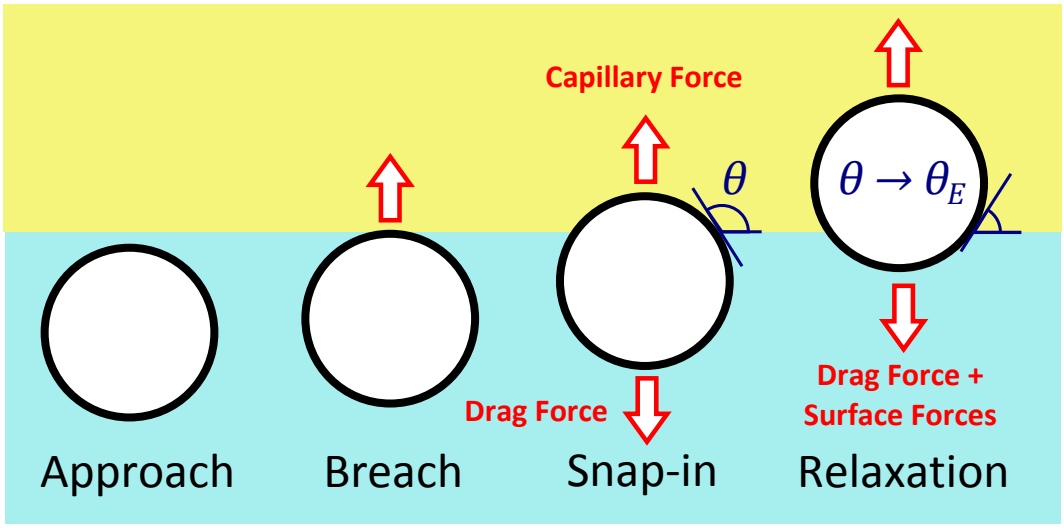

Figure 3.6: The adsorption of a spherical particle to a fluid/fluid interface. The process is split into four steps: **approach** is the approach of the particle to the interface and the draining of the thin liquid film of initial phase that separates the particle from the interface. **Breach**: A hole forms in the interface and wetting of the particle surface begins. **Snap-in**: Large capillary forces on the particle cause high velocity for part of the adsorption before the particle begins to approach its equilibrium contact angle and the forces lessen. **Relaxation**: The relaxation of the contact line to its equilibrium position can be very slow, as thermal motion of the contact line causes it to pass through various meta-stable states caused by pinning.

3.1.3.1 Experimental Work

Figure 3.6 demonstrates a typical adsorption process. The adsorption is split into four stages; approach, breach, snap-in and relaxation. The approach phase is typically dominated by hydrodynamic effects. If there is electrostatic or other repulsion between the particle and the interface, the

particle may reach an equilibrium separation from the interface.

Kaz et. al showed relaxation to the equilibrium contact angle θ_E can be an extremely slow process, often much slower than experimental timescales [62]. Using digital holographic microscopy, they studied the adsorption of micrometer-scale spherical colloidal particles to the water/decane interface, under the action of a low-power optical tweezer. The technique allowed 2 nm and sub-microsecond resolution. It showed that relaxation to θ_E, far from being a fast (micro- to millisecond timescale) process as predicted by a force balance of capillarity versus viscosity, instead was logarithmic in time. Reaching a contact angle close to equilibrium could take days to months.

The authors proposed that the logarithmic decay could be due to the pinning of the three-phase contact line on nanoscale physical or chemical surface defects of area A_d that the contact line requires a thermal 'kick' to overcome. This stochastic process would drastically slow dynamics.

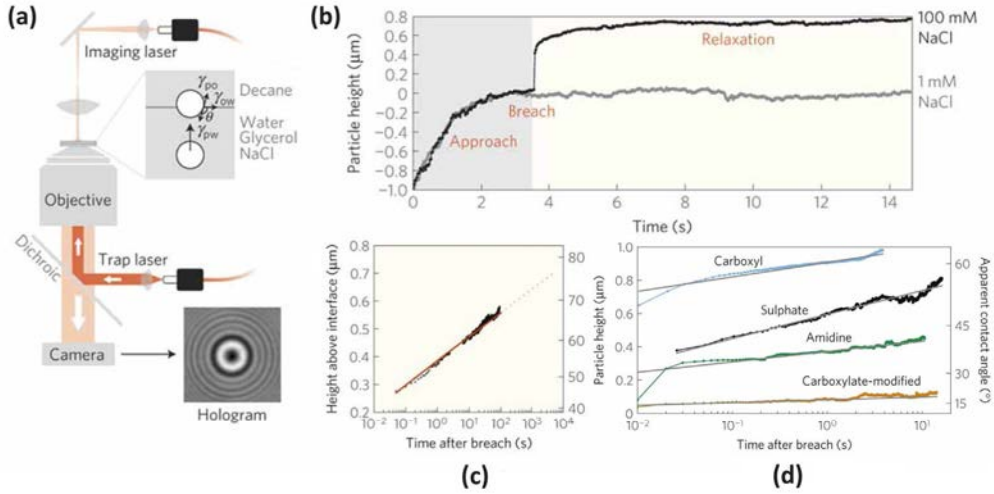

Figure 3.7: Summary of [62]. (a) Experimental setup for digital holographic microscopy including an optical trapping laser. (b) A complete particle trajectory, with and without salt. (c) Semilogarithmic plot of particle displacement over time in the relaxation to equilibrium, showing that dynamics are very slow. (d) Logarithmic relaxations are observed for all particle surface chemistries, though with different gradients.

In their follow-up study [116], the group studied the adsorption of hydrophobic PDMS-stabilised and PHSA-stabilised PMMA microspheres from the decane phase to the water phase, and observed very fast dynamics, and that the slow relaxation did not occur. The authors ascribed this to the difference in surface functionality between the sterically-stabilised PMMA particles and the charge-stabilised Latex particles.

Additionally, they investigated whether the origin of the contact line pinning they observed in [62] was due to physical or chemical heterogeneities by observing the adsorption of carboxyl-functionalised particles under varying acid concentrations. By adding HCl, the surface charge densities were increasingly reduced, with a correspondingly large reduction in Zeta potential. If charges are responsible for pinning, the authors would expect likewise a reduction in the fitted area per pinning group, A_d. The resulting trajectories are shown in Figure 3.8. Although a clear difference in particle height at interface is visible, the area per group A_d affects only the slope, which is very similar between all acid concentrations. The authors therefore conclude that the contact line pinning is due to physical defects.

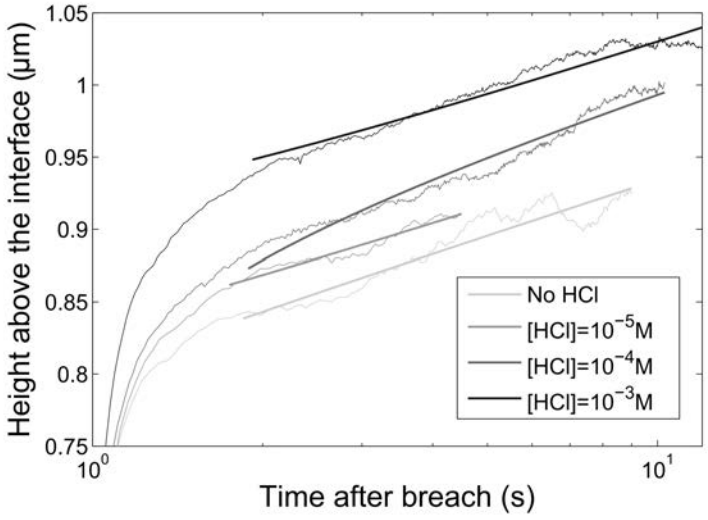

Figure 3.8: Post-breach trajectories of carboxyl-functionalised latex particles in solutions of varying acid concentration, from [116]. Thin lines are averaged trajectories for several particles at each acid concentration. Thicker lines are fits to a logarithmic relaxation model.

Chen et al. investigated the dynamics as well as the forces involved in the snap-in stage using a colloidal probe AFM, observing the adsorption of a spherical silica particle attached to an AFM cantilever to the air-water interface. The particles used were large (diameter 44 µm to 172 µm). An example is shown in Figure 3.9a. While the Silica surface was initially hydrophillic, it could be chemically treated to turn it hydrophobic. The particle was brought into contact with the air-water interface of a water droplet trapped inside a capillary, as shown in Figure 3.9b.

The technique could not extract whole trajectories in the same way as optical observation of particle adsorptions due to the elastic restoring force of the cantilever acting against the capillary force. But, the initial sub-millisecond snap in dynamics were captured with remarkable time resolution.

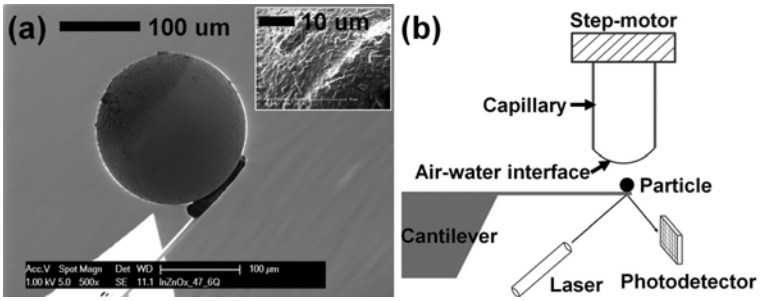

Figure 3.9: From [17]. **a)** SEM images of a silica glass bead with diameter 172 µm glued onto a cantilever. Inset is a zoom of the surface. **b** Schematic of the AFM particle interaction apparatus. The stepper motor brings the particle into contact with the water droplet, and the deflection of the laser point caused by the bending of the cantilever is measured by the photodetector.

The trajectory is shown in Figure 3.10 at three successive zoom levels in time, first for the initial 6 s after breach, then the initial 100 ms, then the initial 3 ms. The motion is characterised by a ~ 0.1 ms snap-in to a balanced position D_B, shown in Figure 3.10d. Analysis of the results showed inertia is important in the snap-in time t_s, as this scaled as $t_s \sim (\rho_P R^3/\gamma)^{1/2}$, where ρ_P is the

density of the particle. However the 44 µm to 172 µm Silica particles have a mass $\sim 10^6$ times larger than particles used in other studies, so this may not always be the most important contribution.

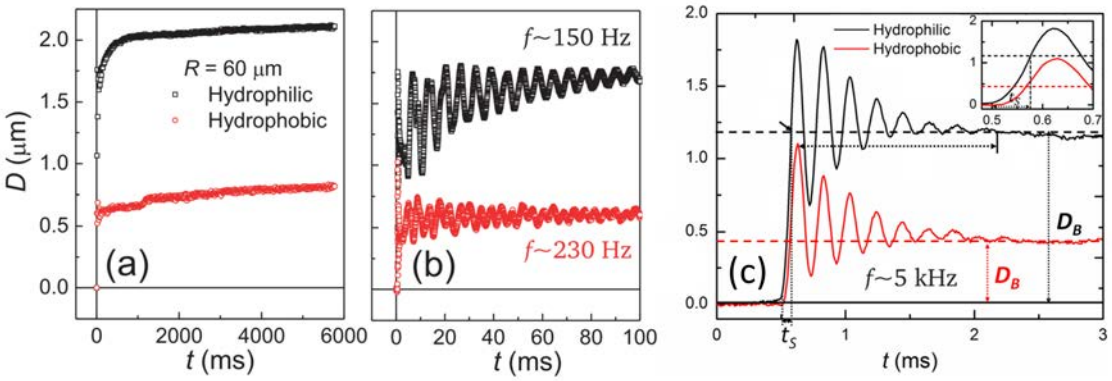

Figure 3.10: Snap-in of a 120 µm diameter particle. Oscillations in (b) caused by activation of capillary waves, whereas those in (c) are due to resonance of the cantilever. Inset shows initial ~ 0.2 ms of the motion, defining the 'snap-in time' t_s. D_B is the cantilever deflection at which the capillary force balances the cantilever spring force.

So far, no study has examined the adsorption dynamics of particles to the interface in an aqueous two-phase system (ATPS), such as a demixing polymer solution. Sinha et al. investigated the dynamics of magnetic particles crossing the water/water interface under a large magnetic force, focusing on the velocity in the bulk phase.

3.1.3.2 Theoretical Models

Once the particle has breached the interface, clearly both hydrodynamics and wetting play a role in determining the dynamics. This section introduces some of the models advanced in literature.

Capillarity vs. Drag

The simplest possible model would be the balance of capillary forces with Stokes drag. In this model, the driving force of motion is the imbalance in surface tensions when the contact line of a particle does not make its equilibrium angle with the surface. For a spherical particle adsorbing to a flat interface, this force F_s equates to a simple Hookean spring once all geometry is accounted for:

$$F_s = k(z - z_E) \tag{3.4}$$

where k is a spring constant given by $k = 2\pi\gamma$, z is the height of the particle and z_E is the height of the particle at its equilibrium contact angle. The viscous drag, neglecting for now the influence of the interface, is given by Stokes's law:

$$F_d = \xi\dot{z} = 6\pi\mu R\dot{z} \tag{3.5}$$

where ξ is a drag term, which is given for Stokes drag above. μ is the viscosity of the fluid, and $\dot{z}$ the differential of z with respect to time. The solution to this equation, neglecting minuscule inertial contributions, is an exponential function:

$$z = z_E - z_0 \exp(-t/T_D) \tag{3.6}$$

where the decay time $T_D = 3\mu R/\gamma$, and z_0 is the distance from equilibrium at the start of the motion. Comparing this model to the data, this overestimates the speed of decay by typically an order of magnitude, and, unsurprisingly, does not recover the logarithmic behaviour observed in experiments. However, the snap-in dynamics do often exhibit exponential behaviour, indicating alternative models to Stokes drag might capture the snap-in motion more accurately. Alternatives and supplements to this model proposed in literature are covered below.

Hydrodynamic Models

Hydrodynamic models are meso-scale models that ignore the molecular details of a system, and attempt to explain dynamic wetting of solids on purely hydrodynamic grounds, examining the complex hydrodynamic systems that arise when interfaces present boundaries impervious to flow.

Important at this length scale is the fact that viscous dissipation diverges at the contact line, which changes the microscopic contact angle θ_m in relation to the macroscopic dynamic contact angle θ_D according to the Cox-Voinov law [22]:

$$\theta_D^3 - \theta_m^3 = 9\mathrm{Ca} \ln \frac{L}{L_m} \tag{3.7}$$

where Ca is the Capillary number, L a macroscopic length (eg. the capillary length) and L_m a microscopic length scale, eg. the slip length at the solid/liquid interface.

One such hydrodynamic model applied to particles at interfaces is introduced by Kaz et al. in the supplementary information of their paper examining adsorption dynamics experimentally. They examine whether a hydrodynamic model detailing the enhanced viscous drag on the sphere caused by a trapped wedge of fluid between the particle and the interface explains their slow relaxation dynamics. Although this model would result in slower dynamics, the model completely fails to recover the observed dynamics in 3 key ways. Firstly, the model predicts a more gradual initial accelleration, which is not observed. Secondly, at later times the predicted velocity is seven orders of magnitude too large. And finally, the logarithmic behaviour of the relaxation is not recovered.

Contact Line Hopping Models

To explain the logarithmic dynamics they observed during the relaxation of the particle to its equilibrium contact angle, Kaz et al. successfully used a model examining the molecular-scale motion of the contact line. They proposed an Arrhenius model in which an advancing contact line underwent a series of stochastic, thermally-activated 'jumps' to approach equilibrium. These jumps, the authors argued, represented the pinning of the contact line by nanoscale abnormalities on the surface of the particles. The defects of area A_d, either chemical or physical (though later proven to be physical [117]), trap the contact line in a potential well of depth U, with its energy modified by the capillary force driving the motion. The velocity of the contact line (and hence the particle) is determined by the rate of these jumps, and the pinning causes dissipation of energy slowing the adsorption.

Due to the assumed strength of the driving capillary force, backward hops of the interface are assumed to be of negligible probability far from equilibrium and are not accounted for in the model.

The velocity $\dot{z}$ is given in their model as:

$$\dot{z} = \nu\sqrt{z(2R-z)}\,\exp -\frac{A_d\gamma_{\mathrm{ow}}z}{2Rk_{\mathrm{B}}T} \tag{3.8}$$

where ν is a fitted constant, where $1/\nu$ represents the time for the contact line to overcome a defect. It is given by:

$$\nu = (V_0/R)\exp -U/kT + (1-\cos\theta_E)\,A_d\gamma_{\mathrm{ow}}/2k_{\mathrm{B}}T$$

where V_0 is an unspecified molecular velocity scale. The only fitting parameters are ν and the defect area A_d, and the model recovers the logarithmic trajectory very well, as illustrated for particles of different surface chemistry in Figure 3.7d. Therefore, the authors conclude that the long-time dynamics of the relaxation to equilibrium of colloidal particles wetting a fluid interface are caused by surface effects on the molecular scale. Further, they measure the size of a defect on the surface to be of order $1-10\,\mathrm{nm}^2$, and independent of the particle size.

Expanding on this model, Colosqui et al. [21] revisited the data presented by Kaz et al. with a more complex theoretical model and with molecular dynamics simulations. In their theoretical model, the motion is driven by minimization of the surface free energy, given by $U(z)$. The equation of motion is:

$$m\ddot{z} = \sqrt{2k_{\mathrm{B}}T\xi}\,\eta(t) - \xi\dot{z} - \frac{\partial U(z)}{\partial z} \tag{3.9}$$

where the first term on the right hand side is the Brownian motion of the particle, with η representing a zero-sum white noise. ξ is the viscous drag coefficient, which includes the hydrodynamics of the system. $U(z)$ has two parts,

$$U(z) = U_s(z) + \frac{1}{2}\Delta U\sin(\lambda z+\phi) \tag{3.10}$$

the first simply given by the capillary force as described in the 'Simple Model' section above as a Hookean spring pulling the particle towards its equilibrium position z_E, illustrated in Figure 3.11b. The spring constant is again $K = 2\pi\gamma$. The potential is given by:

$$U_{\mathrm{s}}(z) = \frac{1}{2}K(z-z_{\mathrm{E}})^2 - \pi\gamma(R-z_{\mathrm{E}})^2 \tag{3.11}$$

Illustrated in Figure 3.11a is the second potential term, which models the roughness of the interface as a sinusoidal potential well of amplitude ΔU. The wavelength is $l = 2\pi/\lambda$.

These two potentials in turn lead to two stages of dynamics. Initially, 'snap-in' dynamics will follow an exponential behaviour with some time constant T_D, as in the exponential model described above. Then near some separation from the interface z_C, a crossover takes place to dynamics dominated by the thermal jumps over surface defects, with a logarithmic trajectory.

The authors' solution to the equation of motion in the logarithmic regime gives the average (as this is a stochastic process) particle trajectory post-crossover $\langle z\rangle$:

$$\langle z\rangle = z_E + L_H\log\frac{1+A_H\exp(-t/T_H)}{1-A_H\exp(-t/T_H)} \tag{3.12}$$

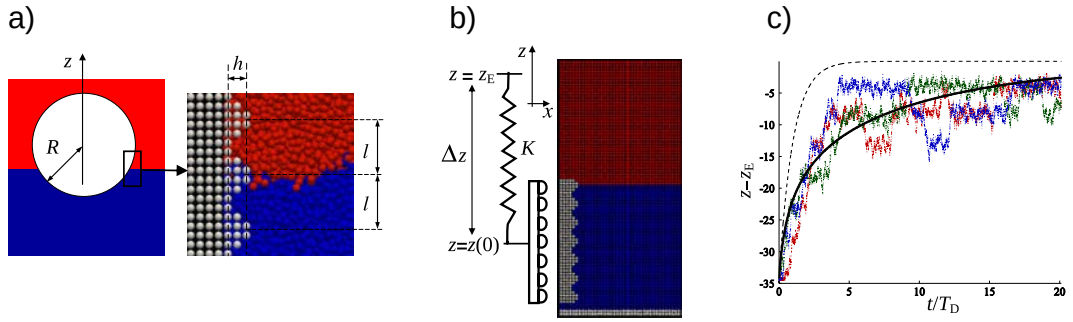

Figure 3.11: Introduction to the model of Colosqui et al. [21]. (a) The particle surface roughness is modelled as having a sinusoidal potential energy landscape. (b) The capillary force is represented as a spring with constant $K = 2\pi\gamma$. (c) Thin lines: molecular dynamics simulations of particle motion. Black line: fit to Equation 3.12.

This equation is governed by three parameters given by physical variables; the characteristic hop length L_H, given by:

$$L_H = \frac{2k_\mathrm{B}T}{Kl} \tag{3.13}$$

The trajectory 'amplitude' A_H:

$$A_H = \tanh \frac{1}{2}\Delta z / L_H \tag{3.14}$$

where Δz is the distance from equilibrium at the start of the motion, $\Delta z = z(t = 0) - z_E$. Finally, the characteristic hop time T_H:

$$T_H = T_D \left(\frac{L_H}{l}\right) \frac{2\pi}{\sqrt{|\Phi^2 - 1|}} \exp\left(\frac{\Delta U}{k_\mathrm{B}T} + \frac{1}{4}\frac{l}{L_H}\right) \tag{3.15}$$

where Φ represents the ratio between the free energy curvature of the modelled surface, and that of a perfectly smooth sphere, given by $\Phi = \frac{1}{2}\Delta U \lambda^2 / K$.

The fitting parameters for this model, assuming the initial distance from equilibrium is known, are the amplitude of the potential perturbation ΔU and the distance between peaks of the potential l, also known as the perturbation wavelength. To explain l physically, it represents the distance that the whole contact line moves before being pinned by a defect somewhere around the particle circumference.

In Ref [21], the authors explore the influence of ΔU and l upon the trajectory of adsorbing particles. Figure 3.12 demonstrates the two regimes, exponential and logarithmic, as well as Langevin Dynamics simulations confirming the resulting trajectories.

Two values of ΔU are shown, $10k_\mathrm{B}T$ and $20k_\mathrm{B}T$. For each there are two values of l, specified in terms of a characteristic length $\sqrt{k_\mathrm{B}T/\gamma}$: $l = 4\times$ and $16 \times \sqrt{k_\mathrm{B}T/\gamma}$, which for a typical oil/water interface at room temperature would equal 1.27 nm and 5.08 nm respectively. Without knowing the particle radius this cannot be converted into the defect area A_d. The y axis of the plots in Figure 3.12 is also rescaled by this characteristic length.

The authors note that increasing the perturbation wavelength l, or decreasing the energy barrier ΔU will delay or even prevent the onset of the thermally activated contact line hopping regime. On the other hand, very large ΔU or small l would lead to purely logarithmic behaviour. Graphically,

ΔU can be seen to influence the y-axis positioning of the logarithmic model, and l influences more the gradient of the line in the semilogarithmic plot.

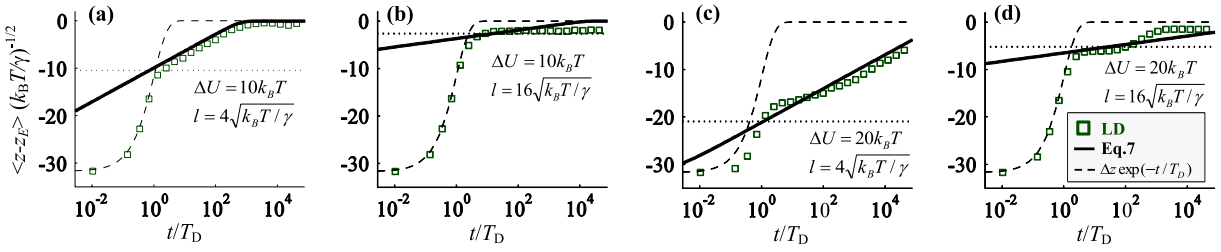

Figure 3.12: Regime crossover during adsorption, from an exponential behaviour with time constant T_D, shown as the dashed line, to a slower logarithmic decay (given by Equation 3.12, solid line) once the surface potential dominates, adapted from [21]. The crossover takes place at a separation z_C from the interface, shown as the dotted line. Points represent Langevin Dynamics (LD) simulations. (a) - (d) represent a range of sizes (in terms of their potential ΔU) and separations (l) of surface defect, given in the legends for each figure.

Applying this model to the results of Kaz et. al. for Sulphate particles, imposing an energy barrier $\Delta U = 15 - 30 k_{\mathrm{B}}T$, the model matched well to the experimental data for an $l \sim 0.5 - 1 \times 10^{-12}$m. Using $l = A_d/p$, where $p = 2\pi R$ is the particle perimeter, they find a defect area A_d of $\sim 3\,\mathrm{nm}^2$. The authors also checked the validity of the model under other physical parameters through molecular dynamics simulations.

This model differs from that proposed by Kaz et al. in a few ways. Both forward and backward hopping of the contact line are allowed as the system attempts to minimise its free energy, moving according to Kramer's Theory for thermally-driven movement between metastable states [64] as opposed to an Arrhenius equation.

However, like the model proposed by Kaz et al., the logarithmic trajectory describes only the relaxation stage of the motion, the snap-in stage being described by the exponential model, with neither model including the crossover from one to the other. In their recent work, the same group extended the model to cover the entire adsorption motion [90], as well as updating the fitting parameters to better reflect the physical system.

This model resulted in a better fit to the experimental data of Kaz et al. [90], covering the entire trajectory. In this model, the potential energy barrier of a defect $\Delta U = \beta\gamma A_d$, where β is a shape factor of order 1. More specifically, β is the ratio of the actual defect area to the resulting disturbance of the interface, given by:

$$\beta = \frac{|\Delta A_{\mathrm{ow}} + \Delta A_{\mathrm{ws}} \cos\theta_d|}{A_d} \tag{3.16}$$

where ΔA_{ow} is the change in area of the oil-water interface, and ΔA_{ws} the change in wetted area of the solid surface. These quantities will be similar to but not necessarily the same as A_d. θ_d is the local Young's equilibrium contact angle, which may differ if local surface chemistry alters. However, this was assumed to be the same as the global equilibrium contact angle θ_{E}.

Table 3.1: Physical parameters resulting from fit of model to experimental data of Kaz et al., from [90].

Surface	A_d (nm)	$l = A_d/2\pi R$ (pm)	β
Carboxyl	9.2	1.63	0.23
Sulphate	12.9	2.34	0.41
Carboxlyate-modified	85.7	15.5	0.45

To obtain an estimate for β, the authors modelled defects as spherical caps with projected area A_d, and projected height $h_d = 0$ to $0.5\sqrt{A_d/\pi}$. This gives the range $\beta = 0.35$ to 0.2, which is in agreement with the values found through fitting to the experimental data.

To perform this fit, this model used a Langevin Dynamics simulation, and the physical quantities they found are reported in Table 3.1.

3.2 Soft Particles

3.2.1 Introduction

Soft (deformable) particles at interfaces can have some of the same behaviours as hard particles. For instance, their adsorption can be irreversible, and we can make Pickering emulsions from them. But in most other respects they are quite different. For instance, being deformable, it becomes problematic to define a contact angle made with the interface, and adsorption dynamics and energies can entirely depend upon the structure and make-up of the particle. One of the main advantages of soft particles however is their ability to be responsive. For example cross-linked polymer microgels can exhibit thermo- or ph-responsive behaviour, depending upon their polymer constituents, while also effectively stabilising emulsions. The following section introduces work on microgels as emulsion stabilisers, and is an extract from the publication 'Drainage dynamics of thin-liquid films containing soft PNiPAM microgels: influence of the cross-linking density and concentration' by Keal et al., accepted for publication in the journal Soft Matter.

Poly(N-isopropylacrylamide) (PNiPAM) thermoresponsive or pH sensitive microgel particles have recently been shown to be promising systems to stabilise responsive emulsions [13, 30, 31, 74, 76, 78, 79]. These particles are surface active and spontaneously adsorb to liquid interfaces. The stability of microgel-stabilised emulsions depends upon their cross-linking density [29, 30], their protonated state [13, 79], and temperature [68, 76]. Conversely, electrostatics has no impact on the microgel organization at the oil-water interface, nor on emulsion stability [71]. The mechanisms for emulsion stabilisation and destabilisation are not well understood and are the object of intense research, the results of which were summarized in recent reviews [26, 94, 96].

Recent studies have focused on the adsorption kinetics and conformation of particles in emulsions and at model interfaces. Unlike usual hard colloidal particles, soft microgel particles can deform as they adsorb at interfaces and their conformation is theoretically governed by a balance between bulk elasticity and surface tension [72,102]. Experimentally, Cryo-SEM images of emulsion droplets have shown that PNiPAM microgel particles can spread as they adsorb at the oil-water interface at low surface coverage and adopt a 'fried-egg' structure [14, 29, 30, 52, 74, 99], illustrated in Figure 3.13. This conformation is due to the fact that the cross-linking density of these microgels is not homogeneous and decreases toward the periphery of the particles. Therefore they have a core-shell structure where the core is more strongly cross-linked and less deformable than the corona, which is composed of dangling PNiPAM arms. This is illustrated in Figure 3.14, which shows the polymer concentration density profile for a PNiPAM microgel obtained with small-angle neutron scattering [99].

Moreover Geisel et al. showed experimentally that the hydrated cores protrude into the oil phase [41, 42], illustrated in Figure 3.15. As the cross-linking density of such microgels decreases (more deformable microgels) it has been shown that their packing at droplet interfaces (center-to-center distance) does not vary, whereas the interpenetration of the dangling chains increases [29,30].

3.2.2 Adsorption kinetics and particle conformation at interface

Several studies have focused on the spontaneous adsorption of microgels in model geometries, using particle tracking techniques at a flat interface [20, 119], the pendant drop method [15, 27, 44, 76,

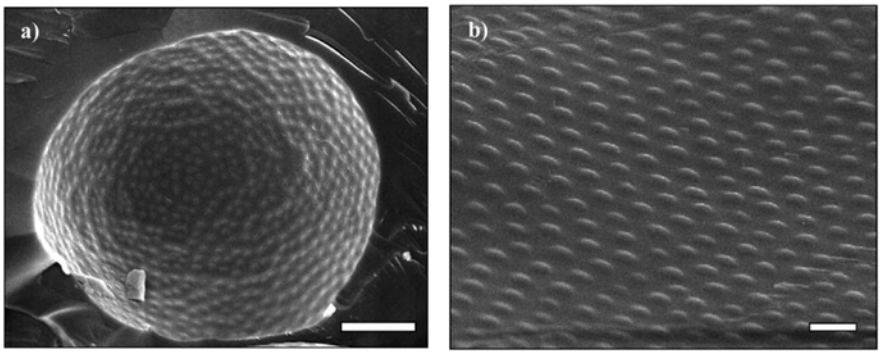

Figure 3.13: Cryo-SEM images of 700 nm microgels at the water-dodecane droplet interface, from [30]. **(a)**: Microgels arranged on the interface of a droplet. Scale bar 5 µm. **(b)**: Microgels appear flattened and lens-shaped at the interface. Scale bar 1 µm.

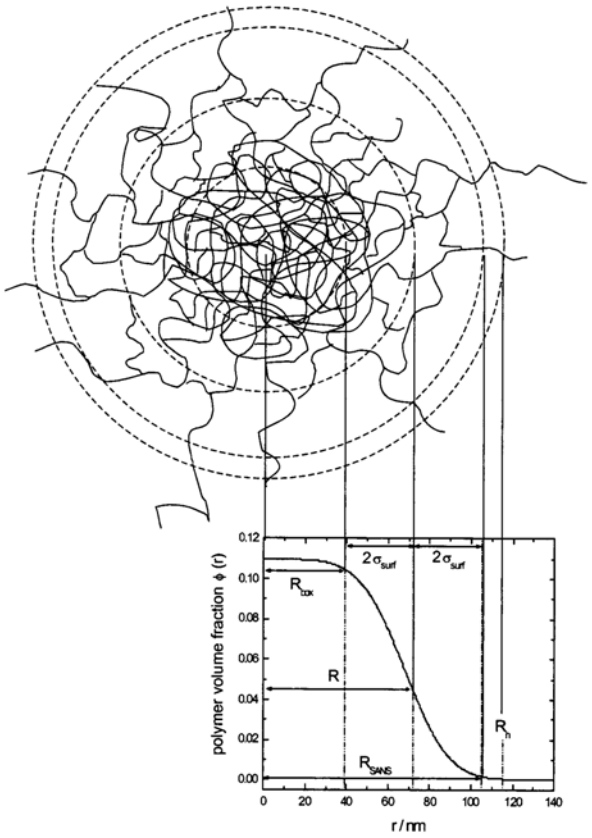

Figure 3.14: Schematic of a microgel, along with its concentration profile measured through small-angle neutron scattering (SANS), from [99].

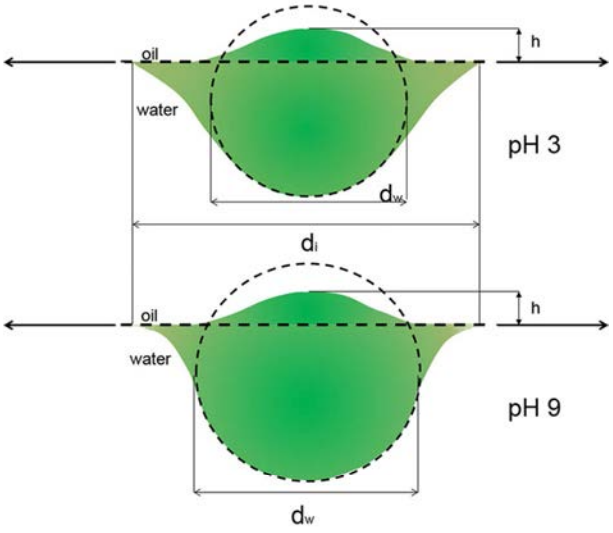

Figure 3.15: Schematic representation of PNiPAM-co-PMAA microgels in profile at the oil/water interface, with protrusion height measured through Fresca Cryo-SEM [42]. Increasing pH causes the microgels to become more rigid and spherical.

87, 119] or Langmuir trough experiments [27, 43, 87]. Interestingly, particle tracking studies performed recently showed that the particles eventually form clusters [20, 53], the origin of which is still unknown.

Spontaneous adsorption studies have revealed the influence of the microgel concentration on the adsorption kinetics [27, 67, 87, 119]. Figure 3.16 shows the change in surface tension over time as microgel solutions of various concentrations adsorb spontaneously to the interface of a water droplet in air, measured with pendant drop tensiometry [87]. At high microgel concentrations the adsorption kinetics are very fast leading to large interfacial tension reductions and consequently to high surface pressures.

In turn, the adsorption kinetics and the concentration control the conformation of the particles. At low surface pressures the microgel particles reach a 'spread' conformation, while at high surface pressures the microgels are forced into more densely packed layers [87].

3.2.3 Influence of conformation on elasticity

The conformation of the particles influences their interpenetration and therefore the surface viscoelasticity as well as the stability of emulsions with respect to handling. Combining Langmuir trough compressions and oscillating bubble experiments Pinaud et al. have found that at low surface coverage the surface dilational elasticity is low as the particles are far from each other in a spread conformation [87]. As the surface coverage increases, particles come into contact and the surface dilational elasticity reaches a maximum as particles become interpenetrated; at larger surface compressions the surface dilational elasticity decreases because some polymer segments of the particles can partially desorb upon compression.

The role of cross-linking density on the dilational elasticity and compressibility of the layers is not trivial. Pinaud et al. [87] found that the cross-linking density influences the compressibility only

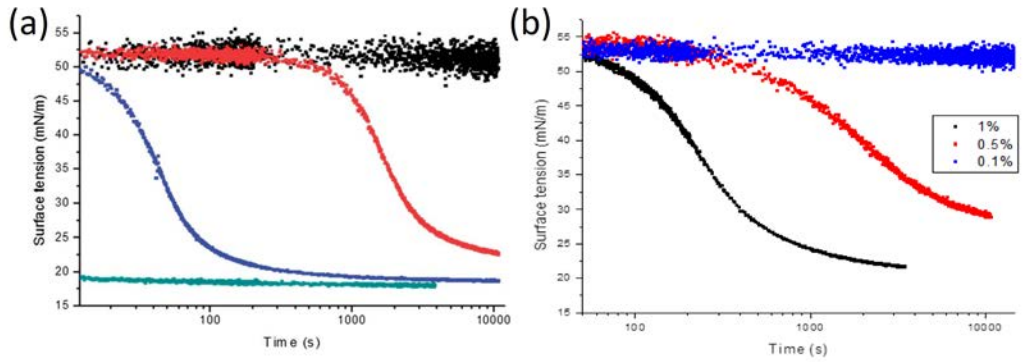

Figure 3.16: Pendant drop tensiometry measurements of the spontaneous adsorption of PNiPAM microgels at various concentrations to the air-water interface, from [87]. **(a)**: Microgels with cross-linking density 1.5mol% BIS. **(b)**: Microgels with cross-linking density 5mol%. The harder, higher-crosslinked microgels show markedly slower adsorption kinetics.

at large compressions. Consistently, the dilational elasticity of microgel layers, which is obtained at low deformations using the pendant drop method, was shown not to depend on the cross-linking density [87]. However Geisel et al. [45] studied the compression of core-shell and hollow shell microgel particles in a Langmuir trough and found that at low compressions, the cross-linking density decreases the compressibility of the layers while at large compressions, larger cross-linking densities favour large compression elasticity. This non trivial behaviour is due to a competition between desorption of polymer segments at low compression and network deformation at large compression. Brugger performed surface elasticity measurements of interfaces covered with microgels composed of NiPAM and acrylamide monomers which are charged at high pH and uncharged at low pH [15]. They found that the surface shear and dilational elasticity is larger at high pH where the particles are charged and the microgels are partially interconnected, providing a soft gel-like interface.

3.2.4 Influence of conformation on bridging in emulsions

The conformation of the microgel particles also plays a role on the behaviour of thin liquid films and bridging phenomena in emulsions. Studies performed on emulsions stabilised by microgels have revealed that such emulsions often exhibit adhesion between drops arising from bridging of the surfaces of two neighbouring drops by particles shared between the two droplets interfaces, as evidenced by Cryo-SEM experiments. Figure 3.17 shows Cryo-SEM images of droplet interfaces covered with microgels for solutions of different cross-linking densities. The adhesion of droplets depends on numerous factors such as:

1. The cross-linking density. At fixed microgel size the more cross-linked the microgels the more adhesive the drops [29].
2. The microgels size. The larger the microgels the more adhesive the drops [28].
3. The stirring energy. A higher energy input favours adhesion [15]

All these parameters have been proposed to merge into a single statement "adhesion is promoted by a low polymer density and the existence of polymer density fluctuations parallel to the surface" [96].

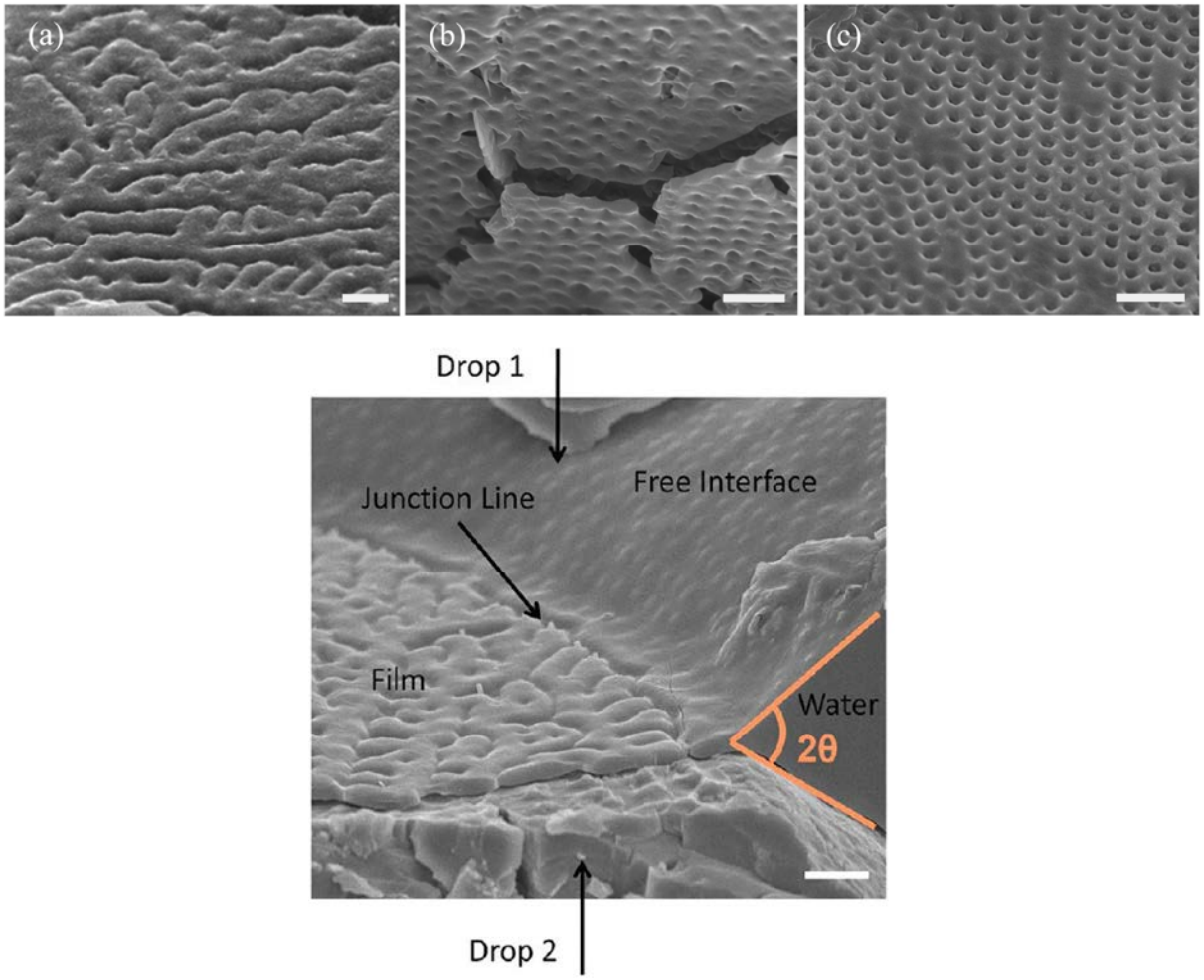

Figure 3.17: Cryo-SEM images of films formed between microgel-stabilised dodecane droplets, from [29]. Top: Films between droplets showing hexagonal arrangement of bridging points, increasing levels of bridging with increasing microgel cross-linking density, with (a) and (b) at 3.5mol%, and (c) at 5mol%. Scale bars 5 µm.
Bottom: Microgels can be seen arranging on the surfaces of the droplets, as well as within the film. Pinched points may show bridging of single microgels shared between both droplet interfaces. Microgel cross-linking density 2.5mol% Scale bar 2 µm.

Chapter 4

Water/Water Interfaces

Contents

This chapter will introduce Aqueous Two-Phase Systems (ATPS). These systems arise when a mixture of two aqueous solutions, either of colloids, polymers or surfactants, phase separates. This separation can be associative as in complex coacervation, whereby one phase is rich in both components and the other in solvent, or dissociative where two phases form each rich in one component. The properties of such systems are very distinct from molecular phase-separated systems. However, the qualitative behaviours are similar. The interactions causing separation are weaker (hence a lower surface tension), viscosities tend to be higher (from 10 mPa s to 1500 mPa s), and the systems' components larger (few nm to 500 nm). As a result the timescales and lengthscales of phase separation phenomena tend to be orders of magnitude longer than molecular systems. Thus ATPSs can be used as model systems to study very fast or small-scale interfacial phenomena experimentally.

In reality however, ATPSs are ternary systems with water as a solvent, and the relative quantities of each of the three components are of key importance in almost all system properties. For all ATPSs, at sufficiently low concentration to be below a critical concentration c_{crit}, the entropic cost of demixing is too great and only one phase exists. Above this concentration, surface tension between phases tends to scale with concentration within a given system. Additionally, the interface is much broader than molecular systems, which in oil/water is of the scale of the diameter of the water molecule (0.3 nm) compared to a single particle/polymer in ATPSs being on the 5 nm to 500 nm scale, but this interfacial widht too depends upon the distance from critical concentration, with larger concentrations having narrower interfaces.

Figure 4.1: From left to right, aqueous two-phase systems (ATPS) consisting of polymer/surfactant phases, polymer/polymer phases, polymer/colloid phases.

4.1 Demixing of Polymer Systems

Compatibility or incompatibility of combined polymer solutions is determined by whether, on mixing, the Gibbs free energy of the solution would reduce compared to the systems staying separate, or not. The Gibbs free energy is given by $G = H - TS$, where H is the enthalpy, T the temperature and S the entropy of the system. Enthalpy is the termodynamic energy of the system, containing both its internal energy U and the volume and pressure of the system, $H = U + pV$. In turn, U contains all the interaction energies between momomers of each polymer type, and with the solvent. If this interaction energy is more repulsive between different momomers than like monomers, the enthalpy will favour phase separation. The entropy S contains information about the possible configurations of each polymer, and is maximised when polymers are as free as possible to translate and rotate around the system.

On combination of the polymers, there will be a change in the energy of the system, ΔH_{mix}, and a change in the entropy of the system, ΔS_{mix}. The resulting change in free energy ΔG_{mix} must be < 0 for mixing to occur; otherwise two phases will emerge at equilibrium:

$$\Delta G_{\text{mix}} = \Delta H_{\text{mix}} - T\Delta S_{\text{mix}} < 0 \tag{4.1}$$

Usually, the entropy of a mixed phase is larger than phase-separating phases, as the polymers have more freedom to move when not confined to one region. To achieve phase separation therefore there must be sufficient change in enthalpy, ie. sufficient unfavourable interaction between opposing polymers to overcome this entropic cost.

To calculate the interactions (and hence energies) and the entropies of a system wherein polymers and solvent are completely free to move would be effectively impossible, as in reality every molecule in the system interacts with every other one. So a simplification is made whereby monomers and solvent molecules are arranged on a 3-dimensional grid, and a mean field approximation is made for the interaction based on only the nearest neighbours on the grid. This is the Flory-Huggins mean field theory.

To model the interactions of ternary mixtures of two polymers and a solvent, it is most convenient to use the so-called 'blob' model. This is an extension of a Flory-Huggins thermodynamic model in which the polymer is coarse-grained as a collection of N_b 'blobs' of size ξ, arranged according to a self-avoiding random walk on a 3D grid. This simplification relies upon the assumption that the

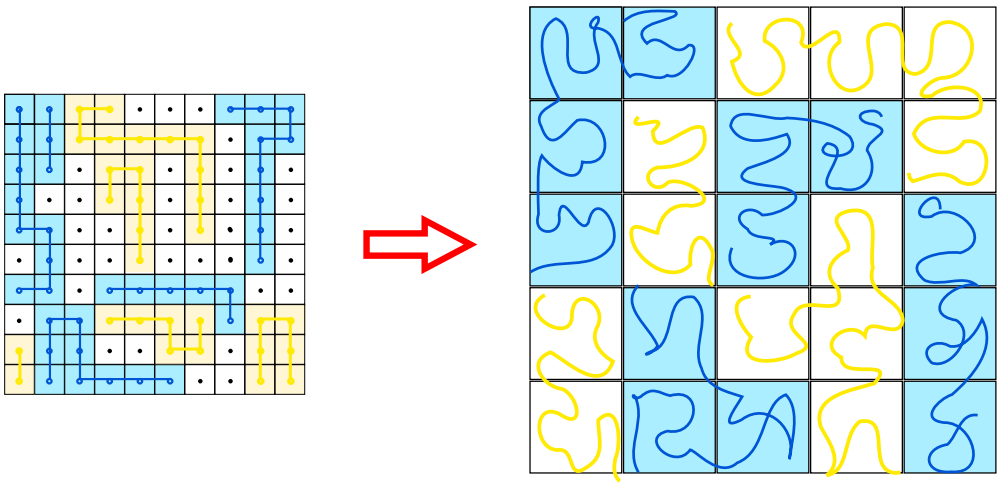

Figure 4.2: Left: A 2-dimensional example of two polymers arranged on a grid, with free space taken up by solvent. Blue represents polymer 1, yellow polymer 2, and the black dots represent solvent molecules. Right: The system is coarse-grained as a collection of polymer 'blobs' that undergo a self-avoiding random walk on the 2D grid. As the chains are hydrated by a 'good' solvent, the solvent is now only represented in the size of the blobs.

polymer is in the semi-dilute regime, in 'good' solvent conditions to avoid itself on short scales, but has the consequence that the solvent can be effectively ignored on longer scales when calculating the free energy [65, p. 169], only contributing in the size of a blob, $\xi = \xi(c)$, where c is the polymer concentration. The interactions between all polymers are reduced to a dimensionless interaction parameter representing the interaction between blobs of opposite polymer.

In such a model, the volume fraction of one polymer is represented by ϕ, and the other $(1-\phi)$, as the solvent is contained within the blobs. The resulting free energy equation is then (per unit volume, in units of $k_\mathrm{B}T$):

$$\frac{G_\mathrm{blob}}{Vk_\mathrm{B}T} = \frac{1}{\eta(c)^3}\left[\frac{\phi}{N_b(c)}\log\phi + \frac{1-\phi}{N_b(c)}\log(1-\phi) + u(c)\phi(1-\phi) + K\right] \tag{4.2}$$

Here K is a constant relating to the free energy of monomers within a blob. The concentration-dependent size of a blob is:

$$\eta(c) = 0.43R_g\left(\frac{c}{c^*}\right)^{\frac{\nu}{1-3\nu}} \tag{4.3}$$

where in a good solvent, the radius of gyration $R_g = bN^\nu$, where b is the Kuhn length and $\nu = 3/5$. c^* is the overlap concentration.

The energy of interaction $u(c)$ is approximated as:

$$u(c) \approx u_\mathrm{crit}\left(\frac{c}{c_\mathrm{crit}}\right)^{\frac{\chi}{3\nu-1}} \tag{4.4}$$

where $\chi = 0.22$ for a good solvent. c_crit is the critical demixing concentration, from experiment, and u_crit is defined as the value of the energy at this concentration.

Hence, for a given starting concentration c, polymer 1 volume fraction ϕ, and temperature T the state of the system is found by minimising the free energy, equation 4.2.

$$\frac{d\Delta G_{\text{mix}}}{d\phi} = 0 \quad \text{where} \quad \frac{d^2\Delta G_{\text{mix}}}{d\phi^2} > 0 \tag{4.5}$$

The solution to this equation will have one value if mixing is favoured, or two values if phase separation is favoured. Figure X demonstrates 1-value and 2-value minima of the free energy, in this case dependent upon temperature. A system that begins at, for example, $\phi = 0.5$ at $T = 250\,\text{K}$ will separate into two phases, one of low ϕ, one of high.

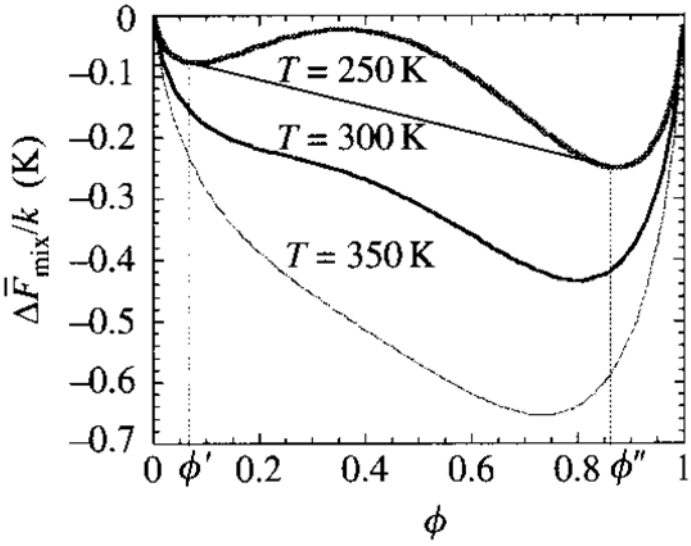

Figure 4.3: Free energy of system vs. polymer 1 volume fraction for a temperature-dependent system, from [95]. At low temperatures two minima exist, meaning phase separation is possible. At higher temperatures only one minimum is present, meaning the system will mix.

But whether a particular system demixes or not depends upon where upon the free energy diagram its initial composition lies, and what the value of the second derivative of the free energy $\frac{d^2/dG}{d\phi^2}$ is at that point. An initial system, with composition ϕ_0 and free energy G_{mix}, may try to separate into two phases due to local fluctuations in composition. These two phases, α and β, will have a composition ϕ_α and ϕ_β and free energy g_α and g_β, respectively. The stability of the system against these fluctuations, ie. whether the system will mix again or whether phase separation will be started depends on whether the total free energy for two systems,

$$G_{\alpha\beta} = G_\alpha\phi_\alpha + G_\beta\phi_\beta \tag{4.6}$$

is greater or less than the free energy of one mixed system, G_{mix}. This can easily be determined, as is demonstrated in Figure 4.4, by whether the local value of the second derivative of the free energy is positive or negative. For a positive second derivative, the splitting of the phases will result in a higher free energy. Such states are (locally) stable. Whereas for a negative second derivative, phase separation will take place.

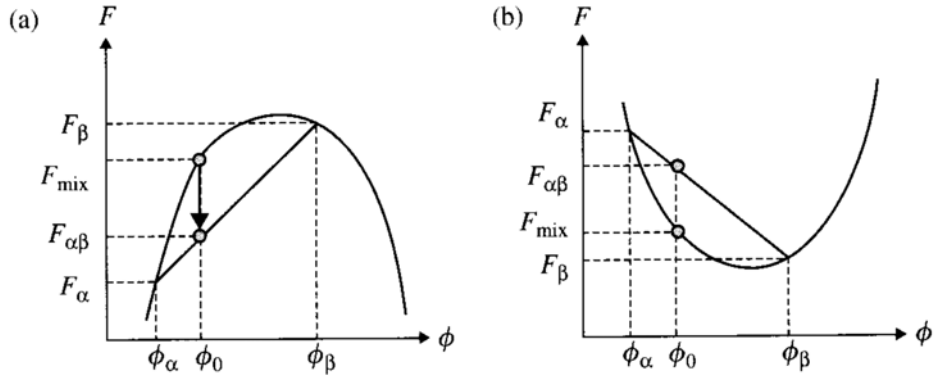

Figure 4.4: From [95] Left: Unstable system. Upon phase separation, total system free energy $F_{\alpha\beta}$ is lower than initial free energy F, meaning separation is favourable. Right: Stable system. Phase separation causes rise in total system free energy, so mixing is favourable.

This can lead to metastable states. For example, if a system began with a composition of $\phi = 0.1$ at $T = 250\,\mathrm{K}$ in Figure 4.3, the second derivative of the free energy is positive and the system would remain in one phase against small compositional fluctuations, despite not representing the global minimum of the free energy.

4.1.1 Polymer/Polymer Systems

The most widely-studied ATPS is the demixing polymer solution. This section will explore some of the key research performed in understanding and quantifying the demixing phenomena introduced above for these systems, and some of the unique properties of ATPSs. Polymer systems tend to be among the higher surface tension ATPSs, where surface tension between the phases is typically within the range $0.5\,\mu\mathrm{N/m}$ to $500\,\mu\mathrm{N/m}$ [118], though this is still a minimum of two orders of magnitude smaller than oil/water. Further, the solvent is continuous throughout both phases and the interface is permeable, hence diffusion of ions is unimpeded [115]. If either polymer phase is charged, it is then possible for there to be an imbalance of charge across the interface at thermodynamic equilibrium, leading to a so-called Donnan potential [112–115], discussed in greater detail later.

There are numerous incompatible polymer systems available, both in the form of biopolymers and synthetic polymers. The demixing of polysaccharides and proteins was found to be so common as to almost be a general property of proteins. Grinberg et al. provide an extensive list of phase-separating systems in their 1997 review [47].

Another polymer pairing of particular interest as a model system is dextran / poly(ethylene) oxide (PEO) [24, 33, 37], as both are neutral in charge, and optially clear. For systems where one polymer is charged however, as is the case for many polysaccharide/protein pairings, dextran and non-gelling, cold-water fish gelatin are a more appropriate model system, as fish gelatin is charged for a large pH range. Fish gelatin does not gel at room temperature ($T_{\mathrm{gel}} \approx 10\,^\circ\mathrm{C}$). This system is the particular focus of our work.

Much research has already been performed with this system, this is partly due to favourable properties for a model system, namely optical clarity and Newtonian shear behaviour across most experimentally accessible shear rates and concentrations. The importance of optical clarity is that

any turbidity of the system can be ascribed to the presence of emulsion droplets, scattering light. The interest is also partly due to the relevance of such food-grade biopolymers to potential food technology applications of a water/water emulsion.

Recent publications by Vis et al. explored the interfacial thermodynamics of fish gelatin / dextran mixtures, focusing mainly on the influence of the charge of the fish gelatin polymer upon the system. As they bear relation to the current work, they will be discussed in greater detail in Section 4.2.

4.1.2 Polymer/Colloid Systems

Polymer/Polymer solution systems are not the only aqueous phase-separating mixtures. Mixing colloids and polymers can induce a depletion-driven phase separation into a colloid-rich and a colloid-poor region. This has been theoretically predicted since the 1950s [5] and explored experimentally since the 1980s [97], though it is commonly observed in life through flocculation of particles in water-based adhesives, inks and coatings [97].

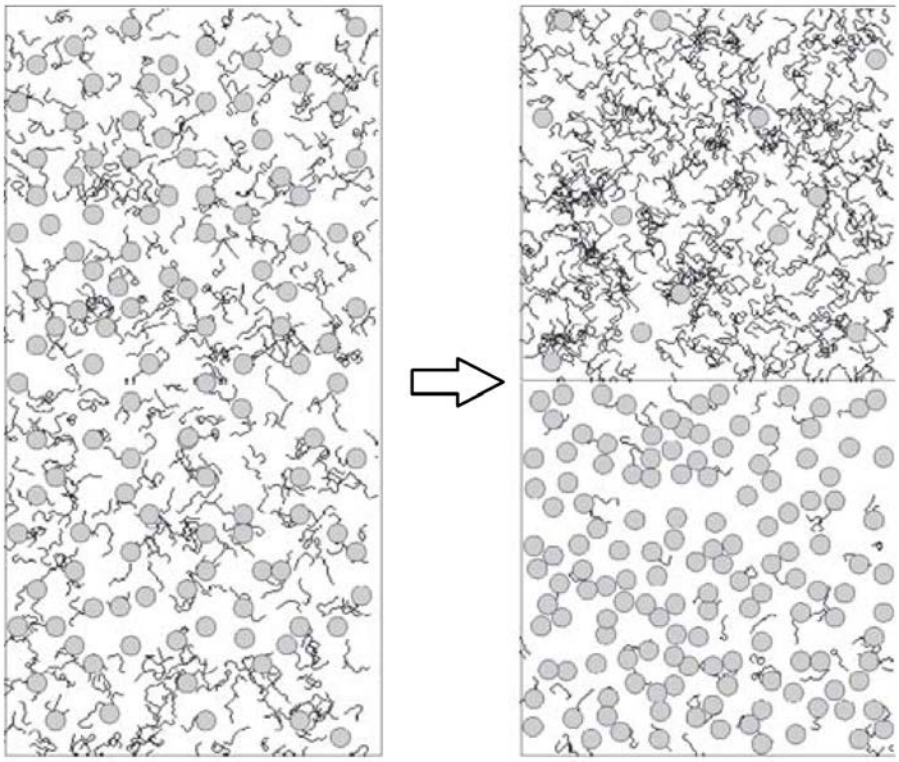

Figure 4.5: An aqueous solution of colloidal particles and non-adsorbing polymers demixes into a colloidal-rich and a colloidal-poor region. Demixing is driven by an attractive depletion interaction between the colloids. Adapted from [66]

The mechanism of phase separation in these systems is an attractive depletion force between the colloidal particles, driven by the polymers [57, 58]. Depletion arises when the polymers do not adsorb to the particles, and are sterically (or otherwise) unable to enter a region around each particle roughly equal to the radius of gyration of the polymer R_g [65, p. 73], with a cost to translational entropy. The range of this attraction is therefore set by the polymer size, so large polymers ($R_g \approx$

50 nm [3, 25] to 250 nm [56, 108]) are often used for a long-range interaction in phase separating systems.

The colloidal particles used, also often of the order of one hundred nanometers in radius, are much larger than the constituents of a polymer/polymer system. The surface tension in colloid/polymer systems far away from the critical concentration scales as [1]:

$$\gamma \propto 1/D^2 \tag{4.7}$$

where D is the colloidal particle diameter. As such, colloid/polymer systems exhibit even lower interfacial tensions than polymer/polymer systems, measured in µN/m, or even nN/m [3]. Hence, no reported works attempt to stabilise these systems through adding surface-active components to the system. Instead, the low surface tension and excellent visibility of fluorescent colloidal particles in confocal microscopy are exploited to observe interfacial phenomena at much longer lengthscales than those of molecular phase-separating systems. The colloidal/polymer interface is used as a model system to study general interfacial phenomena, especially in confined systems such as microfluidics [108]. Additionally, the process of spinodal decomposition under various conditions can be easily studied with this system [56–58].

A useful example of the accessibility of interfacial phenomonena is that the ultra-low surface tension of this system renders the random thermal motion of the interface, thermal capillary waves, visible in real space, using confocal microscopy [3, 25]. Figure 4.6 shows such interfacial motion for different concentrations. The closer to the critical concentration of mixing, the larger the thermal motion of the interface.

Additionally, the 'slow motion' dynamics of such low-tension systems enable observation of coalescence of droplets with the bulk phase at sufficient time resolution to isolate individual regimes of the process. This is again noteworthy, as usually thin film rupture is an extremely fast process. In this system however, the process takes several seconds. As a result of their observations, the authors conclude that firstly, hydrodynamics determine the drainage rate of the thin film separating the droplets, till it reaches a minimum thickness of the order of 1 µm. At this lengthscale, random capillary waves become significant. The likelihood of a 0.5 µm amplitude bulge on one interface meeting a 0.5 µm amplitude bulge on the other, breaching the film, becomes significant over minutes. Once this occurs, hydrodynamics again determine the drainage rate of the droplet into the bulk fluid.

Furthermore, the interface is sufficiently low tension that it can actually be manipulated directly with optical tweezers [108]. A well-defined force can be exerted perpendicular to the interface through a powerful laser incident parallel to it. Figure 4.7 illustrates the technique for two colloid/polymer systems, one far and one near to the critical concentration.

This remarkable technique allows studying of the shape of the interface under a given force, the subsequent relaxation of the interface, and 'snapping off' of droplets of the trapped phase. These measurements can be performed in confined systems to study the effect of confinement upon the interface.

Using this system a technique was developed for measuring the interfacial tension of ultra-low tension systems [1], for which equipment such as the Langmuir Trough or Pendent Drop is difficult or impossible to use. In this method, the static interfacial profile between two bulk phases against the flat wall of a narrow rectangular cuvette is imaged using a horizontal microscope, and analysis

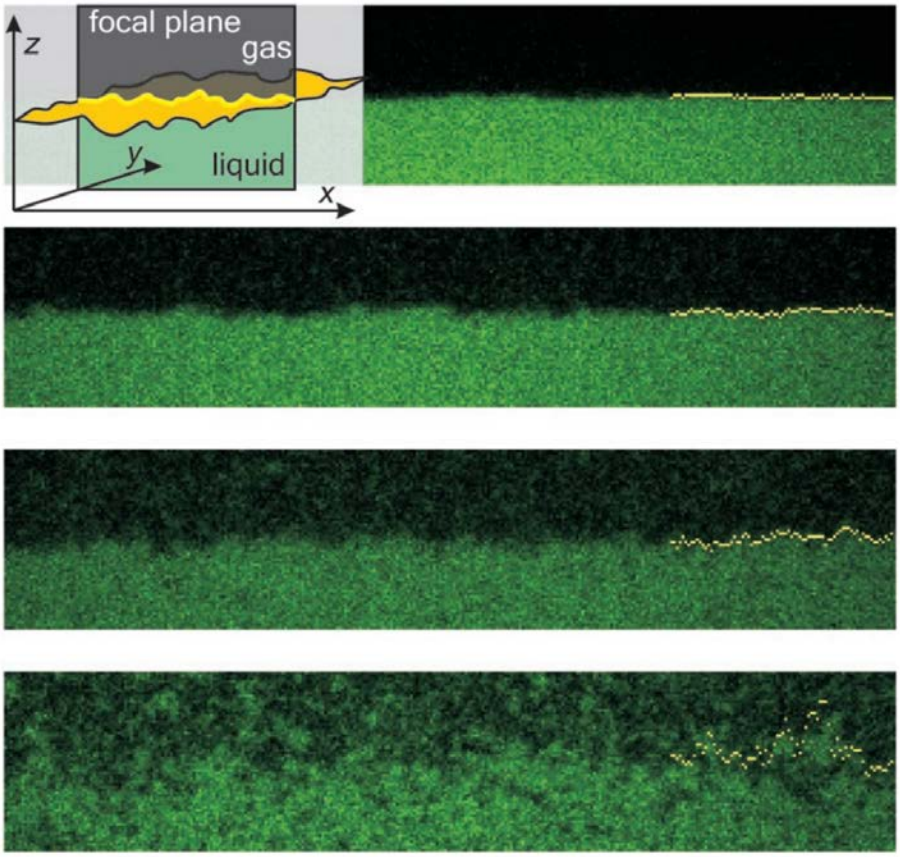

Figure 4.6: Thermal motion of the interface between a phase rich in colloidal particles and one poor in colloidal particles, from [3]. Each successive image moving downwards shows a system closer to the critical point of mixing. As such the surface tension lowers, and thermal motion becomes more noticeable.

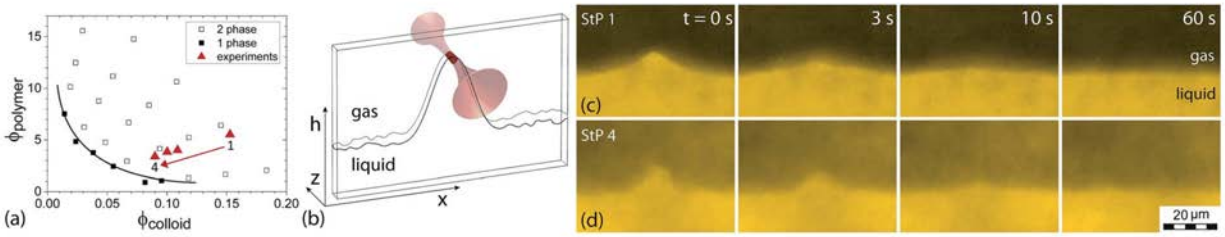

Figure 4.7: The trapping of the liquid/liquid interface of a colloid/polymer demixed system using a high powered laser parallel to the interface, from [108]. (a) Phase diagram of mixing of the polymers and colloidal particles, showing the state points (1-4) of the experiments performed. (b) Schematic of the system. (c) Optical trapping and relaxation of the interface at state point 1, far from the critical point. Laser is turned off at t=0, and interface relaxes back to equilibrium shape. Yellow shows fluorescent colloidal particles. (d) At state point 4, closer to the critical point, the interface takes longer to relax.

of the shape yields the capillary length, $l_c \equiv \sqrt{\gamma/(\Delta\rho g)}$. With the density difference $\Delta\rho$ between the phases measured, the interfacial tension can be known. This technique is illustrated in Figure 4.8.

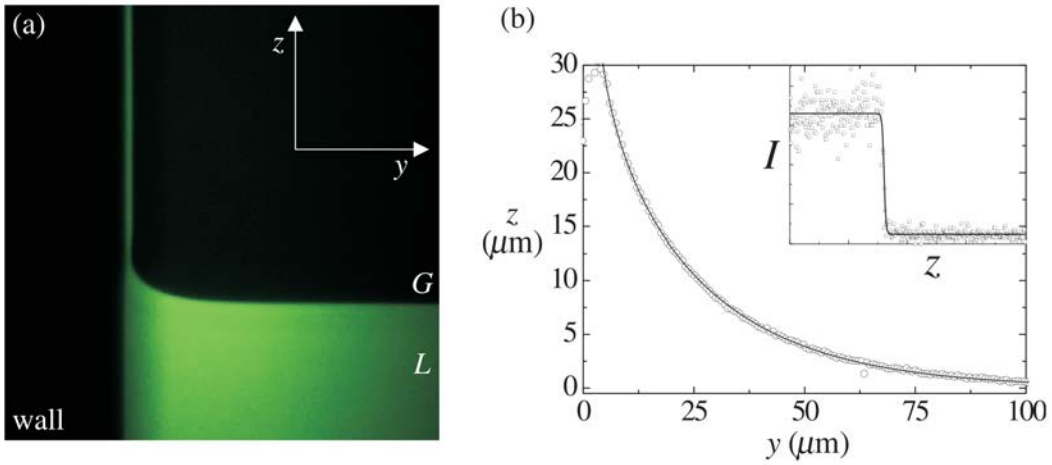

Figure 4.8: Measurement of the interfacial tension between a phase rich in fluorescent PMMA colloidal microspheres and a phase rich in polystyrene polymer, from [1]. (a) The shape of the interfacial profile inside a narrow glass capillary vessel is imaged with a horizontal confocal microscope. The theoretical fit to the data shown as a straight line in (b), and the extracted profile as circles. The inset shows the fitting of a hyperbolic tangent to the data.

4.2 Properties of the Fish Gelatin/Dextran Interface

This section will investigate specific properties of the Fish Gelatin / Dextran interface as reported in literature. The first important property to discover is the phase diagram. When working with ATPSs, knowledge of the phase diagram of mixing is essential. This indicates the minimum concentration required for phase separation (c_{crit}), the concentrations of resulting phases once two polymer solutions reach thermodynamic equilibrium, and allows direct calculation of the surface tension of a given system. An initial system, with a given weight % dextran and weight % fish gelatin, called a 'state point', will split into two points connected by a tie line. Tie lines are usually parallel for all state points, and systems prepared on the same tie line will have phases of the same composition after separation. Surface tension scales with the length of the tie line.

To understand the behaviour of polymers in the system, and have some predictive tools for system properties such as the phase diagram, interfacial tension and charge across the interface, a theoretical model is important. Additionally some properties of the water/water interface, such as the interfacial concentration profile (and hence interfacial width) are of importance to studies of dynamics at the interface but have yet to be measured experimentally [110]. The theoretical model used in literature to model these polymer/polymer systems is the so-called 'blob' model introduced previously.

An additional contribution must be added for the case of charged polymers (as in fish gelatin). The diffusion of counterions from polymer solutions and ions from added salty is free across the interface, and polymer charge may cause them to distribute unevenly throughout the system. This

has an entropic cost, and that can have a significant influence on the phase diagram, demonstrated in Figure 4.9, taken from [115].

4.2.1 Phase Diagram

A phase diagram can be obtained from the model by equating chemical potential and pressures of the coexisting phases. Minimising the free energy provided by the model described gives the phase-separated phase concentrations.

Shown in 4.9 are experimental phase diagrams for a fish gelatin / dextran system, where part (a) shows the influence of pH, and part (b) the influence of salt. These were was obtained through mixing dextran (molecular weight 100 kDa) with fish gelatin (molecular weight ≈ 100 kDa), including NaOH and HCl to adjust pH as required, and KCl to adjust the salt concentration. No buffer was used as gelatin itself acts as a buffer. The samples were mixed and then centrifuged. The concentrations of each polymer in each phase were measured with polarimetry, which provides a very accurate measurement. The resulting phase diagram matched well with theoretical predictions from the blob model.

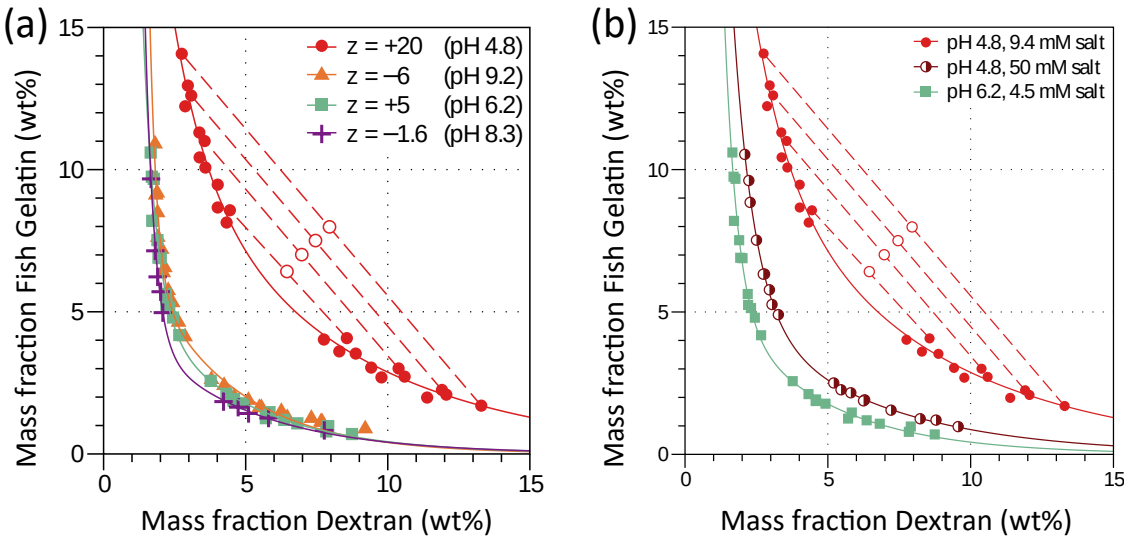

Figure 4.9: Experimental phase diagrams for a demixing fish gelatin / dextran system, from [109], showing the influence of pH (a) and salt (b). z indicates the electronic charges per polymer.

Influence of Salt

From the phase diagram (Figure 4.9b), one observation of particular importance is that when salt is added to the system, the phases become more pure, ie. each polymer-rich phase has a lower fraction of opposing polymer.

4.2.2 Surface Tension and Donnan Potential

To measure surface tension experimentally, Vis et al. used the method described by D. Aarts et al for use with colloid/polymer ATPSs (as described in [1]), illustrated for a polymer/colloid interface in Figure 4.8.

As is typical for water/water systems [98], measured surface tension γ scales as a power law in the tie line length (TLL):

$$\gamma \sim \mathrm{TLL}^{3.33} \tag{4.8}$$

as shown in Figure 4.10a. However, as also shown in Figure 4.10a, there is considerable spread of the data depending on the pH of solution, meaning that the TLL is not the sole determining factor for the surface tension.

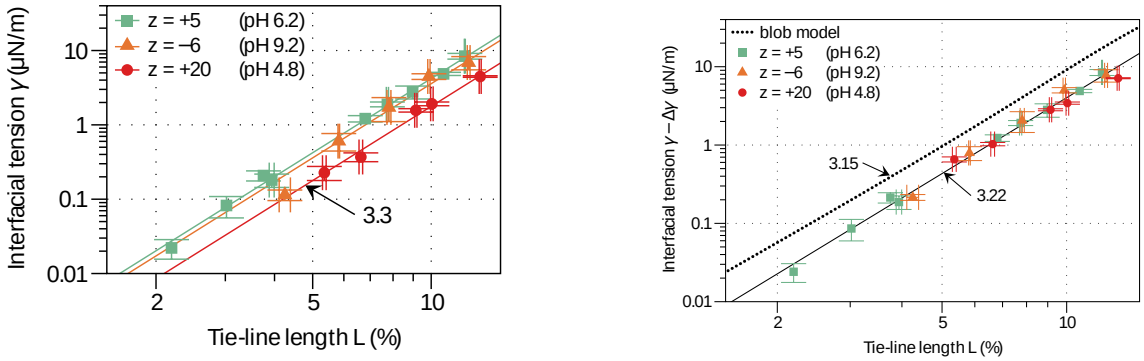

(a) Semilog plot of surface tension vs tie-line length (TLL) for polymers of differing charge.

(b) Semilog plot of surface tension vs tie-line length (TLL) for polymers of differing charge, removing the contribution of the Donnan potential to the surface tension. The lines collapse to a single master curve.

Figure 4.10: Surface tension scaling with tie line length, with and without the contribution of the Donnan potential, from [114].

The cause of this variability was investigated by Vis et al., and found to be due to the charge of the fish gelatin polymer. In an ATPS, when one of the polymer phases is charged, and the interface is permeable to ions, a potential difference can arise across the interface [112], called a Donnan potential, which results in an electrostatic contribution to the surface tension.

Vis et al. measure the Donnan potential for various concentrations of fish gelatin / dextran solution, at different pHs. As a polyelectrolyte, the charge of fish gelatin is pH-dependent, being negative at low pH, with an isoelectric range around pH 7-9, shown in Figure 4.11. The Donnan potential was found to scale linearly with tie-line length.

Vis et al. then derive theoretically the electrostatic contribution of this potential to the interfacial tension. The contribution, $\Delta\gamma$, is well approximated by Equation 4.9.

$$\Delta\gamma \approx -\frac{kT\kappa}{16\pi\lambda_B}\Phi_D^2 \tag{4.9}$$

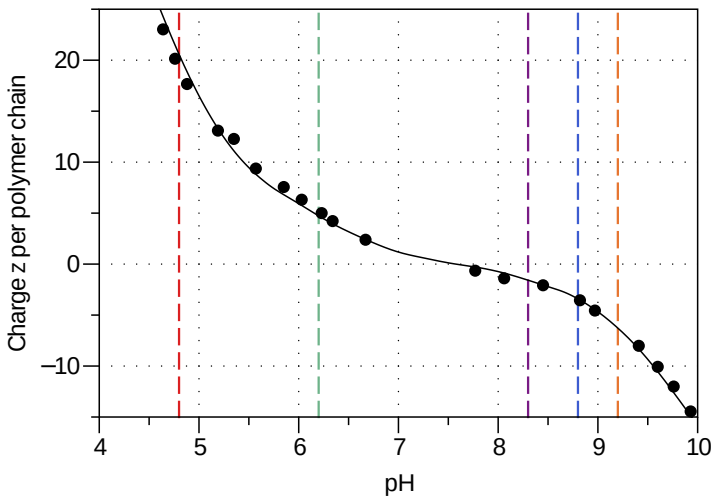

Figure 4.11: Charge of fish gelatin for a given pH. From [109].

assuming relative permittivity is the same in both phases, where λ_B is the Bjerum length, given by $e^2/(4\pi\epsilon\epsilon_0 k_B T)$, κ is the Debye screening constant given by $\sqrt{8\pi\lambda_B c_s}$, where c_s is the salt concentration.

Accounting for this adjustment, the surface tension is now given by:

$$\gamma = \gamma_0 + \Delta\gamma \tag{4.10}$$

Removing this adjustment factor $\Delta\gamma$ given by Equation 4.9, the base surface tension values γ_0 for each pH collapse into a single master curve, as demonstrated in Figure 4.10b. The slope of γ_0, which also scales as a power law in TLL, is given by $TLL^{3.22}$.

4.2.3 Interfacial Profile

Another significant reason for theoretically modelling the water/water system is to understand the concentration profile of polymers across the interface. Unlike oil/water where the interfacial width is around the diameter of the water molecule (0.3 Å), the concentration profile of a water/water interface is much more gradual. The interfacial profile calculated through Flory-Huggins theory for a system far from critical concentration is shown in Figure 4.12.

The further the system is on the phase diagram from the critical point, the narrower the interface will be, but it will typically be of the order of tens of nanometres.

Another important feature of the water/water interface is that the overall polymer concentration drops across the interface, as shown in the top plot of Figure 4.12.

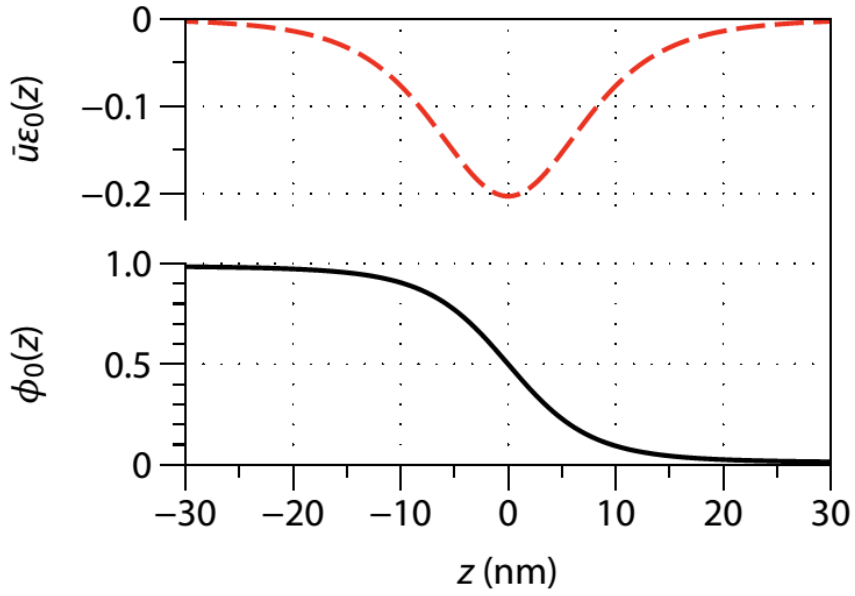

Figure 4.12: Theoretical calculation of interfacial polymer concentration profile, at high enough concentration to be far from the critical point of mixing. Top plot shows relative change in total concentration across the interface. Bottom plot concentration of one polymer component. From [109].

4.3 Stabilisation of water/water interfaces

For most emulsion applications, the stability of the emulsion is a key determining factor of its utility. Emulsions that are unstable and separate to macroscopic phases are of little use to either the food industry or for use in encapsulation or the creation of aqueous 'bioreactors' [32]. However, due to the width of the interface, conventional surfactant stabilisers cannot be used, as no surfactant is large enough for the head and tail groups to fully enter each phase. Additionally the low surface tension makes adsorption of molecular stabilisers more difficult. However, large particles are still good candidates for stabilisation. Despite the low surface tension, due to the R^2 contribution to the desorption energy large (>100 nm) particles can have desorption energies of at least many hundreds of k_BT. As such, adsorption should be irreversible, and the use of the Pickering mechanism to stabilise emulsions with a layer of solid particles becomes possible.

In this section, some of the successful and unsuccessful attempts in literature to stabilise water/water systems with the Pickering mechanism will be explored.

Firstly, in 2009 Firoozmand et. al first demonstrated the tendency of spherical amphoteric latex particles to accumulate at the interface of a gelatin / oxidised starch system [36]. They observed fluorescent particles with confocal microscopy. The system phase separates into a bicontinuous structure over the course of minutes. The presence of particles at the interface, at concentrations of less than 1% wt. particles, causes slowing of the coarsening of the microstructure, which the authors ascribe to the solid-like behaviour of an interface heavily laden with particles.

In 2011 Balakrishnan and colleagues at the Université du Maine, France observed both latex and protein particles to go to the interface of a poly(ethylene) oxide (PEO) and dextran system, also with fluorescent particles and confocal microscopy [10]. The authors explored different radii of particle as well as changing the system concentration's distance from the critical point (and hence the surface tension), and observed latex particles at the interface only for systems in which ΔG was $\approx 7 k_B T$ or larger. As such they concluded that irreversible adsorption was the driving force of particle accumulation at the interface. Using 1 µm particles they were able to observe the microscopic contact angle that a particle made with the interface, at 145° in favour of the PEO phase. However, despite good coverage of particles at droplet interfaces, coalescence of droplets was not affected by the presence of particles. Despite being dispersed in the dextran phase before emulsification, the majority of particles were observed in the bulk PEO phase afterwards, having been removed from the interface by the shear of emulsification. Due to this tendency, increasing the particle concentration did not lead to a significant increase of particle concentration at interface. The authors also measured the diffusion of particles at the interface, submerged partly in each phase. They found that an effective Stokes-Einstein equation with a mean viscosity linearly scaled between the two bulk values matched the observed trajectories.

The same group explored protein particle-stabilised PEO/dextran emulsions further in their 2013 publication [80] by adding β-lactoglobilin particles. This system lead to successful stabilisation for weeks, despite low surface coverage (<30%) of the particles. Figure 4.13 shows droplets stabilised with proteins for a variety of polymer concentrations along the same tie-line. The inverse average drop radius increased with increasing particle concentration which is an indication of the Pickering mechanism, however the relationship was not linear. The authors also investigated the influence of particle size on emulsion stability, finding an optimal particle diameter of around 200 nm for a constant protein concentration.

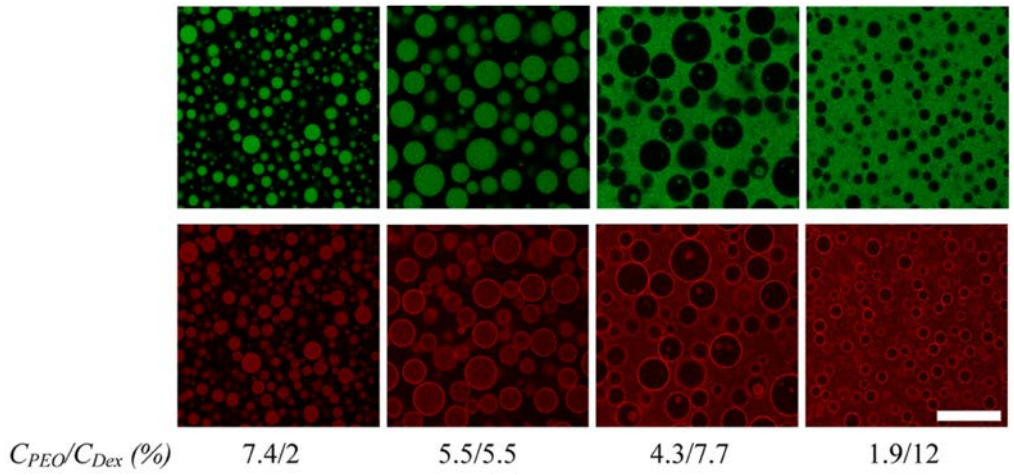

Figure 4.13: Adapted from [80]. PEO/Dextran emulsion stabilised with 300nm β-lactoglobulin particles. From left to right, different concentrations of polymer along the same tie-line. Top images show fluorescent dextran phase, bottom images fluorescent protein particles.

To come closer to a food-like model, in which proteins and oils are frequently found together, Hanazawa and Murray investigated the effect of addition of small (0.36 µm), sodium caseinate-stabilised oil droplets to a sodium caseinate / xanthan ATPS [50]. They observed a stabilising effect which they ascribe to the accumulation of oil droplets on the caseinate/xanthan interface, and the formation of a network of droplets on the interface. The same authors went on to investigate the addition of a percentage of solid oil particles (eicosane), and their influence on the interfacial viscosity of the ATPS. They observed the greatest inhibition to phase separation and the greatest interfacial viscosity at a 50%/50% liquid/solid oil mixture. They ascribe this to the formation of a network of partially coalesced oil droplets on the interface between phases, once again highlighting the importance of interfacial rheological properties in Pickering stabilisation.

A strong example of the possible applications of stable water/water systems was demonstrated by Dewey et al. in 2014 [32]. Dextran droplets suspended in a poly(ethylene)-glycol PEG matrix, stabilised with 130 nm PEGylated liposomes were used as 'bioreactors' for a ribosome cleavage reaction. This process was enabled through the free diffusion of DNA and RNA across the water/water interface, and the partitioning of the ribosome to the dextran phase.

Nguyen et al. at the Université du Maine group created pH-responsive dextran/PEO emulsions stabilised with pH-sensitive microgels. The radius of the poly(ethy acrylate-*co*-methacrylic acid-*co*-1,4 butanediol diacrylate) (PEA-MAA-BDDA) microgels had a strong pH dependence, changing quickly from $R_h \approx 60$ nm at pH ≤ 6, to $R_h \approx 220$ nm at pH ≥ 8. The microgels were observed at the interface for all pHs tested, though emulsion stabilisation for 1 week was only observed at pH 7, and the emulsion could be destabilised upon changing the pH of the PEO phase. The same group later demonstrated stabilisation of a xyloglucan/amylopectin ATPS using 500 nm β-lactoglobulin microgels [24]. These particles stabilised emulsions only for low pH (< 5.0), due to pH-dependent interactions between the protein microgels and the neutral polysaccharide xyloglucan. At low pH, xyloglucan began to adsorb onto the microgel particles, which otherwise preferred the amylopectin phase. This lead to a preferential build up of microgels at the interface between phases. At pH ≤ 3.0 however, the adsorption became sufficiently strong to reduce the contact angle of the particles,

lessening the stabilising effect. This adsorption was supposed to be hydrophobic in nature. The authors also reported the phase diagram of mixing for xyloglucan/amylopectin.

In 2015 the first stabilisation of a non-gelling fish gelatin / dextran system was demonstrated by Vis et al, using hexagonal clay nanoplates [111]. Figure 4.14 demonstrates the adsorption of fluorescent platelets to droplets of fish gelatin in a dextran-rich phase.

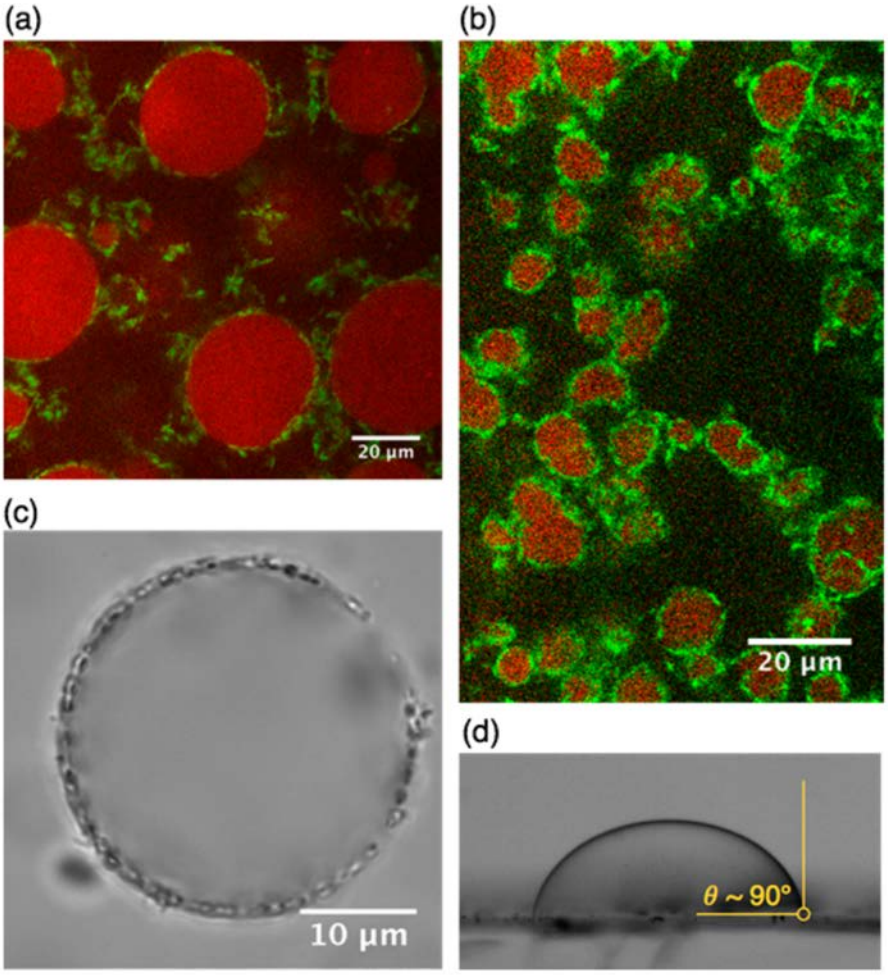

Figure 4.14: Clay nanoplates at the dextan/fish gelatin interface, from [111]. (a) and (b): Confocal microscopy images of emulsions stabilised with 0.4% and 1% respectively of 170 nm platelets (green). (c) Optical microscopy image of 700 nm platelets at the interface of a dextran-rich droplet. (d) Macroscopic contact angle of a gelatin-rich droplet in dextran-rich continuous phase on a gibbsite-covered glass substrate.

Conventional spherical colloidal particles do not stabilise this system (as shown in the present work), and stabilisation with protein particles has yet to be demonstrated either. The particular novelty of the nanoplates is their shape, which, the authors demonstrate, leads to particles laying flat at the interface, virtually irrespective of the three-phase contact angle. Figure 4.15 shows results of computer simulations to determine the particles' orientation at the interface and the resulting free energy for all possible three-phase contact angles. The free energy is even lower for most contact angles than a sphere of the same radius. Gravity-driven sedimentation of droplets is not accelerated due to a high surface-area-to-mass ratio of the particles.

Finally, another example of anisotropic colloids stabilising an ATPS was shown recently by Ped-

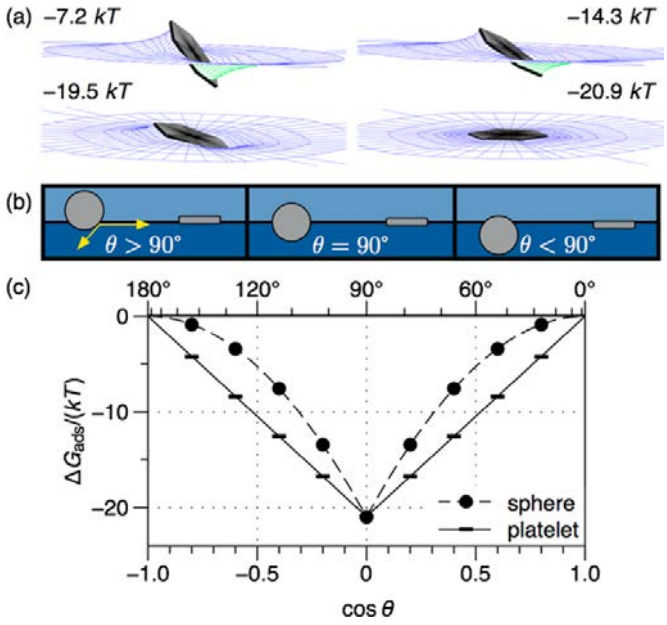

Figure 4.15: Numerical calculations of the adsorption energy of 167 nm nanoplates, from [111]. (a) Adsorption strengthens as plate flattens against interface. (b) Schematic representing the small effect of contact angle upon covered area of interface. (c) Adsorption energy of platelets for a given contact angle θ, compared to that of a sphere.

direddy et al. and the Université du Maine group [84]. Cellulose nanocrystals (CNCs) with a rectangular parallelepiped structure, shown in Figure 4.16, with average dimensions 160 nm × 6 nm × 6 nm were added to a PEO/Dextran ATPS. The CNCs went to the interface of droplets, and due to their shape preferred in general to lie flat, causing stabilisation. Excess CNCs preferred the dextran phase, though neither polymer adsorbed on to them. Dextran-in-PEO emulsions were not stable long term, however PEO-in-Dextan emulsions were stable for months. This was ascribed in part to the formation of a network of CNCs within the dextran phase between droplets, shown in Figure 4.17, which acted as a very weak gel, delaying creaming of the droplets.

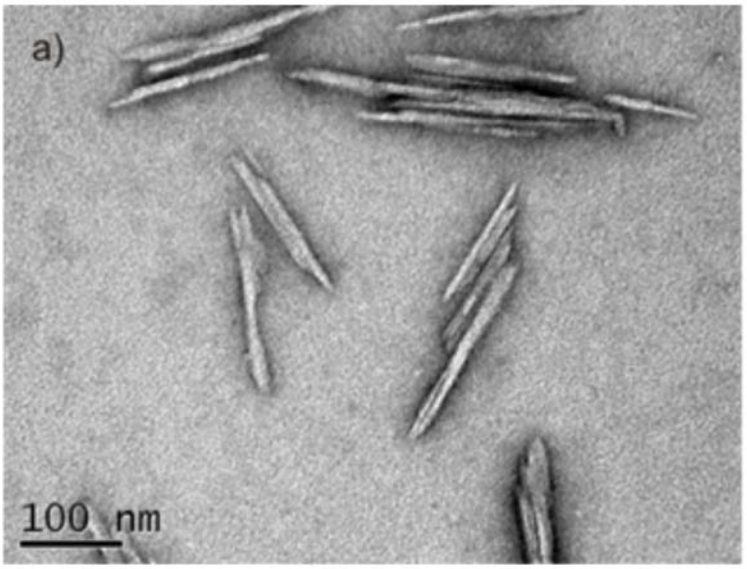

Figure 4.16: Transmission Electron Microscopy (TEM) image of cellulose nanocrystals, from [84]

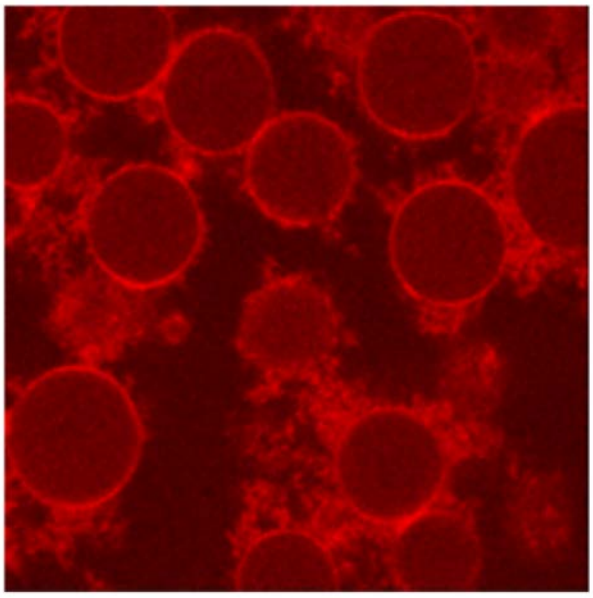

Figure 4.17: CLSM image (160 µm × 160 µm) of PEO droplets in a dextran matrix stabilised by fluorescently-labelled cellulose nanocrystals (CNCs) from [84]. CNCs go to the interface between the PEO droplet and the dextran phase, stabilising it. Additionally excess CNCs in the Dextran phase form a very weak gel, delaying creaming.

Objectives of this work

In the state of the art, we have seen that soft microgel particles are a promising system to produce emulsions that can be destabilised on demand. The crosslinking density and concentration influence the conformation of the particles at the interface and the bridging of emulsion droplets, and hence the mechanical stability of microgel-stabilised emulsions. But very little is known about the dynamics of the thin films, which can shed light on the origin of these effects. In studying the thin film drainage dynamics, the questions we address are:

- How does the drainage of a thin liquid foam film depend upon the microgel concentration and cross-linking density?
- Can the drainage dynamics be linked to previously obtained observations on the macroscopic behaviour of microgel emulsions, for instance their stability under shear, and the adhesion between droplets?

Additionally, we presented 'water-in-water' emulsions as promising systems for the creation of aqueous 'bioreactors', and for low fat food products. These systems are difficult to stabilise, but solid particles are demonstrably effective. In our work, we have focused on a model system for edible water-in -water emulsions, formed from fish gelatin and dextran - a system of interest at NIZO Food Research, with whom we collaborate. The questions we seek to answer with this work are as follows:

- Can spherical colloidal particles be used to stabilise the fish gelatin / dextran water-in-water emulsions?
- Do these particles spontaneously adsorb to the interface, and if so how fast is this process? Can it be described by a simple capillary force / viscous drag model?
- How does the trajectory compare to recent studies of particles at the oil/water interface, showing particles reach equilibrium only on very long timescales, due to pinning of the contact line? Can contact line pinning happen at the very low surface tension of a water/water system?
- Is the desorption energy of particles sufficiently high to make adsorption irreversible?

Part II

PNiPAM Microgels in Thin Liquid Films

Introduction

The subject of this part of the thesis is to examine and explain the behaviour of Poly-n-isopropylacrylamide (PNiPAM) microgels when used as soft Pickering emulsion stabilisers. As deformable colloids formed of loosely-crosslinked surface-active polymer, microgels behave very different from hard particles. But their effectiveness as stabilisers in oil/water systems has already been demonstrated by many authors [30, 78, 94]. Further, as a thermosensitive polymer, microgels formed from PNiPAM shrink and become more hydrophobic above a volume phase transition temperature (VPTT) of around 33 °C, providing microgel stabilised emulsions the added advantage of being destabilisable on demand upon a change in temperature.

However, despite the research interest in microgel-stabilised emulsions, little was known about the dynamics of such systems, specifically the drainage dynamics of the thin liquid films that form when emulsion droplets come into close proximity to each other, which influences many emulsion properties such as droplet adhesion and stability against coalescence.

The focus of this work was observing the drainage of microgel-stabilised thin films in air, as a model system for water-in-oil films. Firstly the influence of microgel concentration was examined. Additionally, in oil/water systems, it was shown that there are differences in stability between emulsions stabilised with microgels of different cross-linking density, 'softer' microgels having greater stability against mechanical disturbance than more strongly crosslinked microgels. This effect was examined with the model system using two different cross-linking densities of microgel.

In order to form the thin films, the Thin Film Pressure Balance was used, and to measure the drainage of the films, the thickness was observed dynamically using interferometry.

This part is an extract from the publication 'Drainage dynamics of thin-liquid films containing soft PNiPAM microgels: influence of the cross-linking density and concentration' by Keal et al., to be published in the journal Soft Matter [63]. This work was performed in collaboration with V. Schmitt[1], V. Ravaine[2] and V. Lapeyre[2].

[1]Université de Bordeaux, Centre de Recherche Paul Pascal, 115 Av. A. Schweitzer, 33600 Pessac, France

[2]Université de Bordeaux, Institut des Sciences Moléculaires, ENSCBP, 16 Av. Pey Berland, 33607, Pessac Cedex, France

Chapter 5

Materials and Methods

Contents

5.1 Materials: PNiPAM Microgels

The microgels were synthesized by aqueous free-radical precipitation polymerization of N-isopropylacrylamide and N,N'-methylenebisacrylamide by V. Lapeyre[1] V. Ravaine[1] and V. Schmitt[2], according to the procedure described in Ref [30]. Microgels were then characterized by dynamic light scattering. Two batches of microgels having different crosslinking densities were produced. The microgels with 1.5% mol BIS had a hydrodynamic diameter of 770 nm at 25 °C and 260 nm in the collapsed state. The microgels with 5% mol BIS had a hydrodynamic diameter of 660 nm at 25 °C and 280 nm in the collapsed state above the VPTT. To produce fluorescent microgels, acryloylfluorescein, (0.1% wt with respect to NIPAM) was introduced in the polymerization reaction.

5.2 Thin Film Pressure Balance

The experimental apparatus was adapted from the Thin Film pressure Balance apparatus as described by Mysels and Jones [77], modified to be more suitable for films with poor stability. Films were formed within a 2.0 mm diameter, 0.8 mm height hole, drilled into a porous glass plate, as shown in Figure 5.1. The plate is attached to a vertical 8 mm syringe with tubing, which acts as a reservoir. Small holes open the syringe to balance the air pressure inside with that upon the film. The syringe is mounted on a micrometre adjustable vertical plate such that its height, and

[1]Université de Bordeaux, Institut des Sciences Moléculaires, ENSCBP, 16 Av. Pey Berland, 33607, Pessac Cedex, France

[2]Université de Bordeaux, Centre de Recherche Paul Pascal, 115 Av. A. Schweitzer, 33600 Pessac, France

hence the hydrostatic pressure upon the film, can be precisely adjusted. The disk is encased in a humidified plastic chamber to prevent evaporation. The temperature of the room is controlled through air conditioning, and set at $(21.0 \pm 0.5)\,^{\circ}\mathrm{C}$.

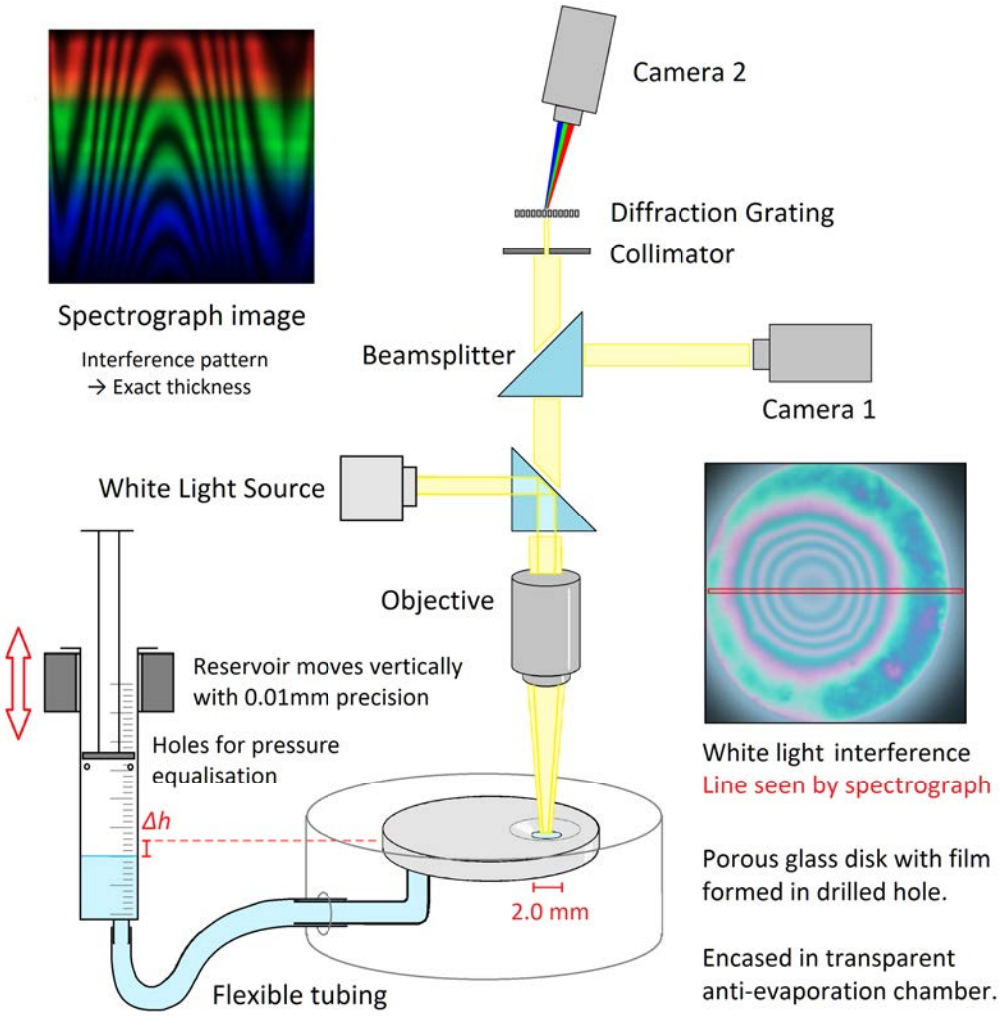

Figure 5.1: Experimental set-up used to study the drainage of thin-liquid films made from microgel suspensions.

The imposed pressure upon the film is given by $\Pi = \Delta\rho g h$, where $\Delta\rho$ is the density difference between the solution and air, g is gravitational acceleration and h is the vertical distance between the surface of the reservoir and the film. The diameter of the reservoir is much larger than the capillary length of the solution such that the curvature of its interface does not contribute significantly to the pressure. The volume of solution drained by application of pressure has a negligible effect upon the volume within the reservoir. In all experiments reported here the applied pressure Π was 15 Pa.

5.3 Interferometric Thickness Measurement

Above the film a reflected light microscope is mounted, with a white light lamp illuminating the film. Reflected light from the film is then split by a beam splitter into both a colour video camera

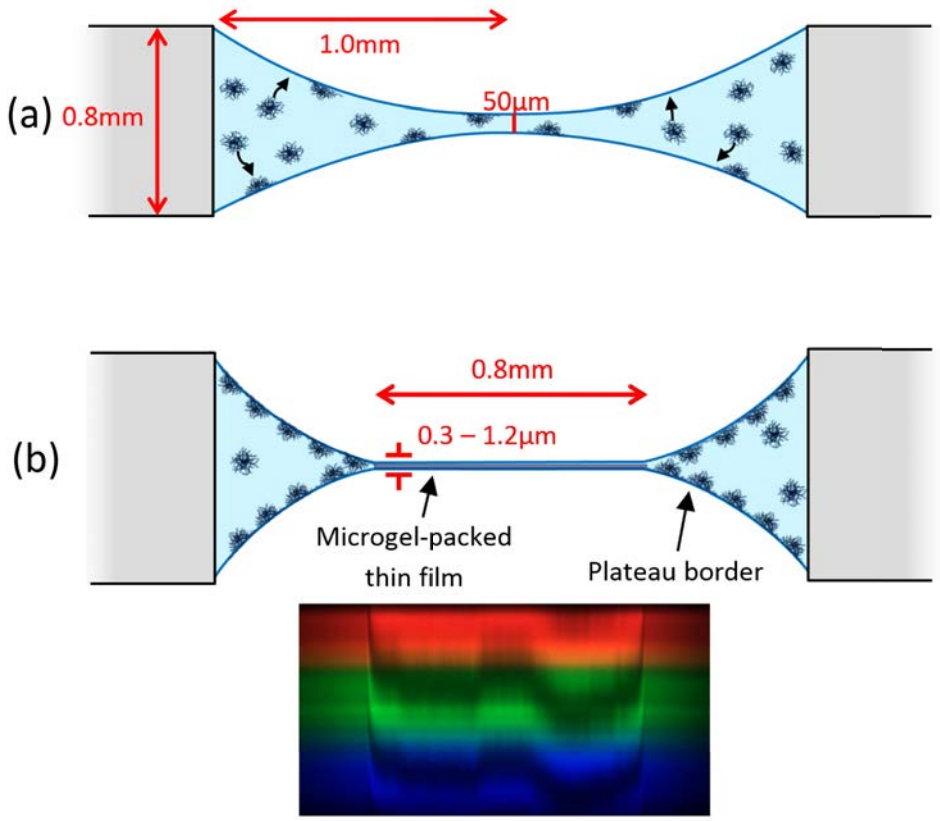

Figure 5.2: Schematic of microgel film formation and drainage. Microgels shown schematically; actual diameter 700 nm. (a) Time $t = 0$ s. Interfaces 50 µm apart at closest point and do not interact. Time allowed for microgels to diffuse and adsorb to the interface. (b) Shape of the film after hydrostatic pressure is applied and drainage begins. Interferometry spectrum for a typical film is also shown.

(Cyberlink PL-B776U), and a spectrograph (Specim V8E) connected to another video camera. The spectrograph provides the wavelength-dependent intensity for a line across the image. The wavelengths of the maxima and minima of interference occur at $\lambda = \frac{2nt}{(m-\frac{1}{2})}$ and $\lambda = \frac{2nt}{m}$ respectively, where n is the refractive index of the solution, t the thickness and $m = 1, 2, 3, ...$

The refractive index of the solution is calculated according to a linear combination by concentration of the wavelength-dependent refractive index of pure water [23] and pure PNiPAM [85]. As explained in the Appendix A, as the microgel particles have been shown to be incompressible [82] and their index of refraction is close to that of water, their deformation and change in concentration in the films during drainage has no significant contribution to the overall refractive index of the films, and hence on the thickness measurement. The thickness profile of the film is attained through finding maxima and minima of intensity.

The experimental procedure begins with the forming of a film in the hole with a drop from a pipette. The initial film is set at 50 µm thickness, where the surfaces are non-interacting (Figure 5.2a). The system is allowed a set adsorption time for microgels to diffuse and adsorb to the surface. Unless otherwise specified, the adsorption time for 1% wt was 20 minutes, and for 0.1% wt 40 minutes, chosen to allow sufficient diffusion time, based on Reference [87]. Then the hydrostatic pressure is applied in one step and the film begins to drain (Figure 5.2b). Once drainage is complete, the adhesion between the interfaces is tested. In order to do this the hydrostatic pressure is removed from the film, to re-swell the film.

5.3.1 Plateau Border Contact Angle Measurement

Measurement of the contact angle in the Plateau border begins with interferometric measurements of the thickness of the plateau border by the film edge with a 100x microscope objective (Olympus LM PlanFI 100x/0.80) and the spectrometer. A linear profile is fitted to these measurements and the angle this line makes with the horizontal plane equals $2\theta_{\text{ads}}$.

5.3.2 Dimple Volume Measurements

For films with a dimple symmetrically centred in the film, interferometric measurements give the film thickness profile of the central line. Modelling the dimple as two spherical caps resting on a cylindrical volume with the thickness of the surrounding film, the model profile is fitted to the measured profile, and the volume of the model system calculated. For films where the dimple is asymmetrically placed on the film but still within the line measured by the spectrometer, the distance of the centre of the dimple from the spectrometer line is measured in the video microscope image, and introduced as a parameter of the model.

5.3.3 Fluorescence Measurements

Film drainage experiments of microgels labelled with a small quantity of fluorescein were performed as described above for non-labelled microgels, however with a filter cube (Olympus U-MWIBA3) in the light path to select excitation and observation wavelengths at 460 nm to 495 nm and 510 nm to 550 nm respectively. The presence of fluorescein in the microgels had no observable effect upon their behaviour.

Chapter 6

Thin Liquid Film Measurements

Contents

6.1 Behaviour of 1.5% mol BIS (Soft) microgel films

We investigate the drainage dynamics of foam films made with 1.5% mol BIS microgels at two particle concentrations, 0.1 and 1% wt. For the 1% wt foam films drain in approximately 1500 s to reach a film of thickness 1070 nm (Figure 6.1). In the first stage, the films form a 'dimple', a spherical cap, which becomes thinner over time. Dimples are known to form because of the pressure gradient in the thin liquid foam film during drainage [59, 60] as the pressure is larger in the centre of the film than on the edge, as discussed in Section 2.3.2.

In the case of the 1.5% mol BIS microgels at a 0,1% wt, we find that shortly after applying the pressure a thin liquid foam film of uniform thickness 340 nm invades the film and traps a spherical dimple (Figure 6.2). This symmetric dimple drains into the 340 nm thin barrier ring in 1500 s. Symmetric drainage is usually observed when a high surface viscosity stabilises thin liquid films [59, 60]. After 2200 s seconds, the foam film thickness becomes homogeneous.

The large difference in thickness, 1070 nm versus 340 nm, obtained for high and low concentrations respectively could be caused by a possible bilayer to monolayer of microgels transition in the film in the case of the low concentration, i.e. a monolayer of microgels that bridge the interfaces. As bridging is known to induce adhesion between the interfaces, we probe in the following the adhesion between the interfaces by reducing the applied pressure back to zero.

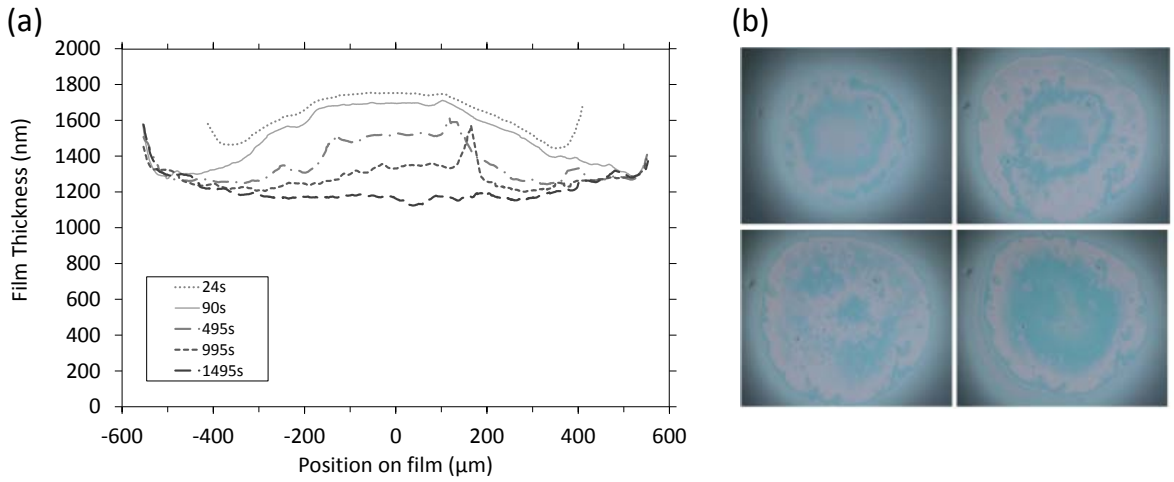

Figure 6.1: (a) Drainage dynamics and thickness profile of a foam film with 1.5% mol BIS microgels at 1% wt. (b) snapshot of a film containing the 1.5% mol BIS microgels at 1% wt during drainage using white light interferences for 24, 90, 500, 1500 seconds. Adsorption time is 20 minutes. Applied pressure is 15 Pa.

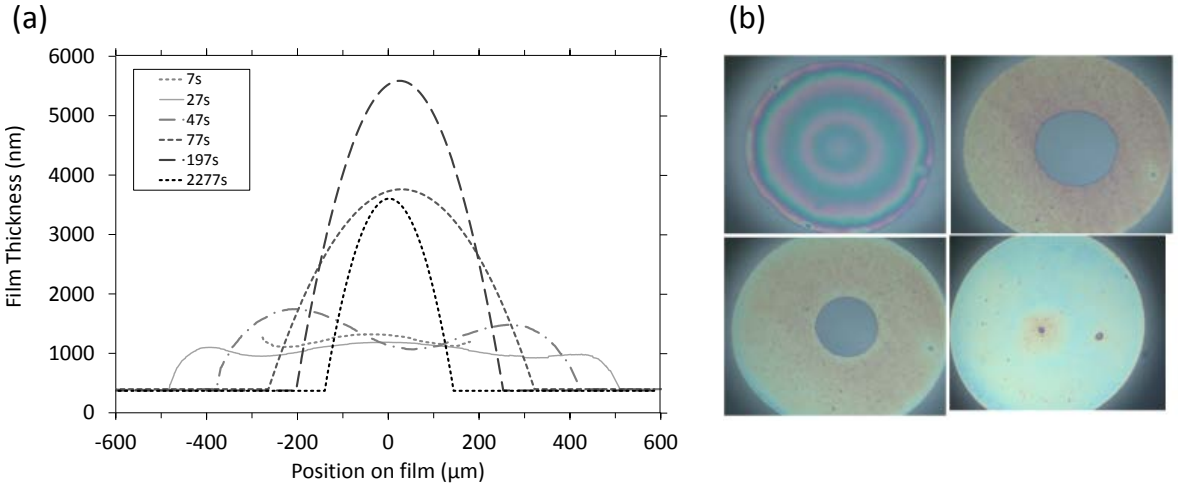

Figure 6.2: (a) Drainage dynamics and thickness profile for the 1.5% mol BIS microgels at 0.1% wt as a function of time . (b) White light images of the thin-liquid foam films as a function of time, for 18, 80, 500 and 3000 seconds. Applied pressure is 15 Pa.

6.1.1 Adhesion between interfaces

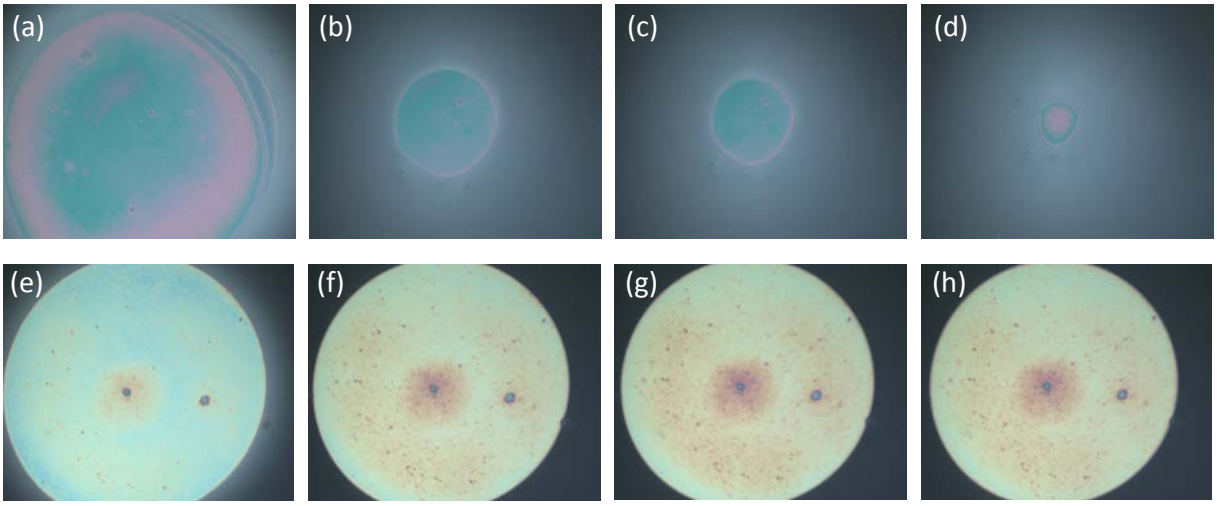

Figure 6.3: Image sequence of the thin foam films before and during the adhesion test. Images (a), (b), (c) and (d) show a 1% wt film of microgels with 1.5% mol BIS crosslinker. Image (a) is taken before reducing the applied pressure ($t = 0\,\mathrm{s}$), and (b), (c) and (d) show the re-swelling of the film once pressure is removed, at $t = 2$, 10 and 60 s respectively. Images (e), (f), (g) and (h) show a 0.1% wt film, 1.5% mol BIS at the same times as (a), (b), (c), (d). Immediately after the pressure is removed, the reflected light in the plateau border becomes much less intense, indicating a large increase in adhesion angle.

By reducing the hydrostatic pressure to zero, it is possible to re-swell the film with water from the Plateau borders. By measuring the adhesion angle, i.e. the angle between the film and the meniscus, we can probe the adhesion between the interfaces. Indeed,

$$E_{\mathrm{adh}} = -\int_{\infty}^{h_g} \Pi_{\mathrm{dis}}(h)\,\mathrm{d}h = 2\gamma_{\mathrm{aw}}\left(1 - \cos(\theta_{\mathrm{adh}})\right) \tag{6.1}$$

with Π_{dis} the disjoining pressure, h the thickness of the film, γ_{aw} the air water interfacial tension, θ_{adh} the contact angle in the meniscus.

As shown in Table 6.1 and Figures 6.3a, b, c, d, in the case of the 1% wt sample, we find that the meniscus recedes immediately and the adhesion angle, which is initially equal to 0.1° before the pressure reduction, remains constant after the pressure is reduced. We note that the contact angles that we measure are of the same order of magnitude as those commonly obtained for thin-liquid films standing in air [55]. For the 0.1% wt (Figure 6.3e, f, g, h), the initial contact angle θ_{adh} is 2° (Table 6.1).Shortly after decreasing the pressure, the meniscus remains pinned until the contact angle increases to 6° and then starts receding. From this adhesion angle, using Equation 6.1, taking $\gamma_{\mathrm{aw}} \sim 40\,\mathrm{mN/m}$ [20], we deduce that the energy of adhesion per unit surface is of the order of $0.5\,\mathrm{mJ\,m^{-1}}$.

From these measurements we conclude that a lower concentration promotes adhesion between the two interfaces of the film and that the microgels particles probably bridge the interfaces of the film in the case of the 0.1% wt. These results are consistent with Destribats's study [29] which reports partial bridging between emulsion droplets in the case of 1.5% mol BIS microgels. Their Cryo-SEM images show that micron-sized regions of various thicknesses coexist within the films corresponding

Table 6.1: Summary of steady-state thickness, adhesion angle θ_{adh} and adhesion energy, E_{adh} obtained for the samples studied.

	1.5% mol BIS		5% mol BIS	
	0.1% wt	1% wt	0.1% wt	1% wt
Thickness (nm)	340	1200	400	900
θ_{adh} (degrees)	6	0.1	8	0.1
E_{adh} mJ m^{-1}	0.5	~ 0	1	~ 0

to monolayers and bilayers. Although we measure a larger angle between the interfaces for the 0.1% wt we do not have enough spatial resolution to determine whether the film is composed of a uniform monolayer of particles or whether both configurations coexist.

6.2 Behaviour of 5% mol BIS (Hard) microgel films

6.2.1 Low concentration (0.1% wt)

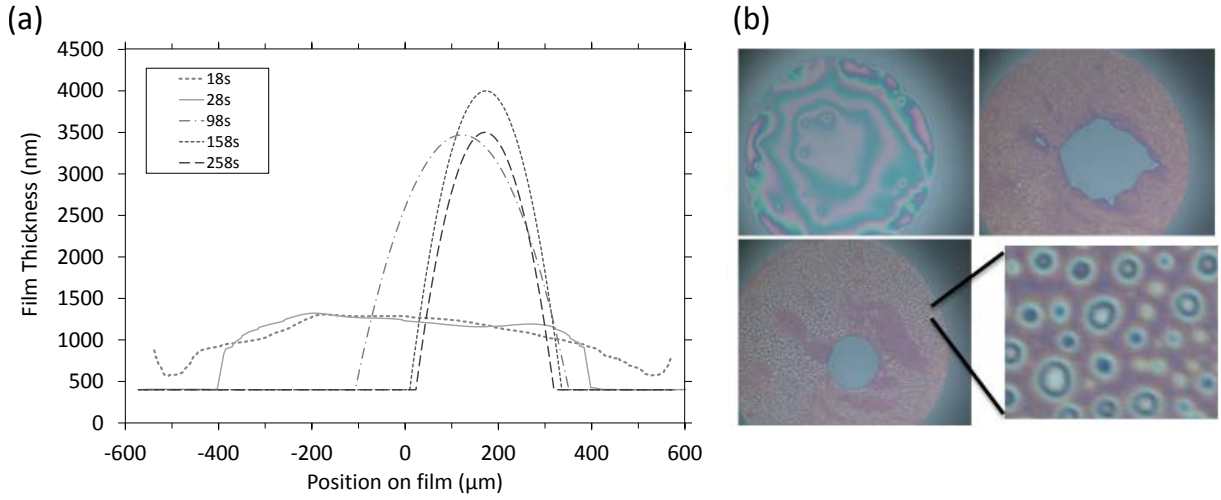

Figure 6.4: (a) Drainage dynamics and thickness profile for the 5% mol BIS microgels at concentration 0.1% wt. (b) White light images of the thin-liquid films as a function of time for 18, 100, 1300 seconds.

In the case of the 5% mol BIS microgels at 0.1% wt (Figure 6.4), the drainage dynamics at short time are very similar to those observed for the 1.5% mol BIS microgels at 0.1%wt. We observe a dimple which drains within a film of uniform thickness $\simeq 400\,\text{nm}$. The film is slightly thicker than the 1.5% mol BIS one, possibly because the more densely cross-linked microgels are more rigid and spread to a lesser extent at the interface. We also note that the shape of the dimple is less symmetric than for the soft microgels. This can be caused by lower surface viscosity [59, 60] due to less interpenetration of microgels.

For the more densely cross-linked microgels, the film thickness is much less homogeneous than the microgel with lower cross-linking density; immediately after nucleation of the 400 nm film, its thickness varying by tens of nm in regions a few µm across, visible as the white and red texturing in Figure 6.4. Over longer times however this inhomogeneity becomes much more pronounced through a process resembling spinodal decomposition [100, 101], where thinner (whiter) spots deepen and

occasionally coalesce on the film, eventually forming much larger thin circular zones, as demonstrated in Figure 6.5a. After several hundred seconds, the larger zones (20 µm diameter) can be as thin as 110 nm in their centres. The profile of a thin zone measured with a 100× objective is shown in Figure 6.5b. Once these thin zones appear in the film breakage is more likely.

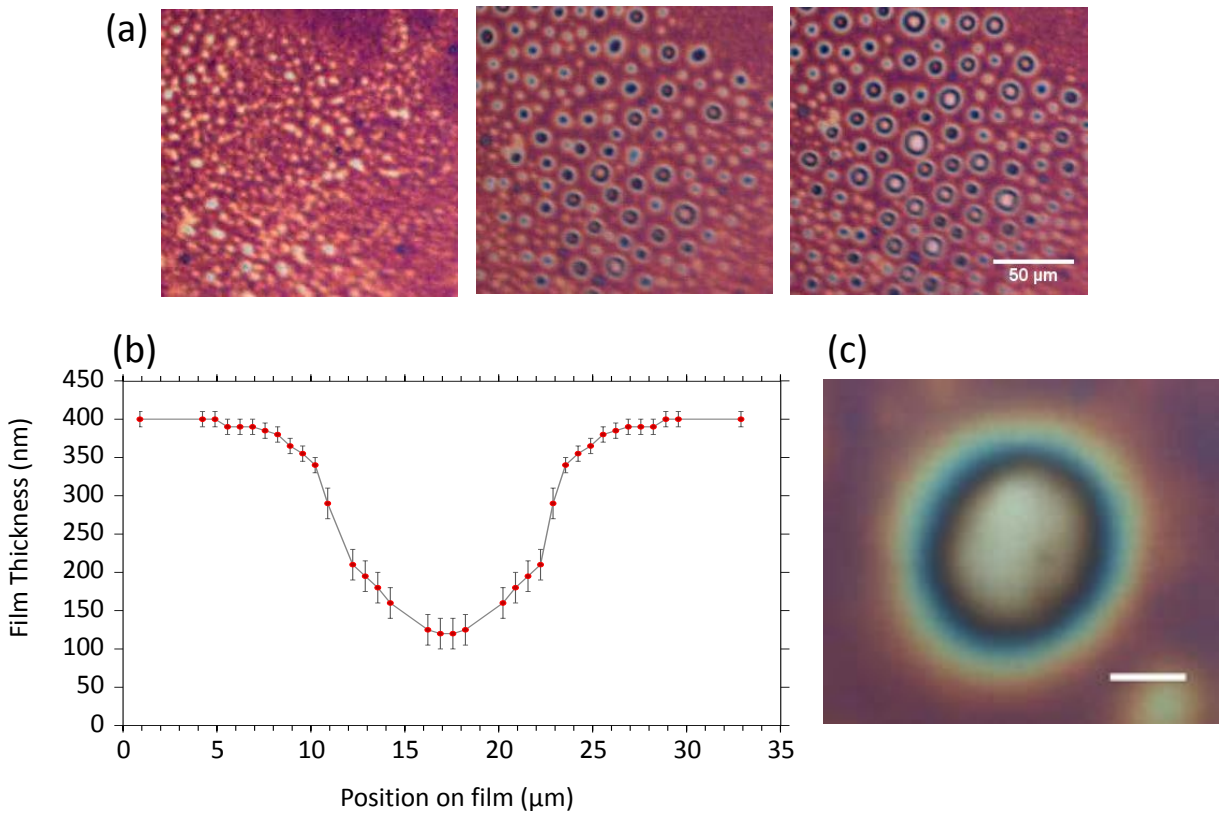

Figure 6.5: White light interference image of the film during the growth and deepening of the thin zones (5% mol BIS, 0.1% wt). (a): the thin zones grow and deepen over time. Frames show 160, 700, 2000 seconds. (b) and (c): profile and white light image obtained with a 100× objective. Scale bar 10 µm.

To determine whether microgel particles are present in these thinner zones, we performed fluorescence measurements using fluorescent microgels and a high-sensitivity camera. As shown in Figure 6.6 the fluorescent intensity is very low in the thin zones, whereas microgels can be individually resolved at their edges. There are therefore no microgels in the 110 nm regions. These depleted zones could lower the life time of the present foam film as the film is no more protected against rupture by microgels. Also, the transient stability of these zones can be explained by the fact that to empty these zones, the water has to drain slowly through the microgel compressed particle layer surrounding them.

Unlike the 1.5% mol BIS microgel foam films, under the same experimental conditions, the 5% mol BIS microgel foam film can exhibit two possible surface behaviours consistent with different surface concentrations. The lack of homogeneity of the film thickness probably reflects the lack of homogeneity of the packing density of the two single air-water interfaces, which are forced into contact to produce the thin foam film upon pressure application. Such gradients in packing density may appear during the adsorption time and probably remain stable because the Brownian motion of these microgel particles is very slow at interfaces [20] and they tend to form clusters at liquid

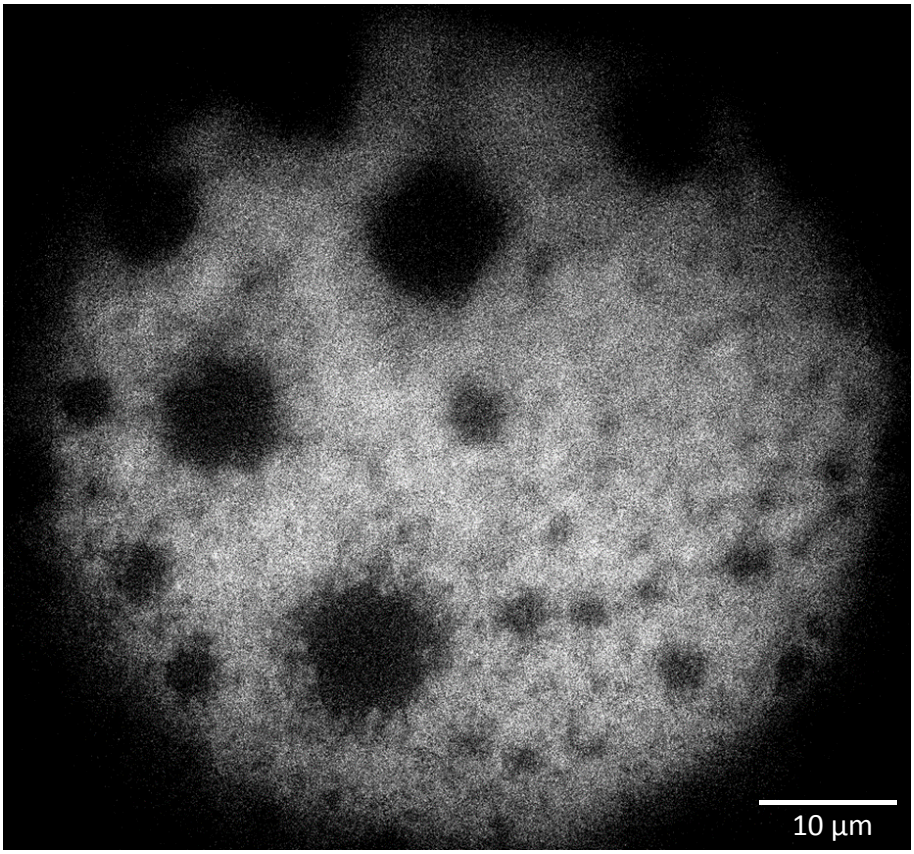

Figure 6.6: Fluorescence image of a thin film containing 5% mol BIS microgels at a concentration of 0.1% wt. Individual microgels can be resolved. Dark regions show that there are no microgels present within thinner regions of film.

interfaces [20, 53].

Adhesion experiments performed on the 0.1% wt films show that the angle, θ_{adh}, increases from 2.7 to 8° as the pressure is released illustrating the adhesion phenomenon between the interfaces.From the value of the angle we find an adhesion energy of $\sim 1\,\text{mJ}\,\text{m}^{-1}$, which is two times larger than the one measured for the 1.5% mol BIS microgels, showing that increasing the cross-linking density leads to an increase of the adhesion energy. This observation on a single foam film is again similar to the observation of Destribats et al. [29] on emulsions. We note that our adhesion energies are an order of magnitude lower the ones we can estimate from Destribats's contact angles measured between emulsions droplets. However, in their study they use much smaller particle concentrations and their emulsification process involves a high shear force which favours spread conformation and bridging.

6.2.2 High concentration (1.0% wt)

As the concentration is increased to 1% wt the short time behaviour is similar to what we observed for the 1.5% mol BIS microgels at 1% wt, i.e. a flat foam film of thickness 800 nm is obtained after 1400 seconds (Figure 6.7). On a longer time scale, in some cases, we observe 450 nm-thin zones nucleating in the foam film, however the 450 nm region never spreads all over the film (Figure 6.7b). When the pressure is released on such films, the 450 nm thin regions remain pinned in the foam film while the thicker parts swell quickly (Figure 6.7c). The 450 nm regions are therefore adhesive and correspond to particles bridging. This result confirms that the 5% mol BIS microgel favour bridging in thin liquid foam films.

6.3 Influence of cross-linking density on dimple drainage

Figure 6.8 presents the time evolution of the volume of the draining dimple trapped in the microgel adhesive thin liquid foam film for the 5% mol BIS and 1.5% mol BIS microgels at 0.1% wt. We find that the dimple drains faster for the 5% mol BIS microgels than for the 1.5% mol BIS. From the drainage dynamics we can estimate a global permeability of the microgel layer surrounding the dimple using Darcy's law, which describes the flow of liquids in porous media under a given pressure difference. Here we consider the flow of water from the dimple to the meniscus, through a flat film of uniform thickness, in a cylindrical geometry,

$$Q_{\text{porous}} = \frac{\kappa \pi h}{\mu} \frac{\Delta P}{\ln \frac{R_{\text{film}}}{R_{\text{dimple}}}} \tag{6.2}$$

where Q is the flow-rate in $\text{m}^3\,\text{s}^{-1}$, κ is the permeability in m, h is the thickness of the film (400 nm for the 5% mol BIS and 340 nm for 1.5% mol BIS), μ is the water viscosity, ΔP is the pressure difference between the dimple and the film due to the curvature of the dimple, R_{film} and R_{dimple} being the radii of the foam film and dimple respectively. We obtain the same permeability for both systems, of the order of $\kappa = 2.3 \times 10^{-14}$ m. From this permeability we deduce the characteristic length scale, $\lambda \sim \kappa^{\frac{1}{2}}$ which can be viewed as the typical width of the channels in which the water flows during the drainage. We find $\lambda \sim 500$ nm for both microgels. This length is consistent with the order of magnitude of the space between the particles in a close packing configuration and much larger than the mesh size of the polymer network the particles are made from. This shows that

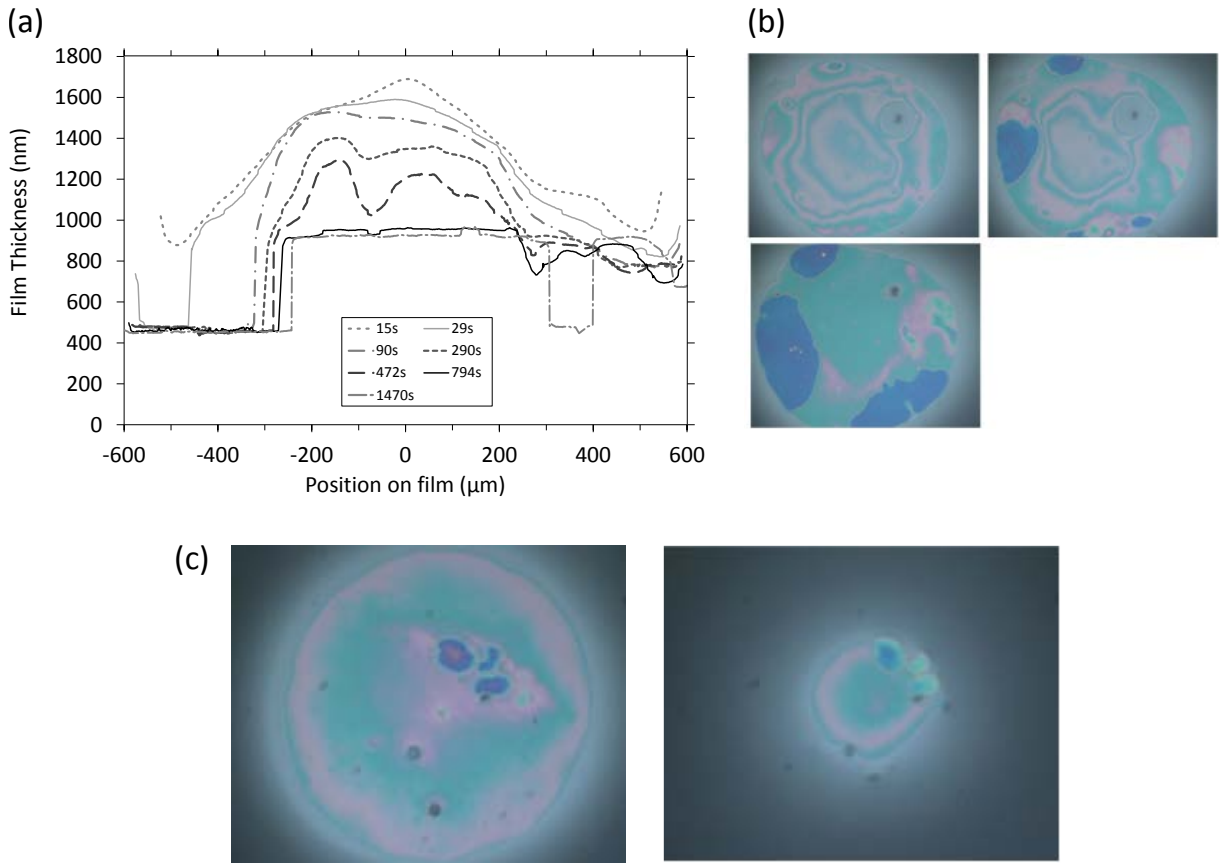

Figure 6.7: (a) Drainage profile for the 5% mol BIS. (b) Snapshot of thin-liquid foam films 5% mol BIS microgels 1%wt for 15, 90, 800 seconds. (c) Adhesion experiment for 1% wt., 5% mol BIS film. Upon pressure reduction, the blue zone remains pinned in the film while the thicker parts swell rapidly.

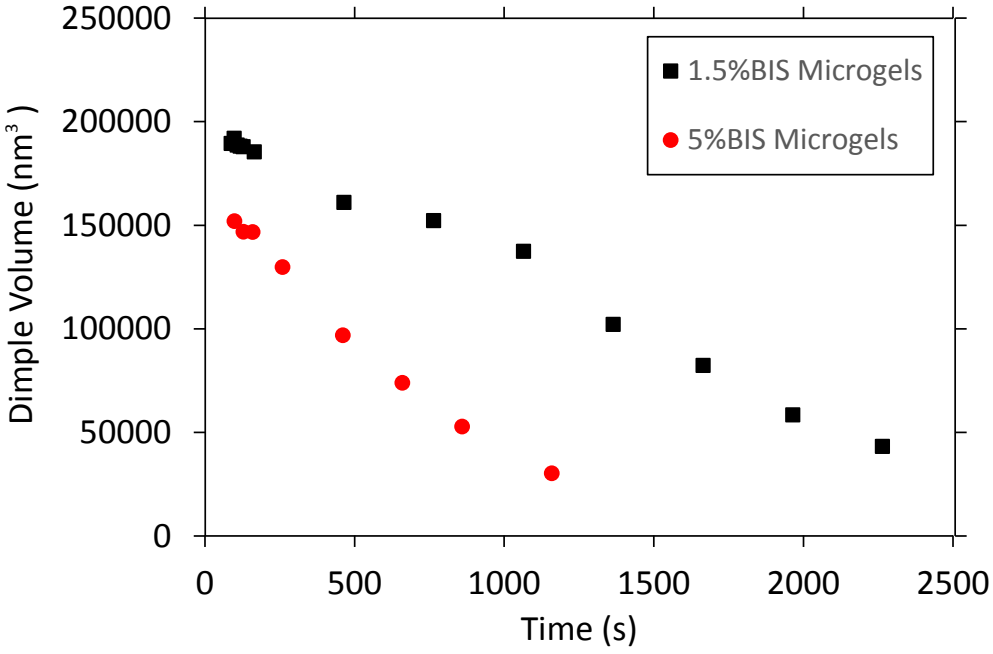

Figure 6.8: Volume of the dimple as a function of time for 1.5 and 5% mol BIS microgels.

the water rather flows around the particles than through them. From this calculation we deduce that the faster drainage observed for the 5% mol BIS particles is mostly due to the fact that the corresponding film thickness, h, is larger, leading to a larger flow rate.

6.4 Discussion

6.4.1 Summary of main results in context of previous studies on emulsions

Our main observations are as follows;

- The microgel concentration controls the adhesion between the thin liquid foam film interfaces. The lowest microgel concentration film shows bridging with a thickness of one monolayer. Conversely, we did not observe adhesion or bridging for the largest concentration. In the latter case, the films have the thickness of a bilayer.
- The more densely cross-linked microgels lead to larger adhesion angle (2.7 to 8° upon removal of applied pressure, versus 2 to 6° for the low cross linking density). The more densely cross-linked microgels drain more quickly, tend to present depleted zones that grow over time and lead to more unstable films. These results present striking similarities with previous observations made for water in oil thin films observed in situ in emulsions.
- Bridging is observed for emulsions prepared in the limited coalescence regime i.e. in a particle poor regime where the particles are in a spread conformation at interfaces. In those conditions, bridging is favoured for more cross-linked microgels.
- The stability of emulsions with respect to handling is lower for more cross-linked microgels because of a lower lateral interpenetration and more protruding microgels in the water phase as they are less deformable. Consistently in our study the foam films made with the more cross linked 5% mol BIS microgels at low concentration are thicker.
- For the largest concentrations, microgels spread to a lesser extent and are in a more compressed conformation. The connection between droplets is less probable and non adhesive bilayers are observed.

There is a fascinating similarity between the two types of interfaces and systems, i.e. air-water interfaces in a single thin liquid foam film and oil-water interfaces in emulsions, although the interfacial tensions involved are slightly different. Such resemblance between a model foam film and a collection of emulsion films is rare. This is even more surprising as the process used to produce these two types of interfaces is very different. A strong shear energy is used to produce emulsions unlike the foam films in the thin film pressure balance set-up. In fact the structure of the layers, such as the percentage of bridging particles in an adhesive film, may be different for both systems. We expect more particles bridging in the case of emulsions as a strong stirring energy favours spread conformations. However these two parameters, surface tension and stirring energy, do not seem to influence the variation in films' behaviour with respect to parameters such as cross-linking density and particle concentration.

6.4.2 Number and conformation of particles deduced from the film thicknesses

The goal of this section is to obtain a rough estimation of the adsorbed radii of the particles at air-water interfaces from the measured film thicknesses and to deduce what is the conformation regime, ie, spread or compressed, of the particles for the two concentrations investigated.

First, using a confocal microscope, we measured the number of particles per unit volume in the thick film c_{bulk} (see Appendix B) and deduce N_{total}, the total number of particles in the thick film for the 0.1 and 1% wt samples. A schematic to aid comprehension of these values is shown in Figure 6.9.

$$N_{\text{total}} = c_{\text{bulk}} \times V_{\text{thick-film}} \tag{6.3}$$

With $V_{\text{thick-film}}$ the volume of the thick-film (see Appendix A for an estimation of this). Then, we estimate the order of magnitude for the number of particles in the thin liquid foam film,$N_{\text{thin-film}}$, from the thickness of the film, assuming a perfect packing of the particles in the film (volume fraction equal to 1) and that the particles are incompressible [82] i.e. they keep a constant volume as they adsorb, as follows

$$N_{\text{thin-film}} \approx \frac{\pi R^2 h}{\frac{4}{3}\pi r_H^3} \tag{6.4}$$

With R the radius of the thin liquid foam film,r_H the hydrodynamic radius of the microgel particles in solution and h the thickness of the film. We note that microgel incompressibility was demonstrated in bulk solutions [82], however, at interfaces, PNiPAM dangling arms may concentrate at the interface due to their high surface activity. Moreover, this calculation does not take into account possible interpenetration between dangling arms, which are not cross-linked.

We then consider that the number of microgels in the thin liquid foam film, $N_{\text{thin-film}}$ is equal to the number, N_{ads}, of particles initially adsorbed at the two interfaces of the film of radius R before applying the pressure. We therefore assume that excess of particles in the thick-film are ejected into the Plateau borders during the drainage. Now considering surface area constraints for the film, we write:

$$N_{\text{thin-film}} = N_{\text{ads}} \approx 0.9\frac{2\pi R^2}{\pi r_{\text{ads}}^2} \tag{6.5}$$

where r_{ads} is radius of the microgels adsorbed at the interface before applying the pressure. We assume here that the surface fraction is 0.9 at the interface corresponding to a 2D hexagonal close packing configuration as often evidenced by imaging. From Equation 6.5 we deduce the expression for r_{ads} given in Equation 6.6:

$$r_{\text{ads}} \approx \sqrt{\frac{8 \times 0.9 \times r_H^3}{3h}} \tag{6.6}$$

The values of N_{ads}, N_{total} and r_{ads} are summarized in Table 6.2.

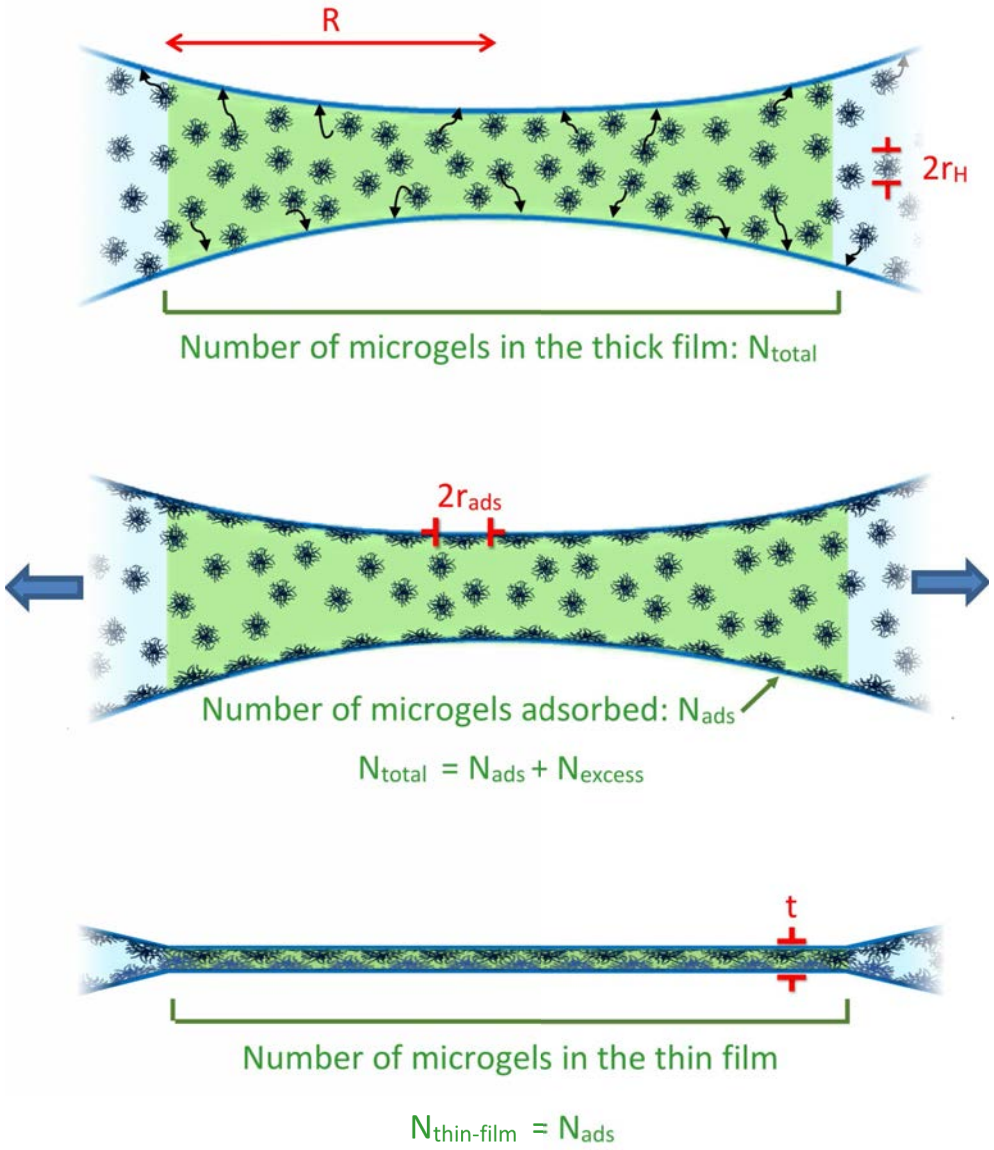

Figure 6.9: Schematic drawing explaining the estimation for N_{total}, $N_{\text{thin-film}}$, N_{excess}, N_{ads}. Top: film during adsorption time. Middle: Film just before pressure application and drainage. Bottom: Thin film post-drainage.

Table 6.2: Values of N_{total}, $N_{\text{thin-film}}$ and r_{ads} obtained from film thicknesses for varying cross-linking density and concentrations.

	1.5% mol BIS		5% mol BIS	
	0.1% wt	1% wt	0.1% wt	1% wt
N_{total}	2×10^7	2×10^8	2×10^7	2×10^8
$N_{\text{ads}} = N_{\text{thin-film}}$	1×10^6	4×10^6	2×10^6	5×10^6
r_{ads}	635 nm	337 nm	453 nm	302 nm
r_{ads}/r_H	1.64	0.87	1.39	0.93

For the 0.1% wt sample, r_{ads} is larger than the hydrodynamic radius of the particles meaning that the particles are in a spread conformation. At this low concentration, the 1.5% mol BIS microgels spread to a larger extent than the 5% mol BIS microgels, because of their smaller network elastic modulus, ultimately leading to thinner films (400 versus 340 nm) as the pressure is applied.

For the 1% wt sample, for both cross-linking densities, r_{ads} is lower than the hydrodynamic radius of the particles, corresponding to the so-called 'compressed' state in Reference [87], where the particles deform and stretch perpendicularly to the interface. These spreading states are illustrated in Figure 6.10.

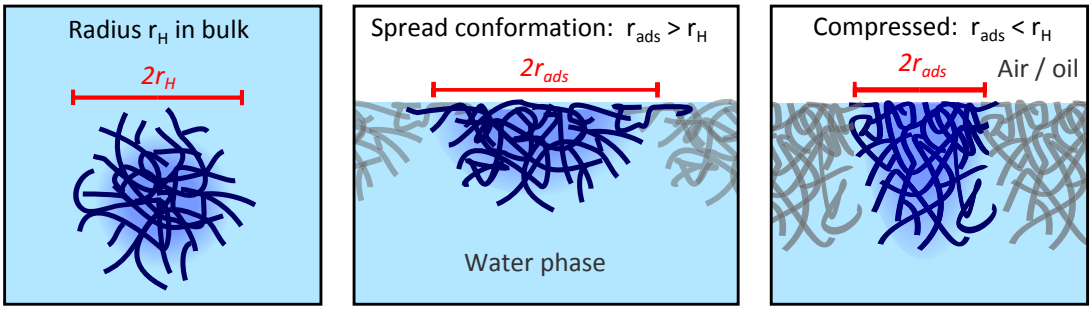

Figure 6.10: Schematic illustrating the conformation states of microgels adsorbing to an air/water or oil/water interface. While in bulk, the hydrodynamic radius of a particle is r_H. At low surface concentration, microgels spread at the interface, adopting a radius $r_{ads} > r_H$, and forming a thinner layer. For high microgel surface concentration $r_{ads} < r_H$, the microgels can compress in the plane of the interface, extending perpendicular to the interface.

As shown in Table 6.2, we find that the numbers of particles available in the thick films for the 0.1 and 1% wt samples are respectively one and two orders of magnitude larger than N_{ads} and $N_{\text{thin-film}}$. This means that in all cases, there is a large number of particles in excess in the films, which are ejected in the Plateau borders during drainage. Therefore the large difference in surface coverage for the 0.1 % wt and 1% wt samples cannot be accounted for by a large difference in the number of particles available.

We therefore learn from this simple calculation that the large difference in surface coverage for both concentrations cannot be due to the difference in the number of available particles in the thick film.

As stated in Geisel et al. [44] the conformation of the particles at the interface results from a balance between adsorption dynamics and spreading/compression dynamics of the particles. In the 0.1% wt case, adsorption is slower than in the 1% wt case. Therefore particles have more time

to spread at short times. Later, for new particles to adsorb, previously adsorbed particles have to compress to make space for incoming particles, which is unfavourable because of the elasticity of the particles. For the 1% wt case, the adsorption dynamics are much faster, more particles reach the interface at the same time, therefore particles may not have time to spread on the interface before coming into contact with each other. Because of the driving force for particle spreading, i.e. the increase of the contact of PNiPAM segments with the interface, the particles may spread into each other at longer times, causing a stronger interpenetration of the particles dangling arms. Therefore the adsorption kinetics may influence the degree of interpenetration of the particles.

6.4.3 Correlation between thin liquid foam film dynamics and surface elasticity

The surface shear and dilational properties are known to play a role in thin liquid foam film drainage [59, 60]. We discuss here the link between our results and previous studies concerning surface elasticity as a function of cross-linking density. From Langmuir trough experiments, Geisel [45] and Pinaud [87], have shown that the network elasticity of the microgel particles lowers the surface compressibility only at large compressions. Indeed at low compressions, the surface pressure of 1.5 and 5% mol BIS microgels overlap. Consistent with this, the dilational moduli obtained at low deformation do not depend on the cross-liking density. However at large surface compressions, the surface pressure of the 5% mol BIS layer becomes larger than that of the 1.5% mol BIS system. Thus the network elasticity plays a role in the compressibility only at large deformations, when the cores are exposed to pressure.

In our case, as we apply the pressure to force the two air-water interfaces to produce the thin-film, the network elasticity of the particles probably plays a role as more rigid particles prefer to rearrange to form a monolayer than compressing. Softer particles can compress more easily into a squeezed bilayer. This means that unlike in the low compression Langmuir trough experiments, elasticity does lead to different behaviour in bridging phenomena. However performing large compressions in Langmuir trough experiments is an indirect way of predicting the behaviour of deformable particles under large deformation, which is involved in bridging phenomena.

Let us now briefly highlight the fact that the largest cross-linking density microgels present a less symmetric dimple than the less cross-linked particles. Asymmetric dimples are known to be linked to a lower surface shear elasticity. Here the lower interpenetration between the dangling arms for the 5% mol BIS microgels probably favours a low shear viscosity. Owing to the low interpenetration and low spreading, the microgels are mobile enough to rearrange and provide space for particles to bridge.

To summarize, combining low shear viscosity and large compression elasticity at large deformation is correlated to easier bridging. In addition, the ability of the 5% mol BIS microgels to rearrange in the films probably enables the depletion phenomenon observed for the 0.1% wt samples, which leads to very unstable films.

Conclusion

We have investigated the drainage dynamics of thin-liquid films containing PNiPAM microgels suspensions with two cross-linking densities (1.5 % or 5% mol BIS) and at two concentrations (0.1 and 1% wt). At 1% wt, the films drain slowly, are not adhesive and have the thickness of a bilayer while at 0.1% wt, the films have the thickness of a monolayer, are adhesive and show bridging. From the thin liquid foam film thicknesses we provide a rough estimation of the radii of adsorbed particles in the thick-films before applying the pressure. Our results are consistent with particles being adsorbed in a spread conformation for the 0.1% wt sample and in a compressed conformation for the 1% wt sample. In line with previous studies on emulsions, we conclude that a larger surface coverage helps stabilizing non adhesive bilayers, while a lower surface coverage favours bridging and adhesive films. For low concentrations, a dimple is trapped in the thin films and slowly drains through the bridged film. From its drainage dynamics we deduce the permeability of the bridged layer and find that it is consistent with water flowing around the particles during drainage rather than through the polymer network of the particles.

We find that the cross-linking density has a strong influence on the film dynamics. Films made with the 5% mol BIS microgels drain faster, show bridging as well as a larger adhesion energy. Particle bridging in thin liquid foam films can be compared to previously observed bridging in emulsions, which lead to emulsions unstable against shear. This effect of bridging on Pickering emulsion stability not only holds for microgels-stabilized emulsions but is a more general phenomenon also observed for hard colloidal particles [39]. However, in the case of Pickering emulsions stabilized by microgels, this effect cannot be distinguished from another contribution arising from the particle deformability. Indeed, under shear, new contacts between drops are formed and involve microgels originally located at free interfaces. The ability of these microgels to flatten and to interpenetrate has been proposed to provide sufficient elasticity to prevent coalescence. Thus, microgels with the highest cross-linking density are less prone to such interpenetration while promoting bridging. The ability of the 5% mol BIS microgels to bridge thin foam or emulsion films to a larger extent than the 1.5% mol BIS probably explains why emulsions prepared with 5% mol BIS microgels are unstable to mechanical disturbance [29].

Moreover for the 5% mol BIS microgels at 0.1% wt, depleted zones appear in the films, while this phenomenon does not occur for the 1.5% mol BIS microgels. These depleted zones are more likely to lead to the rupture of the thin liquid foam films at rest as they are not protected against coalescence. This phenomenon is probably favoured by a low interpenetration between the particles and a low surface coverage.

Part III

Particles at Water/Water Interfaces

Introduction

The subject of this part of the thesis is the Aqueous Two-Phase System (ATPS), and the role colloidal particles can play within it. The experiments presented here focus first on whether spherical colloidal particles can stabilise an ATPS formed of non-mixing polymer solutions of dextran and fish gelatin, and more generally how such particles behave within the system. The ultimate goals of this part of the project are the stabilisation of water-in-water emulsions or droplets, for potential applications in food technology, encapsulation or creating bioreactors [32], and to gain understanding of particle adsorption dynamics in low surface tension systems.

The first stage of experimental work examined whether the addition of colloidal particles, namely Latex and Silica microspheres of sizes 0.4 µm to 3 µm could go to the interface of water-in-water systems, and stabilise emulsions using the pickering mechanism. The particle size, polymer pH, temperature of storage and emulsification method were all modified to search for stabilising effects, which would be observed with macroscopic techniques (video timelapse of emulsion ageing) and microscopic examination of emulsion droplets. To understand the polymers' interaction with the particles, further characterisation techniques were used such as zeta potential measurements in order to measure polymer adsorption to the particles.

The second focus is a detailed study of the dynamics of the particles' adsorption to the interface between the polymer phases. Recent advances in the study of colloidal adsorption show that adsorption dynamics for the oil/water interface are surprisingly slow, due to the pinning of the three-phase interface contact line on nanoscale features on particle surfaces [16, 21, 62]. These slow dynamics may negatively affect the emulsification of Pickering emulsions, and contribute to unexpected behaviour in systems where the equilibrium contact angle is assumed.

This work was done in collaboration with Hans Tromp[1] at NIZO Food Research in The Netherlands.

[1]NIZO food research, Kernhemseweg 2, 6718 ZB Ede, The Netherlands

Chapter 7

Materials and Methods

Contents

7.1 Materials

7.1.1 Polymer System

Among the many demixing polymer solution pairs introduced in Section 4.1, Fish Gelatin and Dextran is one of the most useful as a model system, due to its Newtonian shear behaviour and optical clarity.

7.1.1.1 Dextran

The Dextran used in the experiments here presented is Dextran (from Leuconostoc bacteria), A.M.W. 150,000, used as purchased from Sigma Aldrich in powder form. A 25 wt% stock was formed through adding the powder to Milli-Q de-ionised water undergoing magnetic stirring. Wetting was encouraged through shaking.

7.1.1.2 Fish Gelatin

Fish gelatin (A.M.W $\sim 100,000$) from Norland Products (kindly provided by Fibfoods, Harderwijk, The Netherlands) in the form of small flakes. A 25 wt% stock was formed in the same way as for Dextran above, except the stock was heated. Fish gelatin is non-gelling at room temperature, having a T_g of around 10 °C. However, to make it dissolve effectively, it must be heated to around 60 °C.

Antimicrobial Protection
For stocks that were used in preparing emulsions, 1 drop of 1M Sodium Azide was added to each 40ml stock to prevent bacterial growth. Other studies (for example [112,113]) assert Sodium Azide has no influence on the polymer system. However, for stocks that were used for particle adsorption studies Sodium Azide was omitted as a precaution.

pH Adjustment
As a polyelectrolyte, fish gelatin acts as a pH buffer, and so dominates the pH of the combined sample. The stock pH of Fish Gelatin at 20% concentration is measured to be 5.8. To raise the pH of the sample therefore, the pH of the fish gelatin component is carefully adjusted through addition of 1M NaOH. The pH was measured with a pH meter (Metrohm 632 pH Meter).

Salt Adjustment
The ions contributed by the polyelectrolyte act as an effective salt contribution. The conductivity of a stock fish gelatin solution was measured using a conductivity probe (WTW LF-340). The measured conductivity was converted to an effective NaCl concentration using look-up tables [38]. A 20% stock of fish gelatin has an effective salt concentration of 40mM. Dextran has no measurable effect upon conductivity. The measured conductivity of a 10% / 10% fish gelatin / dextran mixture confirms the linear mixing of these conductivities, with an effective salt concentration of 20mM.

The salt concentration was raised through addition of measured amounts of 1 mM NaCl to the de-ionised water of a stock solution before addition of the fish gelatin and dextran powders.

Table 7.1: Colloidal particles articles used in this study.

Size	Material	Surface	Fluorescence	Ordered From	Part Code
0.2 µm	Latex	Carboxylate	Fluorescein	Invitrogen	F8811
0.5 µm	Latex	Sulphate	None	Life Technologies	S37494
1 µm	Latex	Sulphate	Fluorescein	Life Technologies	F8852
1 µm	Latex	Carboxylate	Fluorescein	Life Technologies	F8823
1 µm	Latex	Amine	Red fluorescent dye	Sigma Aldritch	L2778-1ML
4 µm	Latex	Sulphate	Fluorescein	Life Technologies	F8859
10 µm	Latex	Sulphate	Fluorescein	Life Technologies	S37230
0.4 µm	Silica	Untreated	None	Micromod	43-00-402
1.5 µm	Silica	Carboxylate	None	Micromod	43-02-153
1.5 µm	Silica	NH_2	None	Micromod	43-01-153
3 µm	Silica	Carboxylate	None	Micromod	43-02-303
10 µm	Silica	Carboxylate	None	Micromod	43-02-104

Addition of Rhodamine B

In order to view the interface of the fish gelatin / dextran system with fluorescence microscopy, Rhodamine B was added to the fish gelatin phase. Due to its hydrophobicity, Rhodamine B strongly prefers the fish gelatin phase. 1 drop of 1M Rhodamine B was added to 40ml of fish gelatin 25% stock. This had no measurable effect upon observed behaviours.

7.1.2 Particles

The particles used were all spherical colloidal particles, composed of either polystyrene latex or silica. Multiple surface chemistries and sizes were examined for each material.

Table 7.1 lists the particles used in this study, which were used as supplied.

The particles of most interest to the adsorption tracking studies (Chapter 10), namely 1 µm, 4 µm and (average) 10 µm Sulphate latex particles were imaged with Scanning Electron Microscopy, as described in Section 7.3.8. The images can be seen in Figure 7.1. The 10 µm particles show considerable polydispersity, though all imaged particles are nicely spherical.

7.2 Sample Preparation

7.2.1 Emulsion preparation

All particles examined in this study go preferentially to the gelatin phase as shown later, so the best efficiency (ie. highest number of particles at interface) is achieved if particles are dispersed in the dextran phase before mixing. Hence, particles are added during the dilution of the dextran stock to the desired concentration, and dispersed through stirring or shaking. After this, gelatin is added.

The interfacial tension of an oil/water emulsion is high such that a high-shear emulsifier is needed to create small droplets, such as an Ultra-Turrax. A water/water emulsion however has a sufficiently low surface tension, of order $1-100\,\mu N/m$, that shaking alone for tens of seconds is enough to produce a dispersion of micron-scale droplets. Hence, emulsion samples are shaken by hand for 5 minutes. Immediately after emulsification, samples are placed in front of the camera and recording begins.

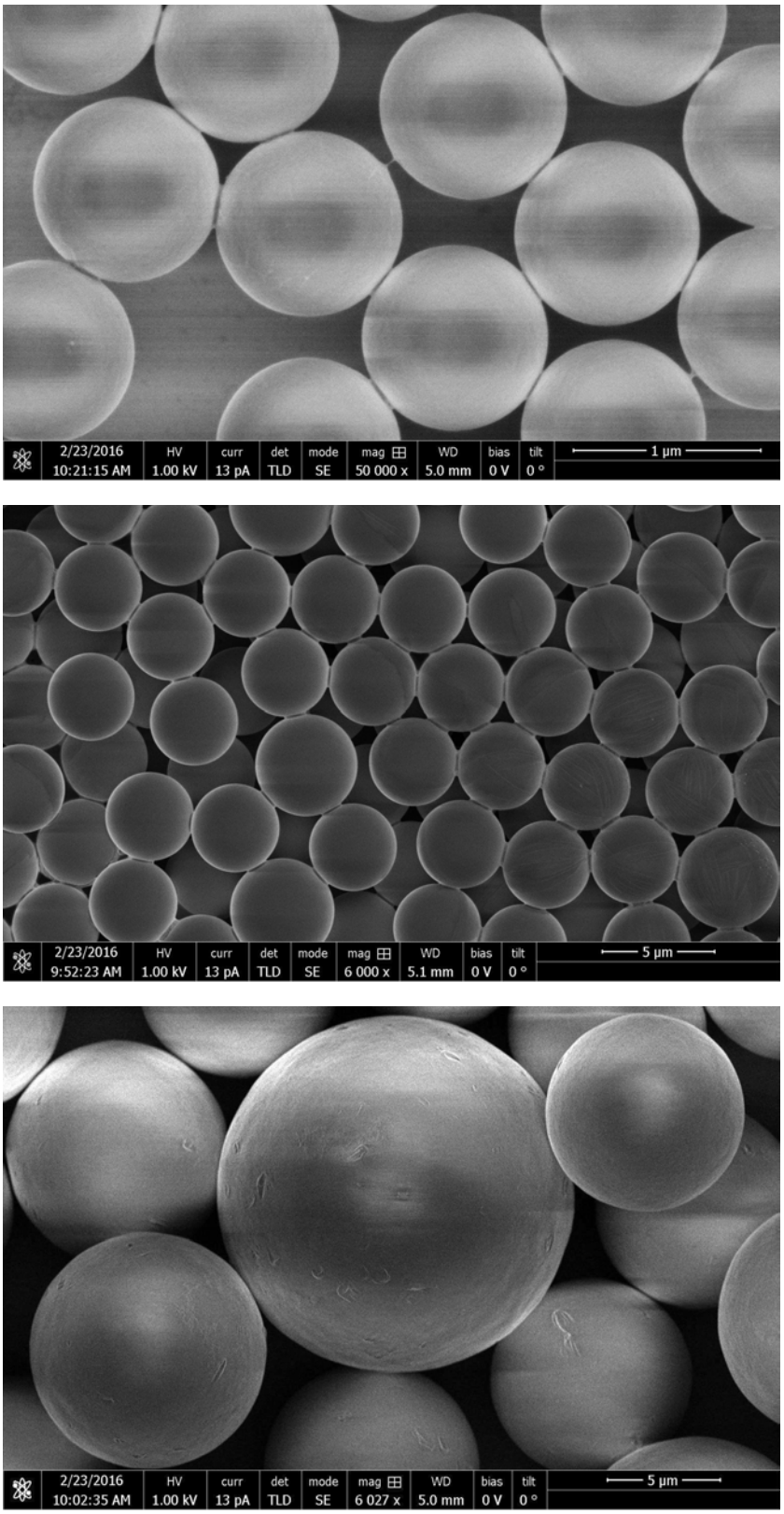

Figure 7.1: Scanning electron microscopy images of particle surface for 1 µm, 4 µm and (average) 10 µm Sulphate latex particles from top to bottom respectively.

7.2.2 Isolation of phase-separated phases

For some experiments, it is desirable to isolate each phase of a phase-separated system that has been mixed, and allowed to spontaneously phase-separate. The resulting isolated phases are then in thermodynamic equilibrium once brought back into contact. However, this is not trivial at the high polymer concentrations used in this study, as droplets of opposing phase can remain without creaming or sedimenting for many days to weeks due to the high viscosity and low density difference.

To accelerate the process, centrifugation was used. Emulsions were prepared through mixing equal parts of fish gelatin and dextran stocks, and the samples were shaken for 5 minutes to induce emulsification. Centrifugation at a force of $4,500g$ (where g is the gravitational acceleration) for a period of 30 hours was necessary to entirely remove droplets from the dextran phase, though small droplets remained in the fish gelatin phase after this period. To isolate the top phase, a syringe was brought into contact with the upper phase / air interface and the majority of the phase was withdrawn. Care was taken to avoid mixing with the lower phase despite the low surface tension. To isolate the lower phase, a puncture was made with a needle in the bottom of the centrifugation tube, and the lower phase was allowed to slowly drain.

7.2.3 Meeting Drop Sample

When studying the adsorption of particles at water-water interfaces, it is often difficult to observe particles in-situ in an emulsion. Hence, the use of a 'model' interface can often be preferable. Figure 7.2 shows a simple experimental setup to create a model interface in which droplets of each polymer solution meet and form an interface inside a glass chamber.

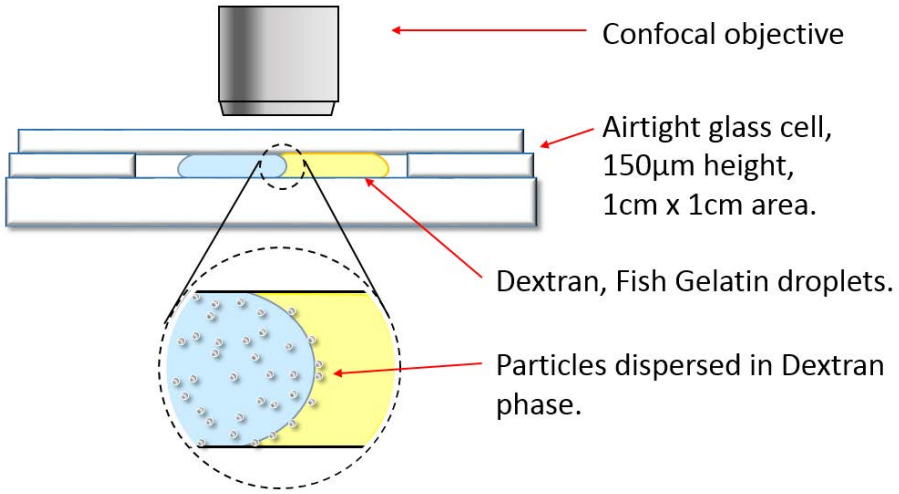

Figure 7.2: Schematic of meeting drop sample chamber, formed of glass microscope slides hermetically sealed with grease.

To make the sample, droplets of each polymer are initially placed in the uncovered chamber with around 1mm separating them. The droplets come into contact only when the cover is placed over the top, applying an even compression to the droplet and preserving a vertically symmetrical shape as the droplets wet both upper and lower slides. Once the interface is formed, it rapidly takes on a curvature due to the polymers' different preference for the microscope slide.

The droplets of polymer are of a fixed and equal volume to conserve the overall polymer concentration ratio. A highly viscous polymer solution is most suitable for this technique, as its shape and flow behaviour are more predictable and gravity plays a smaller role in the droplet shape.

7.3 Experimental Techniques

7.3.1 Timelapse of emulsion separation

A standard semi-quantitative technique for observing the macroscopic phase separation of emulsions is through timelapse video. This is a very simple and cheap technique that gives a clear indication of the stability or instability of emulsions. It is an obvious choice for screening the stabilising effect of different particles and conditions. Additionally, if particles are visible in a system (for example through opacity or fluorescence) it can be used to track the movement of particles through a system.

7.3.1.1 Measuring emulsion stability

For optically clear polymer solutions without particles, the turbidity of the sample indicates the presence of droplets scattering light. If the turbidity is preserved over time, the emulsion is at least meta-stable. If the phases are not density-matched, coalescence of droplets results in growing macroscopic phases which can be clearly visible. At longer times, the sharpness of the interface between these phases indicates whether a stable or meta-stable region is present (ie. a broadened interface indicates a region of stability). And finally the curvature of the interface provides insight into the balance between density and surface tension within the sample, which can indicate the influence of particles at the interface, though this is not analysed in this study.

The experimental setup shown in Figure 7.3(a) consists of a video camera focussed on samples in transparent vessels, illuminated by a consistent light source. Emulsion samples, prepared as described in Section 7.2.1 were placed in square 4ml plastic cuvettes allow side-by-side comparison of multiple samples of different formulations, including a control. Photographs are taken every 10s to 1 minute, for many hours.

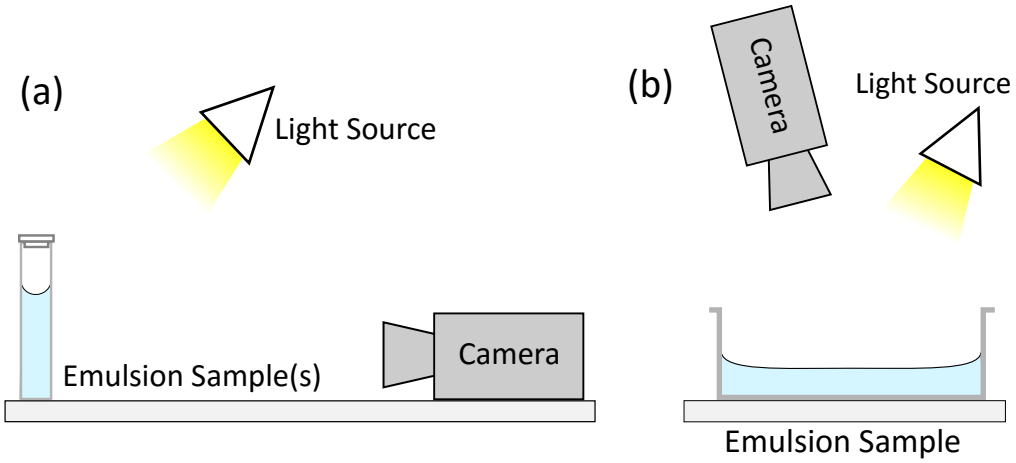

Figure 7.3: Experimental setup for recording timelapses of (a) emulsion separation and (b) movement of particles through a sample.

7.3.1.2 Comparing Stirring and Shaking

An important consideration in emulsification is that applied shear is required to bring particles to the interface. However, in this low surface tension system, that shear could be sufficient to push particles entirely through the interface.

A simple experiment was designed to test whether the shear of hand shaking was enough to remove particles from the dextran phase to the fish gelatin phase, through comparing gentle stirring with shaking as emulsification method. The setup is shown in Figure 7.3(b). A 10cm-diameter bath was filled with 10ml of 20% dextran solution dispersed with 0.05wt% 500nm Sulphate latex particles. 10ml of 20% fish gelatin solution was added dropwise from just above the surface to minimise uncontrolled mixing. In an optically clear sample, at sufficient concentration particles are clearly visible as white opacity. If particles are present in only one phase of a phase-separated system, their location will be obvious. Hence, by observing the change in opacity of the phases, particle location in the sample can be known.

Once prepared, stirring was performed at a slow consistent speed with a 3mm diameter glass rod for 2 minutes, until the sample was visibly fully mixed (ie. opacity was constant throughout). For shaking, the sample was sealed and shaken for 2 minutes. The camera then observed the phase separation of the sample over several hours.

7.3.2 Bulk Rheology

The viscous response to shear of each polymer solution was measured using a bulk rheometer (TA Instruments Advanced Rheometer 2000), in cone-plate configuration, confirmed on a Thermo Rheo-Stress 600, also in cone-plate configuration. Some further measurements were performed with a TA Instruments ARES LS1, in parallel plate configuration.In all cases, a fixed shear rate $\dot{\gamma}$ is applied to the sample by rotating centre cylinder or the cone, and the shear stress σ required to produce the shear is measured. The viscosity μ is then simply given by

$$\sigma = \mu\dot{\gamma} \tag{7.1}$$

The range of shear rate used was from $1\,\mathrm{s}^{-1}$ to $100\,\mathrm{s}^{-1}$, which should encompass all expected shear rates that particles in the polymer solution might experience. Lower shear rates were available for some samples, however noise and measurement error increased drastically below $1\,\mathrm{s}^{-1}$.

7.3.3 Infra-red Spectroscopy

To check the polymer concentrations in each phase of a phase-separated fish gelatin / dextran mixture with and without the addition of salt, infra-red spectroscopy was performed upon freeze-dried samples of polymer. Freeze drying provides more accurate quantitative measurements as when polymers are free to diffuse within a droplet of sample, there may be preferential wetting of one polymer upon the measuring surface, skewing results. Additionally there is no need to know a precise concentration of water to remove its signal as background.

Samples of each phase of a 10% / 10% fish gelatin / dextran system at salt concentrations of 20mM and 85mM were extracted using the technique described above (Section 7.2.2). Small amounts of sample were placed in 1 ml Eppendorf tubes, covered with tissue paper and rapidly

frozen using liquid nitrogen. After 20 minutes freezing time, the samples were placed under vacuum for 24 hours to dry. Dextran-rich samples formed a powder, though samples rich in fish gelatin formed a continuous solid. In each case the samples were forcefully crushed using pestle and mortar to ensure a homogenous sample, and many measurements were performed on different extractions from the samples.

The freeze-dried powder was placed upon the diamond measurement lens of a Bruker ALPHA infra-red spectrometer, clamped in place to maximise the surface area of powder close to the lens. Pure freeze-dried fish gelatin and dextran spectra were also measured in order to provide a baseline for each. The measured spectra.

7.3.4 Zeta Potential Measurement

The zeta potential provides a simple and quantitative measurement of the surface charge of a particle. Measurements are performed using a Malvern Zetasizer. As laser doppler velocimetry is essentially a light-scattering technique, very low sample concentrations must be used to minimise multiple scattering.

When measuring the change in particle charge upon addition of charged polymer, particles are initially dispersed in Milli-Q water before being added to a highly dilute polymer stock, and the samples are shaken vigorously. Then 30 minutes is allowed for polymer diffusion to the particles before a zeta potential measurement takes place.

7.3.5 Total Organic Carbon measurement

The Total Organic Carbon content of a solution, measured with a Shimadzu TOC-V CSH machine, can indicate the presence or absence of dissolved polymer species. By adding particles to a polymer solution then centrifugally removing them, the adsorption of polymers to the particles can be measured.

Measurements are performed by injecting small quantities of solution into a high temperature micro-oven, and measuring the resulting heat generated through oxidation of the carbon atoms. In order to quantify the concentration of a polymer solution, first a calibration curve must be measured with a set of polymer solutions of known concentration. The result obtained from a TOC measurement is Area; that is, the area under a time/signal intensity graph obtained during injection of the sample.

To measure adsorption of polymers, particles are added to a polymer solution, with concentrations chosen such that in the case of no polymer adsorption (ie. maximum carbon content) the signal received by the TOC measurement is high to allow good resolution, but not high enough for saturation of the detector. Particle concentration is chosen such that under reasonable assumptions of surface coverage upon polymer adsorption, all polymer could be removed should adsorption take place. The particle/polymer solutions then undergo hard centrifugation and extraction of the supernatant in order to sediment the particles. Three such washes were enough to remove particles.

7.3.6 Contact Angle Measurement

The intersection of a solid surface with two fluid phases at thermodynamic equilibrium results in a contact angle defined by the interfacial tensions between the three phases. This contact angle will determine the resting height of a spherical solid particle at the interface between the two liquid phases at equilibrium.

The contact angle is hard to measure precisely microscopically due to the width of the interface and the spacial resolution of the optical microscope. A macroscopic observation can be performed by coating a surface with solid particles and resting a drop of one fluid phase against it, immersed in the other phase.

Many methods for measuring the contact angles of particles adsorbed to interfaces have been developed - both single particle [48, 73, 88] and multi-particle [19, 46] techniques. However the vast majority are specialised to oil/water interfaces.

The experimental setup to measure the macroscopic contact angle is shown in Figure 7.4, comprising a transparent bath filled with polymer solution, a droplet of opposing phase and the particle-coated substrate, between a camera and a light source. The setup has two configurations depending upon the relative densities of the phases under examination. At the pHs and salt concentrations of interest in these experiments, dextran is the denser phase. Hence measuring the contact angle of a dextran droplet with particles wetted with fish gelatin requires the particle-coated surface to be submerged facing upwards at the bottom of a bath of fish gelatin. The inverse case is more interesting as in other experiments generally particles begin wetted in the dextran phase, then move to the interface with fish gelatin. This requires the particle-coated substrate to be inverted within the bath. To reduce the trapping of air bubbles beneath the substrate, it is pre-wetted by slowly spreading dextran over it with a syringe before inversion.

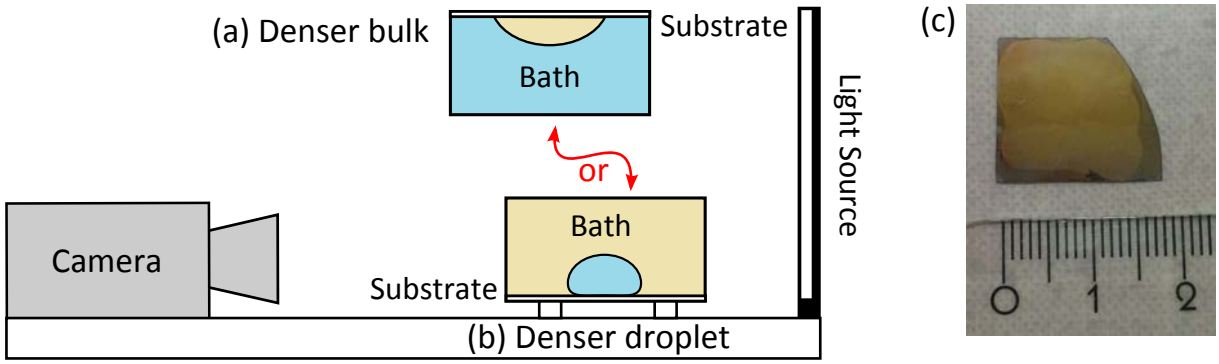

Figure 7.4: (a) and (b): Experimental setup to measure the 3-phase contact angle of a solid surface vs. fish gelatin and dextran. (a) shows the wetting of a droplet of fish gelatin within a dextran-rich bulk phase, with the substrate mounted at the top of the bath. (b) shows the inverse, with the substrate at the bottom. (c): A silicon wafer substrate is spin-coated with 500nm Sulphate latex particles. Under some angles of illumination the layer appears yellow due to scattering of light by the 500nm layers. Two layers are visible, with small areas around the edge of the wafer uncovered.

Preparation of Solid Substrate

Deposition of particles upon a silicon substrate is achieved through spin-coating. This results in a

layer of very even thickness. As the particles used are monodisperse and of typically micron-order size, transitions in number of layers of particles upon the substrate can be seen by eye.

A $\sim 1.5\,\text{cm} \times 1.5\,\text{cm}$ square of silicon wafer is cleaned with tetrahydrofuran (THF) then Milli-Q water, and wiped with Kimtech tissue. 1 minute under UV inundation at $40\,\text{mW}\,\text{cm}^{-1}$ improves adhesion of the particles. Once mounted within the spin coater, the wafer is blasted with compressed air to remove any dust, and $\approx 200\,\mu\text{l}$ of sample is added with a pipette, and spread to wet the whole surface with that pipette. Sample typically used is 2% wt 500nm Sulphate Latex solution, with 10mM NaCL added to aid adhesion through reduction of the particles' stability. The sample is then spun at 3000RPM for 1 minute. Many layers of particles are typically adhered, resulting in a slightly opalescent yellow coverage as shown in Figure 7.4c. This layer is resistant to dissolution when submerged in water.

7.3.7 Confocal Microscopy Adsorption Tracking

The adsorption dynamics of particles to the interface of a polymer/polymer ATPS have not previously been reported. A technique had to be developed to observe model particles and a model interface. 'Meeting Drop' samples, in which a single droplet of one polymer phase in which particles are dispersed comes into contact with a droplet of the opposing polymer phase were created as described in Section 7.2.3. The interface could then be watched with a confocal microscope, and adsorptions recorded. The fish gelatin phase was labelled with Rhodamine B, and the particles used were either fluorescent, or sufficiently large to be observed as a dark regions (eg $10\,\mu\text{m}$).

The microscopes used for this were a Leica TCS SP Confocal Laser Scanning Microscope (CLSM), and a Nikon Ti Spinning Disk Confocal Microscope equipped with an Andor Zyla fast camera.

Typically, samples were allotted 5 minutes equilibration time after the formation of the interface before adsorptions were observed, though no difference in measured trajectories was observed for adsorptions after 2 minutes or after 60 minutes.

With both the laser scanning microscope (Leica) and the fast camera of the Nikon microscope, the time resolution is determined by the inverse of the number of lines of the recorded image. Due to the difficulty of predicting the moment of adsorption for the colloidal particles, a wider field of view provides greater possibility of capturing an adsorption event in its entirety. However, the spacial resolution also determines the precision of the resulting captured trajectory. For the CLSM, typically an image of 32 to 64 lines was captured, which allowed a time resolution of 20 to 40 ms per frame. The fast camera on the Nikon microscope allowed faster capture of order 5 ms, so is well suited to the fast dynamics of small particles.

7.3.8 Scanning Electron Microscopy of particles

In understanding particle adsorption trajectories, in oil/water systems the nanoscale topology particle surface is all-important, as reported in Section 3.1.3. Whether this is also an important factor in water/water systems is not well understood, however characterisation of the particle surface is still therefore vital. Nanoscale features are well below the resolution limit of optical microscopy, so electron microscopy must be used. Scanning electron microscopy provides resolution of around

10 nm, which should be adequate to observe features that the broad water/water interface could interact with.

Samples of 1 µm, 4 µm and 10 µm Sulphate latex particles were dried upon silicon wafers, at a low concentration such that a monolayer of particles was more likely. These samples were examined with a FEI Scanning Electron Microscope.

7.4 Characterisation of our Water/Water System

7.4.1 Calculation of phase diagram position

The phase diagram of fish gelatin and dextran published by Vis et. al [109] does not include polymer concentrations high enough for the present study. However, as the same polymer system was used, also at stock pH and salt concentration, the phase diagram can be extrapolated to include the present study. This extrapolated phase diagram is shown in Figure 7.5.

The tie line for a system with no added salt and stock pH is assumed parallel to the data published for the same polymer system. The position along this tie line is extrapolated from the published data, and confirmed with IR spectroscopy of freeze-dried samples of equilibrated phases (method described in Section 7.3.3), extracted as described in Section 7.2.2. IR spectroscopy gives the proportion of each polymer as a percentage of the total polymer concentration, meaning knowing the tie line is necessary to give the polymer concentration in a solution.

Adding salt will change the position of the system along the tie-line, purifying phases. As the published data does not indicate the effect of salt upon the pH6 system, this phase diagram position can be measured using IR spectroscopy.

The equilibrium phase diagram positions for the systems in this study, calculated as described above, are given in Table 7.2 (on Page 98), along with the tie-line lengths for each. The infra-red measurements used are shown in Table 7.3, where the percentages given are in terms of each polymer's contribution to the total polymer concentration. The dextran-rich phase with low salt showed large variation across different samples, which may be an issue with the freeze-drying process concentrating trace amounts of fish gelatin together. From the phase diagram however it can be safely assumed the fish gelatin proportion is very small. This issue was not seen with the high salt system across multiple samples. The 100% pure samples may have an undetectable trace of opposing phase, though other experiments (Section 8.3) indicate this is unlikely.

Pure vs. Equilibrated Phases

For many experiments in this study, the polymer system begins as two equal unmixed phases of double the intended polymer concentration - eg., the 10% / 10% fish gelatin / dextran system begins as droplets of 20% fish gelatin and 20% dextran. When brought into contact, unless mixed through shear, the system will equilibrate through diffusion of water and polymer until the equilibrium positions indicated on the phase diagram are attained. The initial position of the 10% / 10% fish gelatin / dextran system is indicated on the phase diagram as open blue squares.

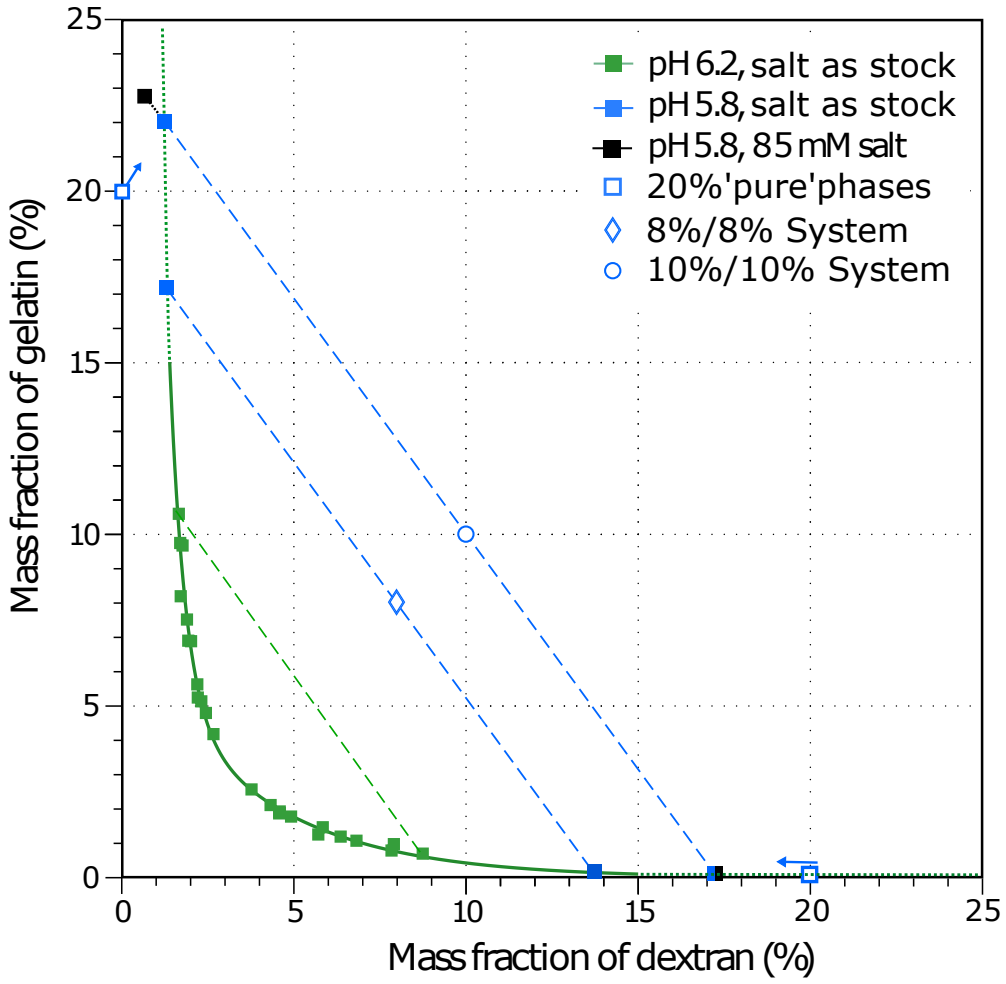

Figure 7.5: Extrapolation of published data by Vis et al. [109] to larger polymer concentration. Solid lines represent published phase diagram positions, dotted lines extrapolated positions. Tie-lines between phases in equilibrium are shown as dashed lines. The green pH6.2 system represents the published unadjusted stock salt concentration system. This is extrapolated to include the 8% / 8% fish gelatin / dextran , and 10% / 10% fish gelatin / dextran systems studied, with the points shown in blue, with the starting points of the systems shown as an open blue diamond and circle respectively. The addition of salt to the 10% / 10% fish gelatin / dextran system, shown as the black squares, results in an increase of the tie line length along the same tie line. The position along the tie line of the high-salt points are measured through IR Spectroscopy. When creating a 10%/10% system by mixing equal volumes of 20% polymer, the initial phase diagram position is indicated by the unfilled blue squares. The system will equilibrate through water and polymer diffusion till the filled blue squares are reached.

Table 7.2: Extrapolated and calculated values for equilibrium phase diagram positions of polymer systems used in this study. In each case, the system splits into a fish-gelatin-rich phase, and a dextran-rich phase. pH of the samples was 5.8.

	Fish Gelatin rich phase		Dextran rich phase		
Total polymer conc.	Fish Gelatin	Dextran	Fish Gelatin	Dextran	Tie line length (TLL)
8% / 8% 20mM Salt	17.2 %wt	1.3 %wt	0.2 %wt	13.7 %wt	21.1 %wt
10% / 10% 20mM Salt	22.1 %wt	1.2%wt	0.1 %wt	17.3%wt	27.2 %wt
10% / 10% 85mM Salt	22.6 %wt	0.6 %wt	0.0 %wt	17.4 %wt	28.2 %wt

Table 7.3: Mass proportions of each polymer within the dextran-rich and fish-gelatin-rich phases with and without added salt from a 10% / 10% fish gelatin / dextran system, as determined from infra-red spectroscopy of freeze-dried samples at pH 5.8. Errors shown are standard deviations for several samples.

System	**% wt. Fish Gelatin**	**% wt. Dextran**
Fish-gelatin-rich phase (20mM salt)	96.0 ± 0.5	4 ∓ 0.5
Fish-gelatin-rich phase (85mM salt)	97.4 ± 0.4	2.6 ∓ 0.4
Dextran-rich phase (20mM salt)	Not accurately measurable	
Dextran-rich phase (85mM salt)	0	100

7.4.2 Theoretical calculation of surface tension

To obtain a theoretical estimation of the surface tension of the surface tensions of the polymer systems used in these experiments, we can extrapolate published values from Reference [114], reproduced in Section 4.2.

Firstly, the surface tension depends most strongly upon the difference in concentration between the two phase-separated phases, given by the phase diagram tie-line length. For the two low-salt systems used, namely 10% / 10% or 8%/8% fish gelatin / dextran with 20mM salt at pH6, we can calculate the TLL from of Figure 7.5, with the results given in Table 7.2.

The surface tension that results from a given tie-line length, γ_0, scales as $TLL^{3.22}$ [112, 114]. The constant of proportionality, calculated from Figure 4.10a, is then:

$$\gamma_0 = 2.465 \times \mathrm{TLL}^{3.22}\,\mu\mathrm{N\,m^{-1}} \tag{7.2}$$

However, as fish gelatin is a polyelectrolyte, there is a small contribution to the surface tension due to charge imbalance across the interface (a so-called Donnan potential) [112,114]. The Donnan potential scales linearly with concentration, as demonstrated in Reference [114]. The addition of salt will reduce the Donnan potential to a negligible contribution [114]. The values for the Donnan potential for this system are extrapolated from Figure 5a of Reference [114], and given in Table 7.4.

The resulting change in surface tension, $\Delta\gamma$, as calculated in Ref [114], is found in reference to Figure 4 of Reference [114], for each system, and is again shown in Table 7.4, as is the resulting final calculation for the total surface tension, $\gamma = \gamma_0 - \Delta\gamma$.

Table 7.4: Table of surface tension values for each system. Effective salt concentration measured through conductivity measurements, and adjusted with addition of NaCl. γ_0, the surface tension due to concentration difference, is given by Equation 4.8.

Polymer Conc. (Gelatin / Dextran)	(Effective) Salt Concentration	TLL	Donnan Potential	$\Delta\gamma$	γ
8 wt% / 8 wt%	20 mM	21.1%	2 mV	0.3 µN/m	45.6 µN/m
10 wt% / 10 wt%	20 mM	27.2%	3 mV	0.5 µN/m	103.5 µN/m
10 wt% / 10 wt%	85 mM	28.2%	0 mV	0 µN/m	115.2 µN/m

7.4.3 Bulk Viscosity

When studying dynamics within a fluid system, it is essential to know the viscosity of the fluid. This is dependent upon the polymer concentration. The two initial polymer concentrations examined in this thesis are 8% / 8% and 10% / 10% fish gelatin / dextran . Each system will phase separate into phases with local polymer concentration according to the phase diagram (Figure 7.5), as given in Table 7.2. The viscosities of each polymer at each point in the phase diagram specified in Table 7.2 were measured. Results are presented in Figure 7.6. The viscous response is independent of shear rate for both polymers, indicating Newtonian behaviour. This is highly favourable for understanding particle dynamics as viscosity will not scale with particle velocity.

To check the scaling behaviour of the viscosity with concentration, additional datapoints of concentrations 16% and 20% were measured for each polymer, and up to 25% for the fish gelatin. The fish gelatin viscosity scales as a power law in the concentration with exponent approximately 4, indicating that it is in the semidilute regime.

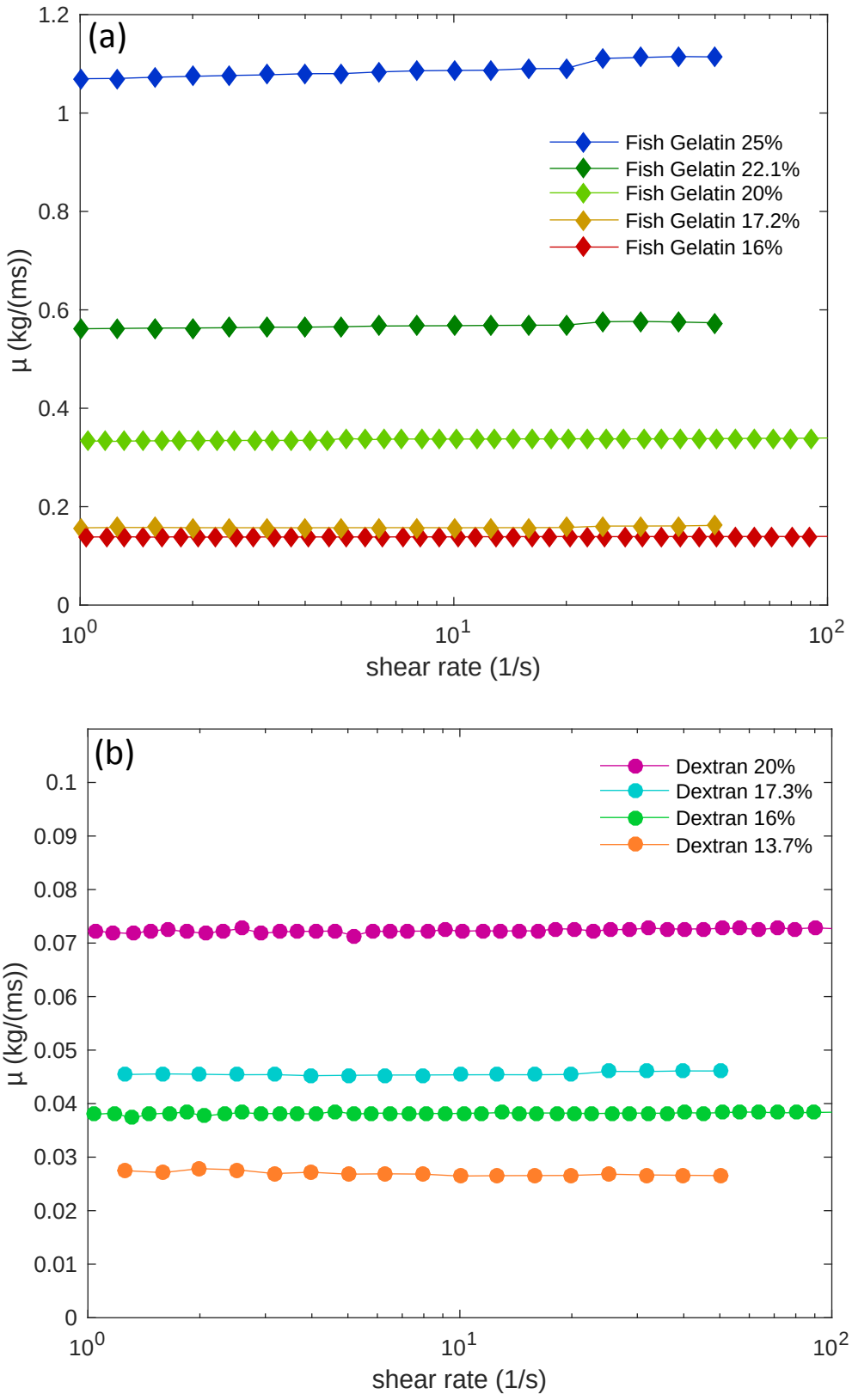

Figure 7.6: Bulk shear viscosity data for fish gelatin (a) and dextran (b), determined through bulk rheology. Polymer concentration provided in the legends. Noise reduces the datapoints for some samples.

Chapter 8

Particles in a Water/Water System

Contents

When studying the adsorption of particles to an interface, or attempting to create emulsions, knowing the interactions between the phases and the particles is important. For hard particles in oil/water systems, the interactions tend to be simple, characterisable by the three-phase contact angle when the particle is at interface.

The interaction of colloidal particles with a polymer/polymer ATPS has many more elements to consider. The interactions of polymers with the particles, both in terms of direct interactions such as electrostatic and charge interactions, and larger-scale interactions such as depletion all must be considered. Additionally, unlike the $\sim 3\,\text{Å}$ broad oil/water interface, the water/water interface can approach the size of particles in the system, meaning that a 'contact angle' may no longer be well-defined. Large particles must therefore be used.

The particles used in the experiments reported here are typically of diameter 1 µm or larger, so should make a defined contact angle with the $\sim 10\,\text{nm}$-broad interface.

8.1 Contact Angles

The contact angle that particles make with the interface determines the desorption energy of the particle, its resting height at interface, and hence the preferred curvature of the particle-laden interface. To estimate the wetting properties of particles with the fish gelatin / dextran interface, we performed simple experiments in which a droplet of one phase within a bath of the other phase

is allowed to wet a particle-coated substrate, as described in Section 7.3.6. The temperature was controlled at 20 °C, and the pH of the system was 5.8.

A 20% concentration droplet of fish gelatin was added to bath of 20% dextran and vice versa, meaning that the droplets must equilibrate through diffusion before reaching equilibrium phase diagram positions. As water can diffuse quickly throughout the sample compared to the slow relaxation of the droplets upon the substrate, this equilibration is not expected to have a large impact on measured contact angle, and other experimental errors (such as contact line pinning) may have a greater contribution.

First the three measurements are presented, then they are compared in Section 8.1.4.

8.1.1 Dextran droplet in fish-gelatin-rich phase

As dextran is the denser phase at stock pH and experimental salt concentration, the droplet of dextran rests on top of a sulphate-latex coated substrate. However, the droplet was never observed to wet the substrate, as shown in Figure 8.1.

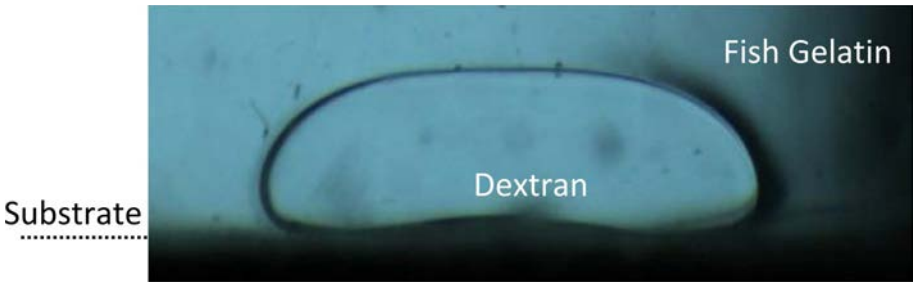

Figure 8.1: Contact angle measurement of a dextran droplet in a fish gelatin phase, wetting a substrate covered with 500 nm sulphate latex particles, after 5 hours of equilibration. Image width: 15mm

8.1.2 Fish gelatin droplet in dextran-rich phase: low salt

Using an inverted substrate, a fish gelatin droplet was examined wetting from a dextran phase, as shown in Figure 8.2. The measured contact angle after equilibration was $(19.5 \pm 1.0)°$, averaged across both sides of 3 droplets. The contact angle showed some tendency to be pinned, possibly due to the large roughness of the surface, but several drops relaxed to the same contact angle after ≤ 2 hours.

8.1.3 Fish gelatin droplet in dextran-rich phase: high salt

The salt concentration of the system was raised from 20 mM to 85 mM using NaCl. The contact angle in this system was $(22 \pm 1)°$, again with some tendency for pinning, but with no contact angle measured less than 22°.

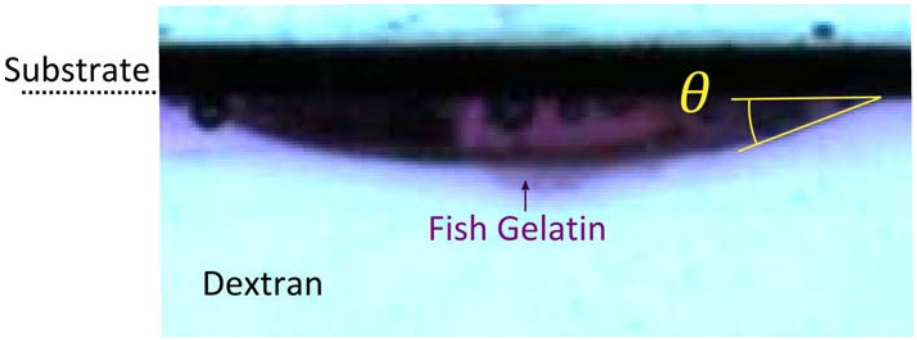

Figure 8.2: Contact angle measurement of a fish gelatin droplet inside a dextran phase with salt content 20mM, wetting a substrate covered with 500 nm sulphate latex particles, after 5 hours of equilibration. Image width: 10mm

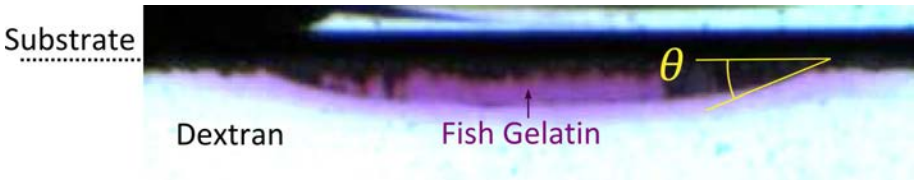

Figure 8.3: Contact angle measurement of a fish gelatin droplet inside a dextran phase with a salt content of 85mM, wetting a substrate covered with 500 nm sulphate latex particles, after 5 hours of equilibration. Image width: 10mm

Table 8.1: Macroscopic contact angle measurements for droplets of one polymer solution within a bulk phase of the other polymer solution, resting against a substrate of spin-coated 500 nm Sulphate latex colloidal particles

System	Contact Angle
Dextran in F.G.	No Wetting
F.G. in Dextran, 20mM Salt	$(19.5 \pm 1.0)^\circ$
F.G. in Dextran, 85mM Salt	$(22 \pm 1)^\circ$

8.1.4 Comparison

The total wetting of fish gelatin in Figure 8.1 may be due to fish gelatin completely wetting the particles with a contact angle of 0°, or this may be caused by irreplaceable adsorption of fish gelatin to the particle surfaces, and/or a non-draining film of fish gelatin forming between the dextran phase and the particles. If the contact angle is indeed zero indicating complete wetting, the contact angle observed for the inverse system in Figure 8.2 could be caused by pinning of the contact line on the rough particle-coated substrate. However, in microscopic studies a contact angle of 0° is never observed despite experimental times on the order of hours.

Though from the dextran droplet experiment, we can infer that particles, once wetted with fish gelatin, either require large amounts of shear to be brought back to the interface or may not wet the interface again at all.

When salt is added to the system, the contact angle increases from 19.5° to 22° (Table 8.1). This can be attributed to the increase in interfacial tension incurred when salt purifies the phases, as explained in Section 4.2. The surface tension with and without salt is, from Table 7.4, 115.2 µN/m and 103.5 µN/m respectively. To calculate the expected change in contact angle this induces, we

look to Young's law:

$$\cos(\theta_E) = \frac{\gamma_{S,Dex} - \gamma_{S,FGel}}{\gamma_{Dex,FGel}} \tag{8.1}$$

where subscript S represents the solid substrate, Dex the dextran phase and FGel the fish gelatin phase. If only $\gamma_{Dex,FGel}$ changed upon the addition of salt, the contact angle at the higher salt concentration would be 33°. This is somewhat different from the measured value, which could suggest an influence of fish gelatin adsorbing onto the particle surfaces, or a small change in interaction between the particle and either polymer.

8.2 Polymer Adsorption

The adsorption of polymers on to the surface of a colloidal particle can in principle be measured with DLS [107]. However, with slight polydispersity of particles and small size of the polymers ($\sim 10\,\text{nm}$), this proved very difficult to measure. However, the particle surfaces and the fish gelatin bear a negative and positive charge respectively, so through measuring the surface charge of the particles with and without added fish gelatin, adsorption can be qualitatively observed.

An additional technique to measure the adsorption of charged or uncharged organic polymers is to measure the change in carbon content of a dilute polymer solution once particles are added. Through centrifugation, particles can be removed completely from the solution, and all remaining carbon content can be ascribed to the presence of unadsorbed polymer.

All experiments reported in this section are at the stock pH of 5.8.

8.2.1 Zeta Potential

The zeta potential of particles indicates the charge of particles at the 'slipping plane', i.e. the outer shell of ions which surrounds charged particles. This, measured by a Malvern Zetasizer, as described in 7.3.4, gives an indication of the surface charge of particles.

Table 8.2: Zeta potential results for 500 nm Sulphate latex with added fish gelatin and/or dextran.

Sample	**Zeta Potential** (mV)	**St.Dev** (mV)
0.01% Fish Gelatin	3.8	3
0.01% Latex	-33	6
0.01% Latex + 0.25% Dextran	-34	5.5
0.01% Latex + 0.0165% Fish Gelatin	0.2	2.2
0.01% Latex + 0.165% Fish Gelatin	9	3.5
0.01% Latex + 0.25% Dextran + 0.0165% Fish Gelatin	-1.5	3.5
0.01% Latex + 0.25% Dextran, + 0.165% Fish Gelatin	7	3.5
0.01% Latex + 85mM NaCl	-33	6
0.01% Latex + 85mM NaCl + 0.0165% Fish Gelatin	-0.1	4

Table 8.2 shows that Fish Gelatin is positively charged, and the Sulphate latex particles negatively charged. However, upon addition of fish gelatin solution, the particles become positively

charged, indicating polymer adsorption. This charge inversion indicates that electrostatic interactions are not responsible for polymer adsorption. (The freely diffusing fish gelatin molecules will not contribute to the measured value, as the measurement is achieved through light scattering and hence the larger particles dominate the measurement).

As dextran is uncharged, it does not change the measured potential. However if fish gelatin is then added, the charge increases. At the same fish gelatin concentration, the charge of the particles is the same within error bars in the presence of dextran. This indicates either that dextran does not adsorb onto the particle surface, or that it is easily replaced by or covered over with adsorbed fish gelatin. The next section however presents results indicating dextran does not adsorb.

Finally, adding salt to the fish gelatin solution has no effect upon the resulting charge, indicating that salt concentration may not affect the extent of polymer adsorption. This further indicates that electrostatic interactions are not responsible for polymer adsorption, meaning instead the hydrophobic interaction is most likely responsible.

8.2.2 Total Organic Carbon

Measurement of total organic carbon of a solution gives the carbon content in arbitrary units. To convert these arbitrary units to wt% concentration of a polymer solution, a set of calibration measurements must be taken of a range of polymer concentrations. These measurements are shown for fish gelatin and dextran in Appendix C.

To choose our relative quantities of polymer and particles, we must examine the surface area each contributes to the system. The quantity of adsorbed polymer depends upon the available surface area of particles. The surface area of particles per unit volume of solution can be calculated given the density of polystyrene latex, $\rho_L = 1.055\,\mathrm{g\,cm^{-3}}$:

$$a_{\mathrm{particles}} = \frac{3c_{\mathrm{particles}}}{R\rho_L} \tag{8.2}$$

The surface area of polymers can be approximated by guessing that polymers will adsorb covering an area approximately equal to that of their radius of gyration, which for the dextran and fish gelatin used are 10 nm and 8 nm, respectively [109]. Then, given the molecular weights M_{poly} of the polymers, the potential surface area covered by a single layer of adsorbed polymers per unit volume solution is:

$$a_{\mathrm{poly}} = \frac{\pi R_g^2 N_A C_{\mathrm{before}}}{M_{\mathrm{poly}}} \tag{8.3}$$

where N_A is Avogadro's number, and C_{before} is the concentration of polymer before centrifugation of the sample. Comparing these two areas, an approximate maximum polymer coverage can be estimated. The real polymer coverage is revealed by the change in polymer concentration in the supernatant once the particles are removed, $C_{\mathrm{after}}/C_{\mathrm{before}}$). This means the polymer adsorbed to the particles covers a proportion (typically represented by the letter θ) of the available surface area given by:

$$\theta = \left(1 - \frac{C_{\mathrm{after}}}{C_{\mathrm{before}}}\right) \frac{a_{\mathrm{poly}}}{a_{\mathrm{particles}}} \tag{8.4}$$

If this coverage θ is high (ie. $> 100\%$), the polymer may adsorb in more than one layer, or more close-packed than its radius of gyration. Measuring the Total Organic Carbon content allows measurement of C_{after} to quantify this adsorption.

Table 8.3 shows the results of the adsorption tests. Dextran showed no difference in carbon content before and after addition of particles (within experimental uncertainty), implying that dextran does not adsorb to sulphate latex particles. Fish gelatin showed no carbon remaining in the supernatant, implying that fish gelatin readily adsorbs to sulphate latex particles.

Further, given the quantity added was sufficient to cover 500% of the particle surface with polymers of surface area πR_g^2, we can conclude that fish gelatin adsorbs in multiple layers and/or more close-packed than while in bulk.

Table 8.3: Concentration of polymer in supernatant before (C_{before}) and after (C_{after}) addition and centrifugal removal of 1000nm Sulphate latex particles.

Sample	$C_{\text{particles}}$	**Max surface coverage***	**Polymer conc.** C_{before}	**Polymer conc.** C_{after}	**Real surface coverage** θ
Dextran (Low conc.)	0.001 wt%	$\sim 100\%$	0.005 wt%	0.0043 wt%	14%
Dextran (High conc.)	0.001 wt%	$\sim 270\%$	0.0125 wt%	0.01 24 wt%	1%
Fish Gelatin	0.0002 wt%	$\sim 500\%$	0.050 wt%	0.000 wt%	500%

* - Given by ratio of particle surface area to estimated polymer surface area, $a_{\text{poly}}/a_{\text{particles}}$.

8.3 Aggregation and droplet nucleation

Polymer adsorption has a complex influence upon particles in a fish gelatin/dextran system. In low salt conditions, fish gelatin diffusing in the dextran-rich phase adsorbs to the particles, and alters the local phase diagram. Subsequently, a coating of fish gelatin nucleates around particles. This is demonstrated in Figure 8.5, where a 20% fish gelatin droplet is brought into contact with a 20% dextran droplet, in which 200 nm Carboxylate latex particles are dispersed. The preparation of these samples is described in Section 7.2.3.

In dextran (or fish gelatin) alone, particles do not aggregate. However, once the droplets come into contact, the polymers slowly interdiffuse to reach thermodynamic equilibrium. Due to their strong preference for the fish gelatin phase, the particles act as 'sinks' for the small quantity of fish gelatin in the dextran phase. A coating of fish gelatin grows over time, which causes aggregation of particles due to capillary bridging. Close to the dextran/gelatin interface, the concentration gradient is steepest so diffusion occurs at the fastest rate, and the aggregates collapse into spherical fish gelatin droplets with the particles fully wetted inside within hours. This is represented schematically in Figure 8.4.

This behaviour is not observed in the presence of salt, which is experimental evidence for the purification of phases. Figure 8.6a shows a meeting drop sample in the presence of salt after 24 hours, and no aggregation occurs even after many days. Additionally, no aggregation occurs when particles are dispersed in the fish gelatin phase (Figure 8.6b), despite dextran diffusing more freely

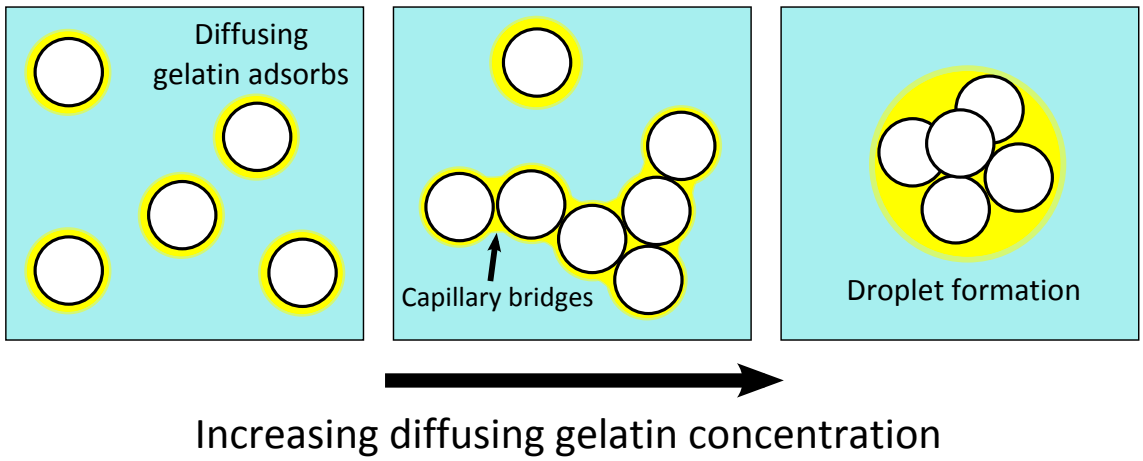

Figure 8.4: Schematic of the aggregation of particles due to diffusing gelatin forming capillary bridges, eventually leading to droplet nucleation. From left to right, the concentration of diffusing gelatin increases. Eventually the aggregate or the nucleated fish gelatin phase becomes so large that surface tension collapses the aggregate into a spherical droplet.

through a fish-gelatin-rich phase than vice versa. This indicates that adsorption, or at least the hydrophobic interaction, may play a role.

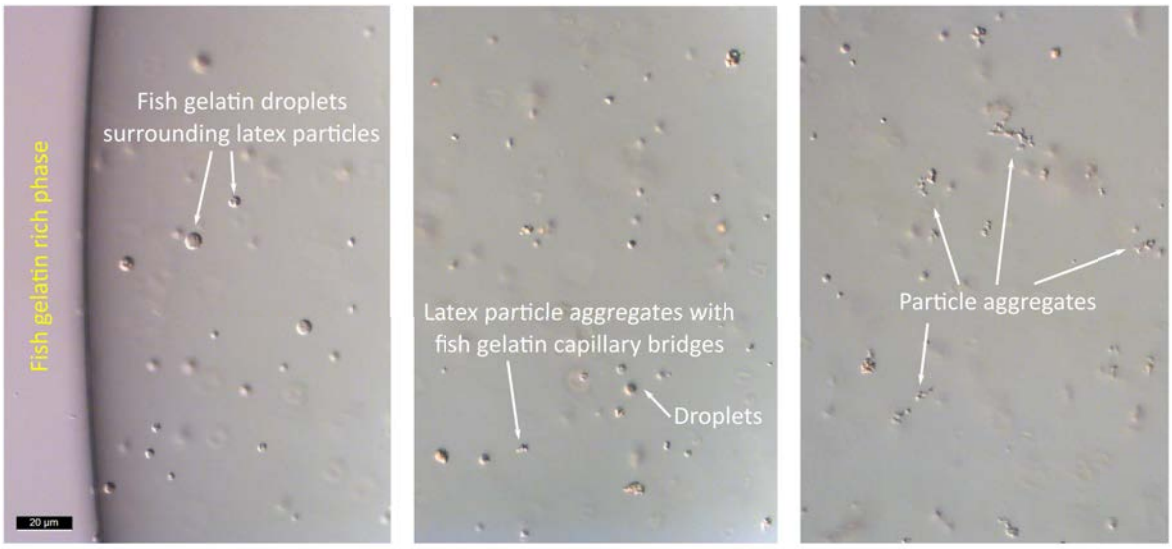

Figure 8.5: 200nm Carboxylate-functionalised latex particles dispersed in 20% dextran solution, close to the interface with a 20% fish gelatin solution, within a sample cell as described in Section 7.2.3. Sample aged for 24 hours. Left: At interface, diffusion of fish gelatin through sample causes nucleation of droplets of fish gelatin around particles. Centre: 1mm from interface, transition zone from nucleated droplets to capillary-bridged aggregates. Right: 2mm from interface, disparate aggregates connected with capillary bridges of diffused gelatin.

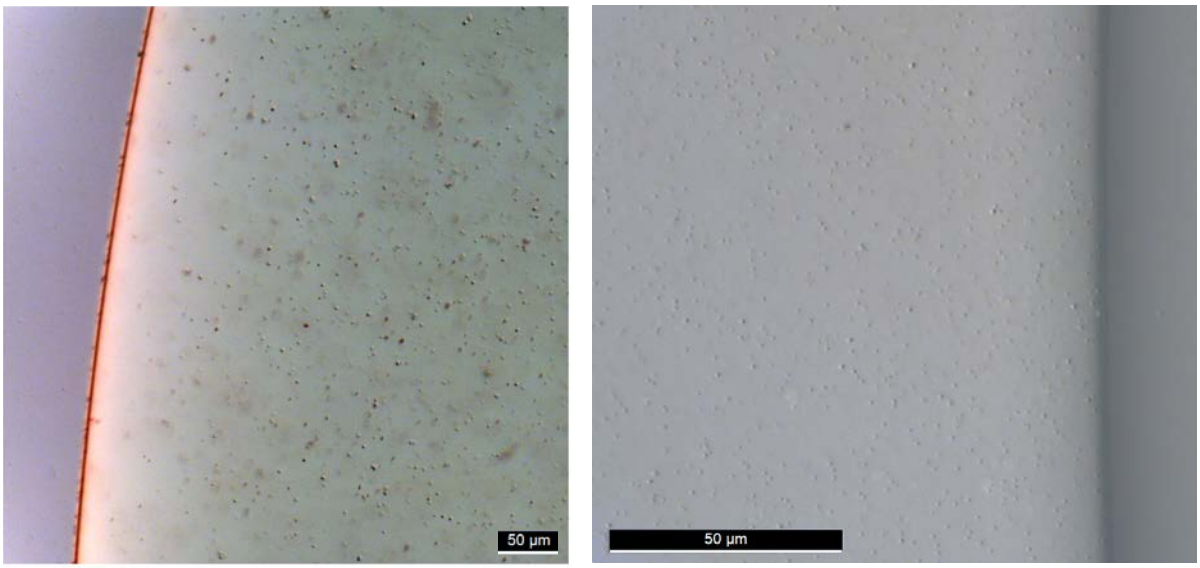

Figure 8.6: (a) 200nm Carboxylate-functionalised latex particles dispersed in 20% dextran solution, close to the interface with a 20% fish gelatin solution, with a total salt concentration of 85mM. Within a sample cell as described in Section 7.2.3. Sample aged for 24 hours. With added salt, no aggregation or nucleation of fish gelatin droplets occurs, even after many days. This provides evidence that salt purifies the dextran phase, preventing the diffusion of fish gelatin. (b) Particles dispersed in Fish Gelatin show no aggregation even with no added salt, after many days.

Chapter 9

Stabilising Water/Water Emulsions

Contents

One of the goals of understanding particles in water/water systems is the stabilisation of water/water emulsions through the Pickering mechanism, introduced in 3.1.2. This section explores attempts to stabilise fish gelatin/dextran systems with spherical colloidal particles. The sample preparation and emulsification methods are explained in Section 7.2.1. Figure 9.1b illustrates the desired goal of droplets of one phase suspended within a matrix of the other phase.

9.1 Measuring stabilisation

Microscopically, the presence of a high concentration of particles at the interface of a droplet would indicate the possibility of interfacial protection. Stabilisation is judged macroscopically through many observations:

- the presence of a turbid phase,
- reduction in the volume of separated phases at the top and bottom of the sample,
- delay in formation of separated phases,
- rheological changes such as resistance to flow (implying bridged droplets).

To maximise the possibility of stabilisation, many parameters were controlled. Multiple particles of different materials and with different surface chemistries were examined. To check for Pickering behaviour, ie. a dependence of the emulsion droplet diameter on $1/C_{\text{particles}}$, a range of particle concentrations were examined. To tune the interactions between polymers and particles, the pH was changed. The role of high and low shear was examined through comparing samples mixed through gentle stirring, shaking, and high-speed UltraTurrax. Finally, the influence of temperature

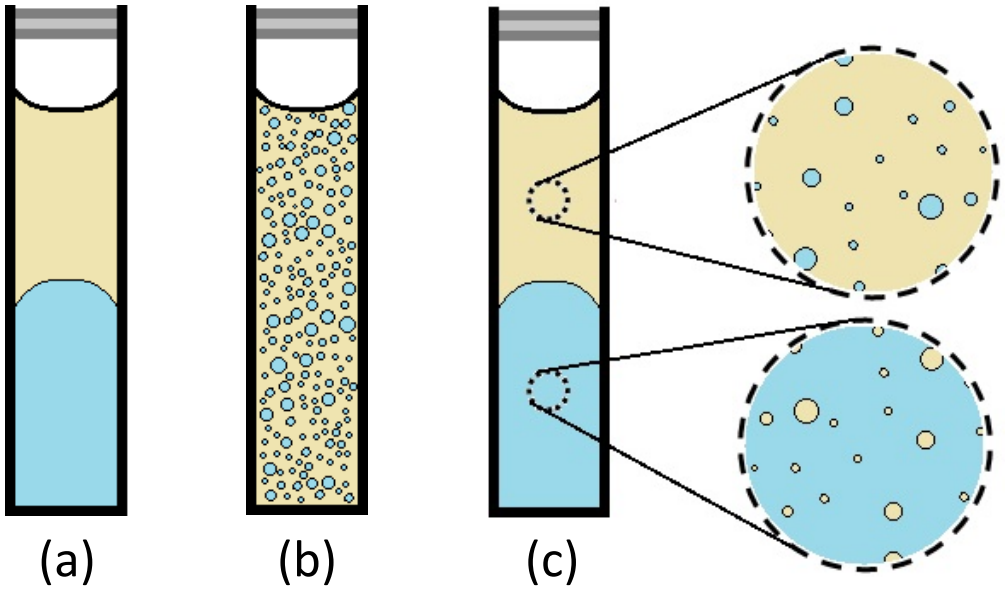

Figure 9.1: Schematic of stabilisation vs. destabilisation. Fish gelatin rich regions shown in yellow, dextran-rich in blue. Samples are contained within 4ml square plastic cuvettes. a) the initial condition of demixed polymer solutions. b) After mixing through shear, droplets of one polymer will form within a matrix of the other. If the particles added to the system stabilise the interface, the system will remain in this form.If stabilisation is not successful, the system will resemble c) wherein bulk dextran-rich and fish-gelatin rich phases form, but droplets of each opposing phase are still observed due to the small difference in density between phases and large viscosity.

was briefly considered, ageing emulsions at 14 °C, close to the gelling temperature of fish gelatin around 10 °C.

Table 9.1 summarises the results.

Table 9.1: Summary of emulsion stabilisation attempts. Samples were prepared as described in 7.2.1. Unless stated otherwise, samples were emulsified through manual shaking for 5 minutes, and ageing took place at room temperature (20 °C). Results recorded after 24 hours. pH5.8 represents stock pH. D is the particle diameter.

D (nm)	Particle Type	pH	Particle Conc. (wt%)	Other Parameters	Macroscopic Observations	Microscopic Observations	Figure
400	Silica (uncoated)	5.8	0.01 to 0.16		*	No particles observed at interface.	
500	Sulphate Latex	5.8	0.001 to 1.2		*	†	9.2, 9.3a) & b), 9.4a).
500	Sulphate Latex	6.6	0.05		*	†, slightly more particles at interface than pH 5.8.	
500	Sulphate Latex	7.5	0.05 and 0.1		*	†, slightly more particles at interface than pH 6.6.	
500	Sulphate Latex	7.5	0.05 and 0.1	Stored at (14.5 ± 1.0) °C	*	†, as above.	
500	Sulphate Latex	8.6	0.05 and 0.1		*	†, most particles at interface of pH range.	9.4b)
500	Sulphate Latex	8.6	0.05 and 0.1	Stored at (14.5 ± 1.0) °C	‡, week lifetime	†, as above.	
1000	Sulphate Latex	8.6	0.05 and 0.1	Stored at (14.5 ± 1.0) °C	‡, $\sim$ 4-day lifetime	†	
500	Sulphate Latex	8.6	0.05 and 0.1	UltraTurax 3kRPM for 5 minutes	*	†, fewer particles at interface than when shaken	
500	Sulphate Latex	10.2	0.05		*	†, fewer particles at interface than pH 8.6.	9.4c)
1500	COOH-coated Silica	5.8	0.025 to 0.1		*	†	9.3c) & d)
1500	NH_2-coated Silica	5.8	0.025 to 0.1		*	No particles observed at interface.	
1500	COOH-coated Silica	6.6	0.05		*	†, more particles than at pH 5.8.	
1500	NH_2-coated Silica	6.6	0.05		*	No particles observed at interface.	
1500	COOH-coated Silica	8.6	0.05		*	†, most particles observed of all pHs. However, particles also aggregate in the fish gelatin phase and at interface.	
1500	NH_2-coated Silica	8.6	0.05		*	No particles observed at interface.	
1500	COOH-coated Silica	10.2	0.05		*	†, particles all within aggregates.	

† - Some particles observed at interface, most in the FG phase. Little or no influence of particle bulk concentration upon particle surface concentration.

* - No delay in phase separation. Some minor influence of presence of particles in the shape of the macroscopic interface.

‡ - Due to low temperatures approaching onset of gelling, mm-sized droplets of fish gelatin appear. These droplets are stable on the order of days, however they appear identically in the particle-free control sample.

9.2 Role of particle concentration

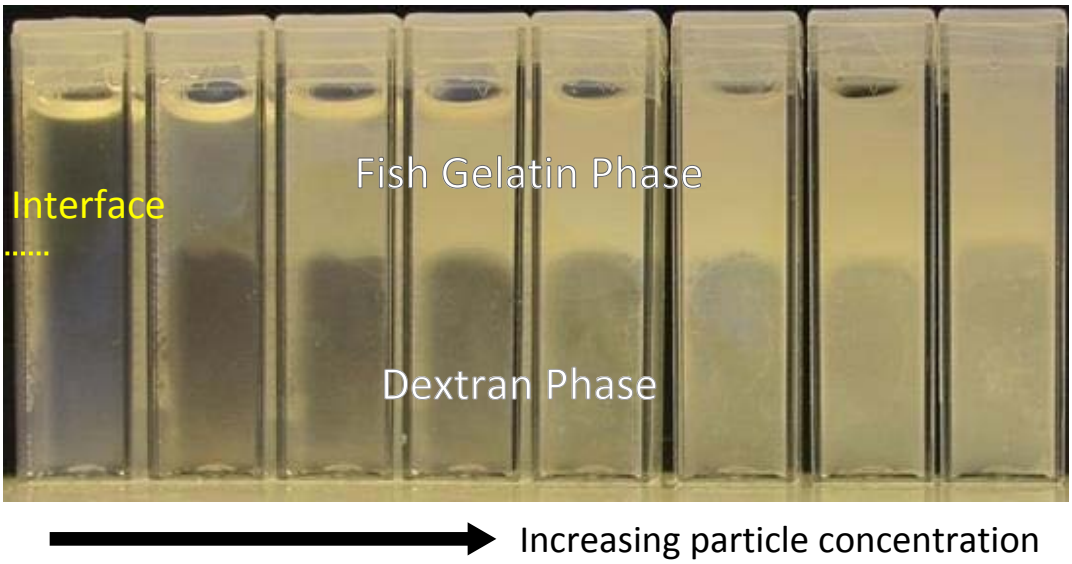

Figure 9.2: Emulsions prepared with 10% fish gelatin and 10% dextran, with 500 nm Sulphate latex particles at concentrations of 0%, 0.001%, 0.005%, 0.01%, 0.02%, 0.04%, 0.08%, 0.8% from left to right. pH is as stock, 5.8. Images taken after 24 hours of ageing.

As previously discussed, the particles show a strong preference for the fish gelatin phase, and once wetted with fish gelatin they no longer are easily wetted with dextran. In an emulsion setting, this means that the majority of particles are found in the fish gelatin phase after shear. Figure 9.2 shows a set of emulsions with a range of 500 nm Sulphate latex particle concentrations, from 0% to 0.8%. Timelapse video of the phase separation process showed no discernible difference in phase separation dynamics with increasing particle concentration.

Microscopy images, such as Figure 9.4a, showed that although some particles were at interface, the majority were in the bulk fish gelatin phase. Despite particles being initially dispersed in the dextran phase, not a single particle was observed there after phase separation.

To test whether increasing the particle concentration would force particles to the interface, samples with particle concentration as high as 1.2 wt% were created. These too showed no difference in phase separation dynamics, and as Figure 9.3a and b show, the fish gelatin bulk phase and droplets remain saturated with particles, with few located at the interface.

9.3 Tuning particle-polymer interaction: pH and surface chemistry

To improve the stabilising effect of particles, the number of particles at interface must be increased. This might be achieved through improving the particles' preference for the dextran phase. As shown in Figure 4.11, the charge of fish gelatin is dependent upon pH, being positive at low pH (such as the stock pH of 5.8) and negative at high pH. Sulphate and carboxylate particles are negatively charged, meaning there will be some electrostatic attraction between the fish gelatin phase and the

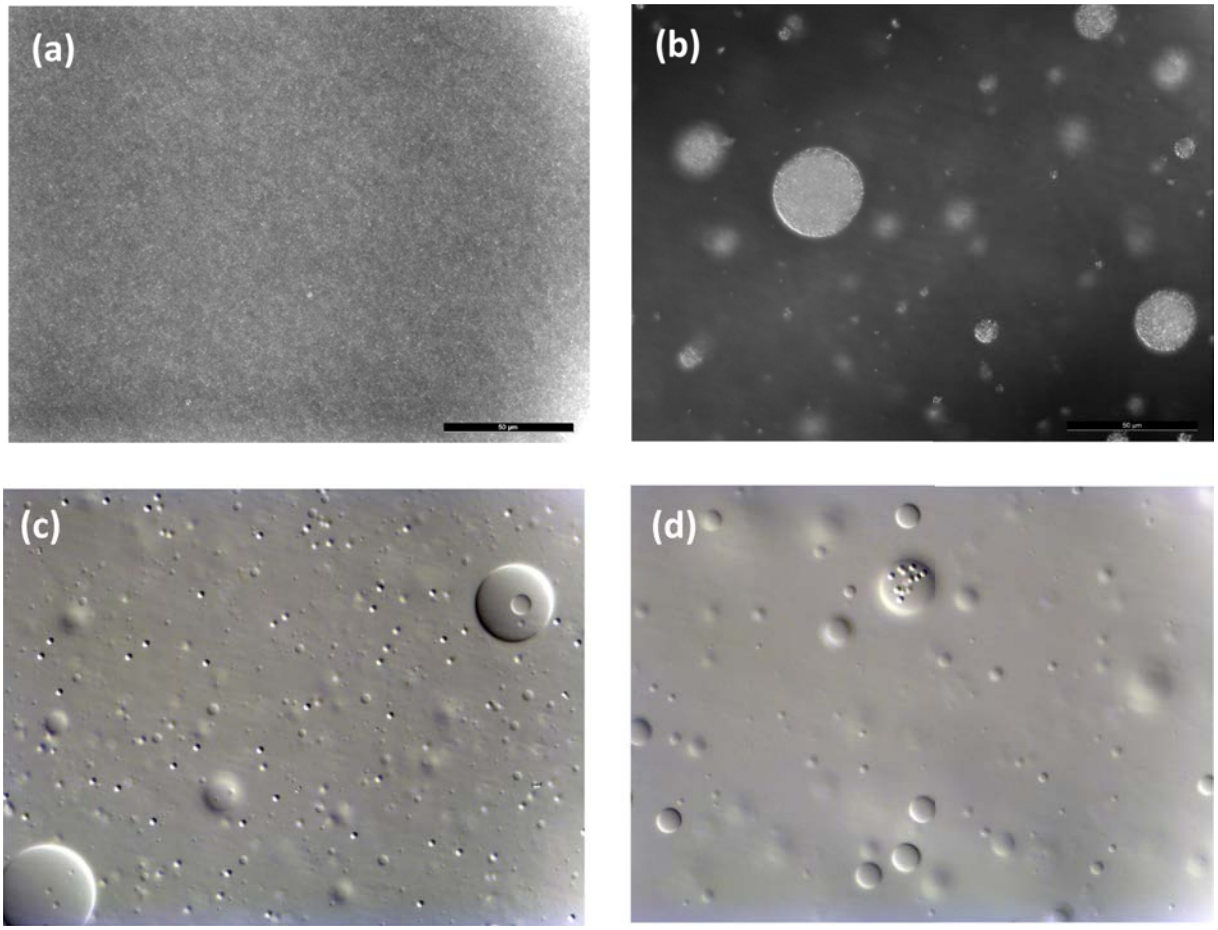

Figure 9.3: White light microscopy images of upper and lower phases of phase-separated 10 wt% fish gelatin / 10 wt% dextran emulsions. (a) upper phase of an emulsion prepared with 1.2 wt% of 500 nm Sulphate Latex particles. Particles exhibit such strong preference for the fish gelatin phase that the upper (fish gelatin-rich) phase becomes almost saturated with particles. (b) the lower phase of this emulsion, showing particle-saturated droplets with few observable at interface. (c) upper phase of emulsion with 0.05 wt% 1500 nm COOH-coated Silica particles. (b) lower phase.

particles at low pH. The pH was increased therefore to try to weaken or reverse this effect, and particles of different surface chemistries were examined.

No pH or surface chemistry change resulted in macroscopic stabilisation. However, as Figure 9.4 shows, a maximum of particles at interface was observed at pH 8.6, at which fish gelatin would exhibit a small negative charge. However, most particles were still in the bulk fish gelatin phase at every pH. The dynamics of stabilisation are difficult to compare between pH values, as with increasing pH the polymers' solvency changes, causing two density inversions. At pH < 7 and pH > 9, the dextran-rich phase is the denser, whereas around its isolectric range of pH 7 to 9, the fish-gelatin-rich phase is the denser. This makes comparing density-driven creaming rates a poor judge of stabilisation. However, as no pH exhibited well-covered droplet interfaces, it is safe to assume pH has only a small contribution on particles' interfacial preferences. This can be ascribed to the hydrophobic interaction dominating fish gelatin's interaction with the particles, rather than charge.

Additionally, COOH-coated and NH_2 coated Silica particles were tested at each pH. The COOH particles showed a greater tendency to be found at interface than the NH_2, though neither improved over the latex particles. Figure 9.3 shows that again the majority of particles were found in the fish gelatin phase.

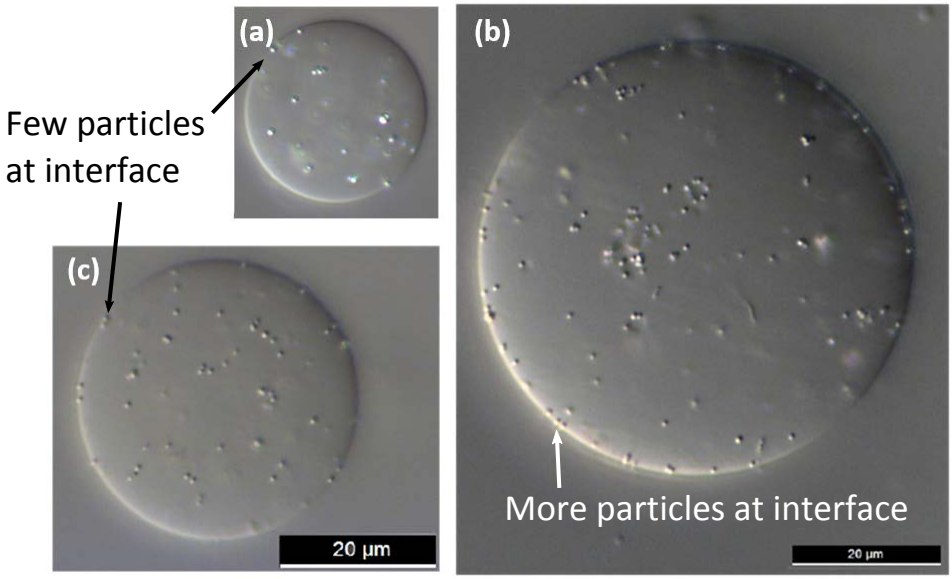

Figure 9.4: Effect of pH upon the presence of particles at interface. (a) shows a fish gelatin droplet in a dextran matrix at pH 5.8. Some particles are at interface, though the majority are in bulk. (b) At pH 8.6, a maximum of particles are observed at interface, however coverage is still very poor. (c) pH 10.2, fewer particles are seen at interface.

9.4 Influence of shear: stirring vs. shaking vs. UltraTurrax

As in every case the particles are dispersed in the dextran phase, the particles must cross the interface to reach the fish gelatin phase. To test this qualitatively, a simple experiment was performed where a 10ml 10% / 10% fish gelatin / dextran mixture with 0.05 wt% 500 nm Sulphate latex particles dispersed within the dextran phase was mixed with two different shear methods, gentle stirring

and shaking, and the phase separation was observed from above with a timelapse camera. The experimental procedure is detailed in Section 7.3.1.2.

The results are shown in Figure 9.5. The fish-gelatin-rich phase is the droplet-forming phase, while the dextran-rich phase is the matrix. The particles are clearly visible as white opacity. After gentle stirring, the particles have not left the dextran phase, and the fish gelatin phase remains very clear. After shaking, the fish gelatin phase becomes highly opaque, and the dextran phase very clear.

This indicates that at low shear, particles do not cross the interface, and that shaking counts as a 'high shear' in this system.

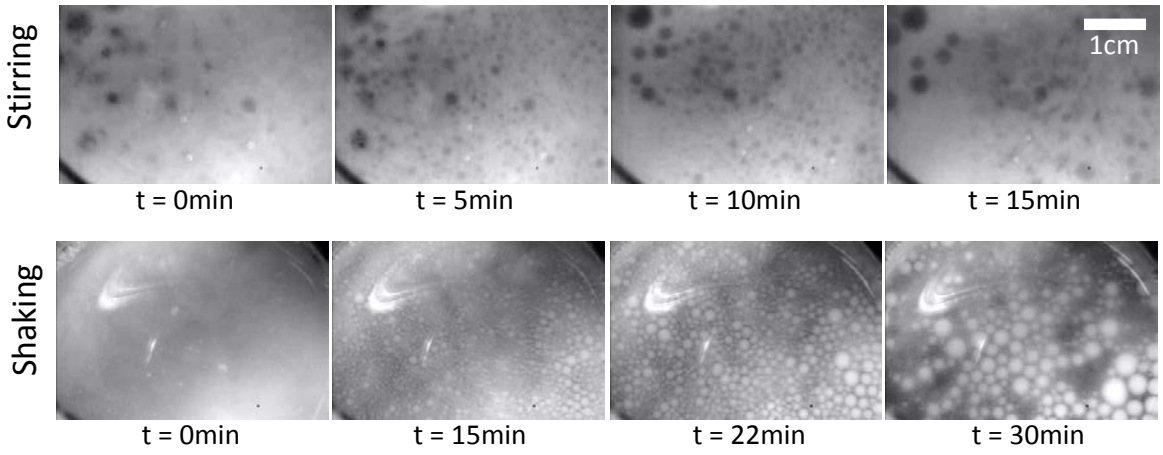

Figure 9.5: Comparing gentle stirring and shaking for a 10% / 10% fish gelatin / dextran system, with 0.05 wt% 500 nm Sulphate latex particles dispersed within the dextran phase. pH chosen at 8.6 to maximise particles' presence at interface. The phases can be distinguished as the fish-gelatin-rich phase forms droplets within the dextran-rich phase. The particles are observable as white opacity in the sample. The sample was mixed in two ways. Top: Gentle stirring with a 2mm-diameter glass rod for 2 minutes. Bottom: Strong manual shaking for 2 minutes. In each case, the sample became fully visibly mixed, with no droplets visible. Change in droplet opacity after shaking indicates that particles have crossed to the fish gelatin phase.

To ensure that an even higher shear does not bring all particles nicely to interface, a test was performed emulsifying the same system with an Ultra-Turrax mixer, at 3kRPM for 5 minutes. This resulted in possibly even fewer particles at interface, consistent with the previous experiment.

The behaviour of particles in an emulsion, especially in regards to their entering and staying at an interface while the system undergoes shear, is highly dependent upon their adsorption kinetics [117]. The following chapter presents experimental work tracking the adsorption dynamics of spherical particles to the water/water interface, and compares the resulting trajectories to theoretical models at the oil/water or air/water interface.

Chapter 10

Dynamics of Particles at the Water/Water Interface

Contents

This chapter presents the results obtained tracking the adsorption of colloidal particles to the interface of a fish gelatin / dextran system. Measuring the dynamics in this way is interesting for two separate fields - firstly the dynamics give insight into the forces and timescales involved when attempting to stabilise a polymer/polymer ATPS with colloidal particles, which may lead to improvements in water/water emulsions. Secondly, the adsorption dynamics of particles to liquid-liquid interfaces is an area of intensive theoretical, experimental and computational work (see Section 3.1.3). Thus far, studies have entirely focussed on the oil/water interface. The water/water interface provides a means of testing the universality of the theories presented thus far for the dynamics of particle adsorption.

10.1 Experimental Results

10.1.1 Confocal particle tracking & analysis

The results obtained here used confocal laser-scanning microscopy to observe the adsorption of individual colloidal particles to a model interface formed between droplets of fish-gelatin-rich and dextran-rich polymer solutions. The preparation of samples is described in Section 7.2.3, and the capturing of adsorptions with confocal microscopy in Section 7.3.7. The pH of all samples is that of the stock solution - around 5.8. The temperature in every case was controlled at 20 °C.

A sample of a tracked adsorption is shown in Figure 10.1. Figure 10.1a shows frames from the microscope footage of the tracking. As demonstrated in the image, a circle is manually fitted to the particle image. However, in the second and third frames, an optical aberration is visible wherein a second image of the particle appears. The slight difference in index of refraction between the fish gelatin phase and the dextran phase, combined with the curved shape of the interface far below the focal plane cause a doubling of all light from the focal plane. The second image occurs at a distance z_{diff} from the first image. The images can be resolved quite distinctly from one another.

To ensure that this optical effect has no influence on measured particle positions, Figure 10.1b shows tracking data for both particles, and gives the position of both interface images. Figure 10.1c shows the distance between the two images z_{diff} is constant whatever the particle's position at interface, hence either particle image can be tracked accurately.

For early dynamics, and to accurately capture the moment of acceleration, tracking the lower image of Figure 10.1a, appearing in the dextran phase, is necessary. For dynamics only concerned with later times, tracking of the upper image (appearing in fish gelatin phase) would be preferable. Tracking both for some time to accurately measure z_{diff} would allow superimposition of the curves, giving the most complete capturing of the trajectory.

From the trajectory in Figure 10.1b, the following stages of motion are apparent:

- The particle slowly approaches the interface through Brownian motion, or small flows within the sample.
- Eventually, the particle approaches the interface close enough that it can breach (likely due to thermal fluctuations as shown by Aarts et. al, [2]). This moment is defined as zero time ($t = 0$). After this point, the particle begins moving towards its equilibrium position straddling the interface. The velocity of this motion is of much interest when seeking to understand the dynamics, and is well captured by this technique.
- Due to the low surface tension of the water/water system, the initial acceleration is much slower than in an oil/water system, wherein the acceleration of the particle is not observable even with sub-millisecond time resolution. For large particles it is therefore visible, as in Figure 10.1.
- The particle rapidly reaches its maximum speed nonetheless, and completes the majority of its motion very quickly, in a process named 'snap-in'.
- As the particle begins to approach equilibrium, capillary forces driving motion lessen. At lower speeds more complex behaviours may begin to play a role (as discussed in Section

3.1.3), slowing the motion further. Relaxation to equilibrium can thus be unexpectedly slow. This part of the motion is also of great interest as relaxation dynamics can be quite different to snap-in dynamics [21, 62]. However, the measurement uncertainty of this technique becomes more significant close to equilibrium due to the increasing contribution of horizontal and vertical drift in the sample, so the relaxation is tracked for only seconds to tens of seconds.

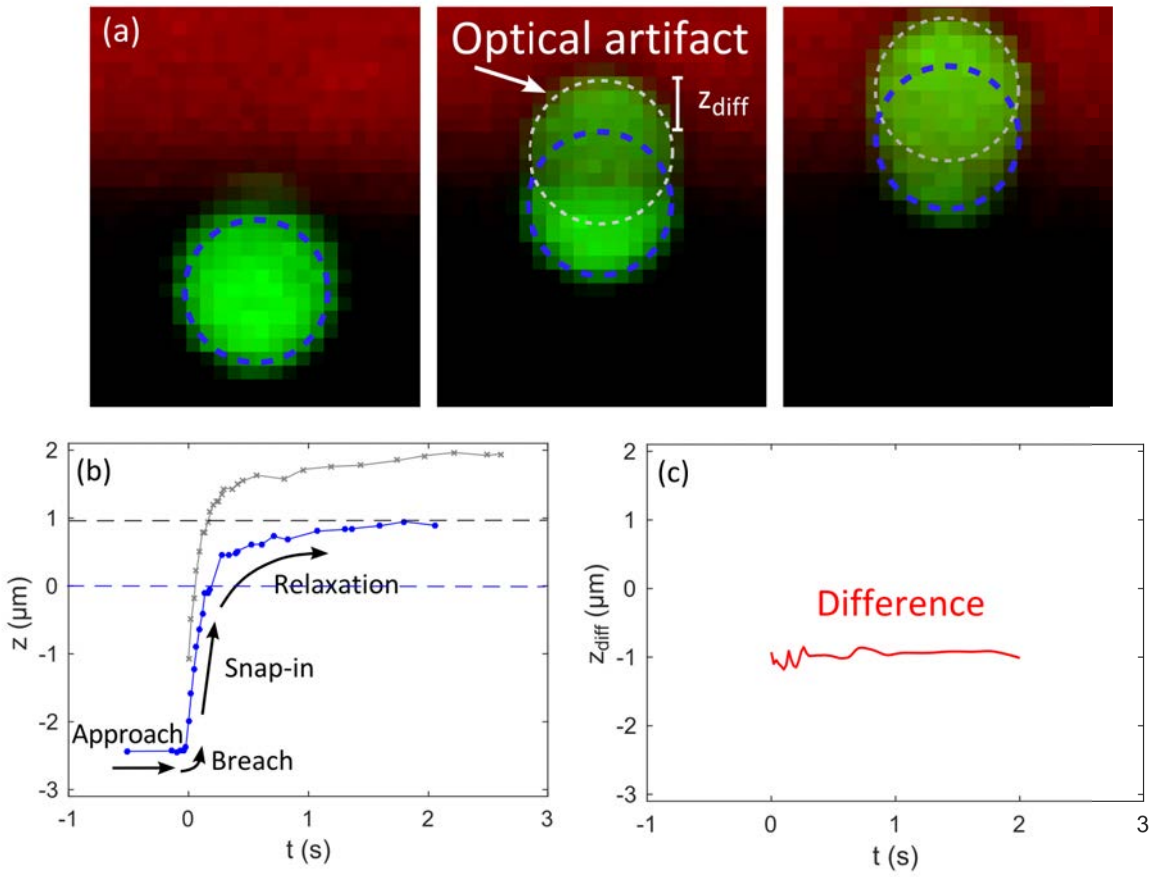

Figure 10.1: Example of confocal microscopy tracking of an adsorption of a 4.5 µm Sulphate latex particle to an 8%/8% dextran / fish gelatin interface. (a) 8 µm × 10 µm Frames from confocal microscope. Fluorescein-labelled particle shown in green, and the fish-gelatin-rich phase is labelled red with Rhodamine B. Time of images from moment of breach: 0 s, 0.61 s and 1.03 s. In frames 2 and 3, two particle images can be seen, due to a lensing effect elsewhere in the sample. Either image can be tracked. (b): results of particle tracking, z representing the distance of the blue particle centre from the interface. Uncertainty in measurement approximately 0.15 µm. Blue trajectory tracked from lower particle image outlined in blue, grey trajectory upper image outlined in grey. Upper and lower dashed lines correspond to interface positions for upper and lower particles, respectively. (c) Difference, z_{diff} between upper and lower particle positions from tracking. No trends is observed and noise is the same size as measurement uncertainty. Either image can therefore be tracked.

The water/water interface is a complex system, though through the variation of different factors we can gain insight into the relative contributions of different aspects of the system. Firstly, the influence of particle size was examined. The scaling of dynamics with particle size can give insight into the relative contributions of different forces (for instance, some such as Stokes drag and line

tension, scale with the particle radius ($\propto R$) and some, such as surface tension, with the particle surface area ($\propto R^2$)). Particles with diameters of 0.2 µm, 1 µm, 4 µm and 10 µm were tracked. The 4 µm and 10 µm particles were rather polydisperse, however this is advantageous as the diameter can be measured during the adsorption tracking process, providing additional particle size datapoints.

Second, the influence of the concentrations of the polymer solutions was investigated. In a polymer/polymer ATPS, both the surface tension and the viscosity scale in a well established way with polymer concentration. Systems with 10% / 10% fish gelatin / dextran and 8% / 8% fish gelatin / dextran concentration were investigated.

Thirdly, the addition of salt to the fish gelatin / dextran system results in the purification of the phases, ie. the small quantity of fish gelatin diffusing the dextran-rich phase is reduced or removed, and vice-versa. There will also be a small influence upon the electrostatic interactions between particle and interface, though this effect is very short-range. The initial effective salt concentration of a solution of 10% / 10% fish gelatin / dextran is 20mM due to the polyelectrolyte (fish gelatin). This was raised to 85mM to study the influence of salt.

Finally, the influence of particle surface chemistry was investigated. Sulphate, Carboxylate and Amine-coated latex particles were tracked.

10.1.2 Effect of particle size

Here the adsorption of the three particle sizes so far introduced, (1 µm, 4 µm and 10 µm) are compared in the 10% / 10% dextran / fish gelatin system. Figure 10.2a shows the resulting adsorptions. It is clear that larger particles have slower dynamics. Figure 10.2b helps show the scaling of this effect, as it shows the movement of each particle rescaled by its radius, as individually measured with confocal microscopy in the case of the polydisperse larger particles. The time axis also is rescaled with the particle radius, as in many models (discussed in Section 10.2) dynamics scale in this way. As is evident from Figure 10.2b, there is some effective collapse of the trajectories to a single curve, especially at shorter times during snap-in. However as particle size increases, the dynamics of the relaxation phase slow down, and the chances of reaching equilibrium contact angle within the experimental timeframe are also apparently diminished.

0.2 µm particles were also observed adsorbing to the interface, however the experimental errors of the optical microscopy technique were larger than the observed motion, so this data is not presented.

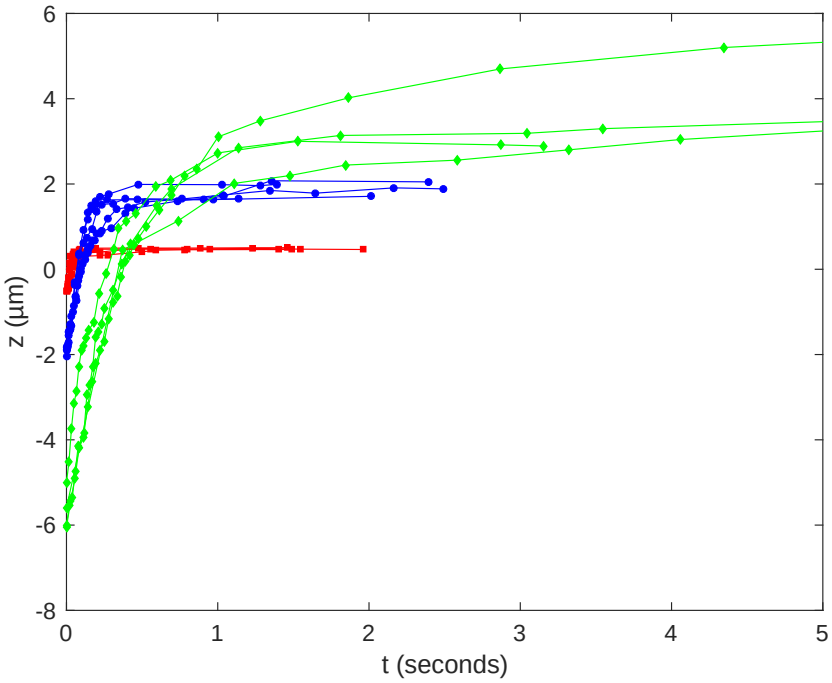

(a) Sulphate latex particles of size 1 µm (red squares), 4 µm (blue circles), and 10 µm (green diamonds) adsorbing to the interface of a 10% / 10% dextran / fish gelatin system.

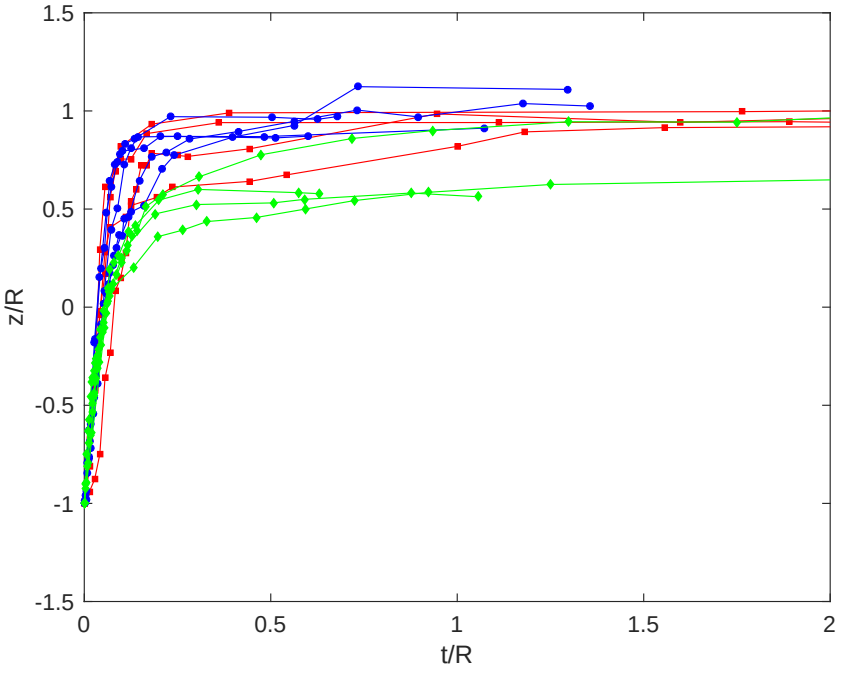

(b) Reproduction of Figure 10.2a, with each axis rescaled by the particle radius.

Figure 10.2: Influence of particle size. (b) shows the data rescaled for particle size. The data collapse with reasonable accuracy during initial snap-in motion, but closer to equilibrium larger particles slow down more rapidly.

10.1.3 Effect of polymer concentration

The concentration of polymer solution controls both the viscosity and the surface tension of the system. The polymer concentrations of 10%/10% and 8%/8% dextran / fish gelatin were chosen to provide high viscosity, which helps reduce flows within the sample and provide a well-defined interface. The viscosity and surface tension values were measured and calculated respectively as described in Section 7.4, and are provided again in Table 10.1:

Table 10.1: Table of polymer systems. Effective salt concentration measured through conductivity measurements, and adjusted with addition of NaCl. 'Polymer Concentration' refers to the initial state point, not the resulting phase diagram positions.

Initial Concentration (Fish Gelatin / Dextran)	(Effective) Salt Concentration	Dextran-rich phase viscosity	Fish-gel.-rich phase viscosity	Surface Tension
10 wt% / 10 wt%	20 mM	0.045 Pa s	0.554 Pa s	103.5 mN/m
8 wt% / 8 wt%	20 mM	0.027 Pa s	0.155 Pa s	45.6 mN/m
10 wt% / 10 wt%	85 mM	0.047 Pa s	0.515 Pa s	115.2 mN/m

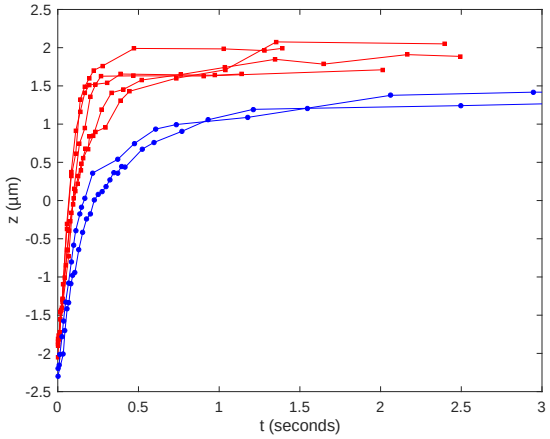

(a) 4 µm Sulphate latex particles adsorbing to a dextran-gelatin interface. Red squares: 10% / 10% fish gelatin / dextran . Blue circles: 8%/8% fish gelatin / dextran.

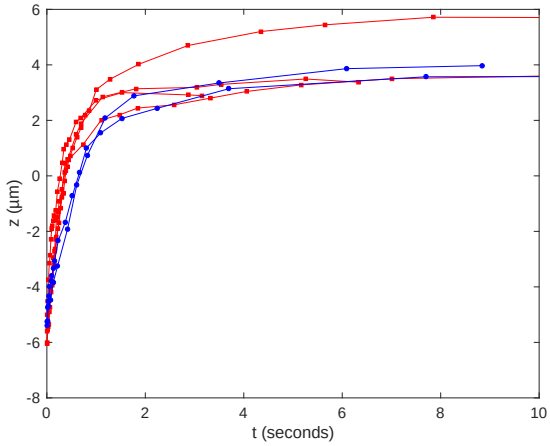

(b) 10 µm Sulphate latex particles adsorbing to a dextran-gelatin interface. Red squares: 10% / 10% fish gelatin / dextran . Blue circles: 8%/8% fish gelatin / dextran.

Figure 10.3: Influence of polymer concentration upon adsorption. Lowering the concentration of polymer results in slower adsorption, with a larger resulting contact angle.

The trajectories of a 4 µm sulphate latex particle in the 10% / 10% dextran / fish gelatin system and the 8% / 8% dextran / fish gelatin system are compared in Figure 10.3a, and for particles with a mean diameter of 10 µm in Figure 10.3b. In each case, the lower polymer concentration results in a slightly slower snap-in and slower relaxation, though this is small compared to experimental error. The low concentration also has an apparently higher contact angle (measured from the fish gelatin phase). This difference may not be significant.

10.1.4 Effect of salt concentration

As previously discussed, the addition of salt purifies each phase. As surface tension scales with the difference in polymer concentration between the phases, this is influenced too by salt. Viscosity is

also affected as the interactions between neighbouring polymers are changed. Table 10.1 shows the resulting change in surface tension and viscosity.

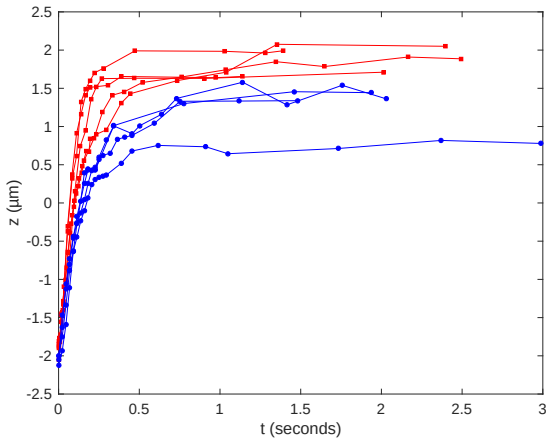

(a) 4 µm Sulphate latex particles adsorbing to a dextran-gelatin interface. Red squares: 20 mmol salt concentration (as stock). Blue circles: 85 mmol salt concentration.

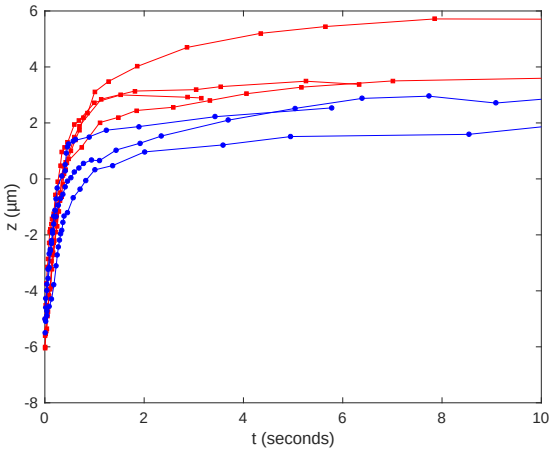

(b) 10 µm Sulphate latex particles adsorbing to a dextran-gelatin interface. Red squares: 20mM salt concentration (as stock). Blue circles: 85mM salt concentration.

Figure 10.4: Influence of salt concentration. Raising the salt concentration increases surface tension, but also fish gelatin phase viscosity. Resulting equilibrium contact angle is larger, but motion is slower.

However, as shown in Section 8.3, salt-induced purification also affects the extend of fish gelatin adsorption to the particles, as without salt diffusing fish gelatin adsorbs onto the particle surfaces. Therefore there will also be some difference in wetting properties between the case with salt and without.

Figures 10.4a and 10.4b show the adsorption of 4 µm Sulphate latex and 10 µm Sulphate latex particles respectively, for a salt concentration of 20 mM and 85 mM. In the higher salt case, the snap-in dynamics are slightly slower, the equilibrium contact angle appears larger as is expected from an increase in surface tension. The relaxation dynamics are also somewhat slowed, but not as much as in the 8% / 8% dextran / fish gelatin case. In this case too though the difference is not much larger than experimental error.

10.1.5 Effect of particle surface chemistry

In attempting to stabilise water-water systems with particles, the surface chemistry could be assumed to play a role in determining particle behaviour and interaction with the polymer phases. 1 µm Sulphate, Carboxylate and Amine-coated latex particles were therefore observed adsorbing to the 10% / 10% dextran / fish gelatin interface. The results are shown in Figure 10.5.

However, within experimental errors and particle polydispersity, no influence of surface chemistry can be seen. This may be due to the adsorption of fish gelatin to the surfaces, driven by the hydrophobic interaction, which may then dominate further interactions with the polymer phases.

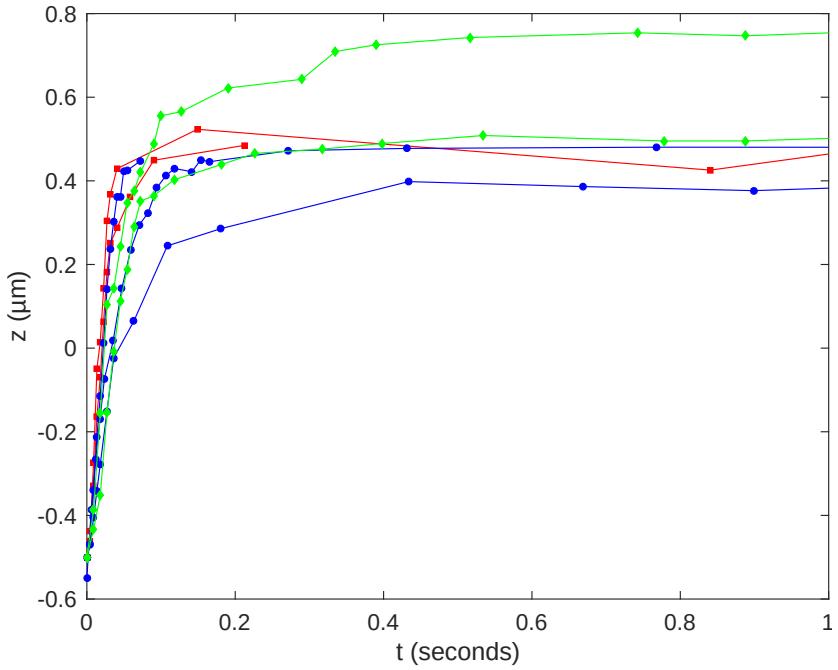

Figure 10.5: Influence of particle surface chemistry upon adsorption to the dextran-gelatin interface in a 10% / 10% dextran / fish gelatin system. Red squares: 1 µm Carboxylate latex particles. Blue circles: 1 µm Sulphate latex particles. Green diamonds: 1 µm Amine latex particles. No influence of surface chemistry is seen within experimental errors.

10.1.6 Effect of phase purity

As discussed in Section 7.4, although the system begins with two phases each of exactly 20% fish gelatin or 20% dextran, this is not in fact the equilibrium phase diagram position for this total polymer concentration. Some polymer will diffuse into each opposing phase, and a small quantity of water will move from the fish gelatin phase to the dextran phase, due to the greater preference for water of the dextran phase.

This is expected to happen very quickly upon meeting of the two drops, and will equilibration will occur first of all at the interface, which is the region we are interested in. However, to ensure that beginning with pure phases does not influence the observed trajectories, two droplets were isolated from the equilibrated phases of a separated emulsion, using the method described in Section 7.2.1. Trajectories for 4 µm Sulphate latex particles dispersed in the dextran-rich phase of this system are compared to the same particles dispersed in pure 20% dextran in Figure 10.6. No difference is observed in particle trajectories.

Particles smaller than 4 µm were difficult or impossible to observe adsorbing in the equilibrated phase system, as the adsorption-driven spontaneous aggregation of particles discussed in Section 8.3 occurred on very fast timescales of a few minutes. After this point all particles were aggregated. For this reason, pure phases were used in all other experiments.

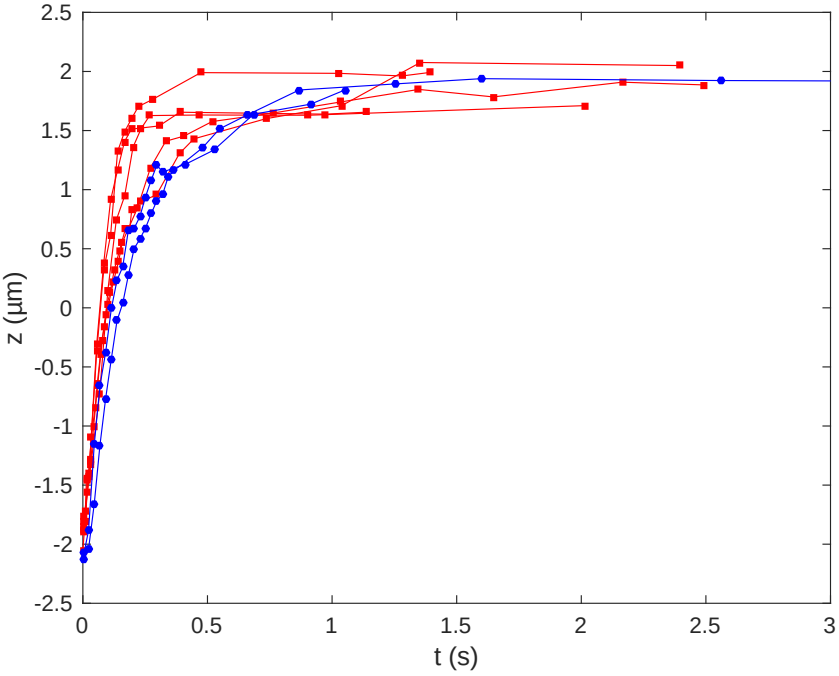

Figure 10.6: Influence of initial phase purity upon adsorption of 4 µm Sulphate latex particles to the dextran-gelatin interface in a 10% / 10% dextran / fish gelatin system. Red squares: pure phases. Blue circles: thermodynamically equilibrated phases. No influence of initial phase purity is seen within experimental errors.

10.2 Comparing trajectories to models

10.2.1 Capillarity vs. Viscous Drag model

This model, discussed in Section 3.1.3.2, assumes that the forces experienced by the particle can be approximated as simply the balance between the pull of surface tension as the contact line seeks its equilibrium contact angle, and a drag force, eg. Stokes drag. The solution to this force balance, neglecting small inertial contributions, is an exponential function given by Equation 3.6 reproduced here as Equation 10.1:

$$z(t) = z_E - \Delta z \exp(-t/T_D) \tag{10.1}$$

where z_E is the equilibrium height, and Δz the total distance moved by the particle. T_D is the characteristic time of this model, given by:

$$T_D = \frac{\xi}{K} \tag{10.2}$$

where ξ is the viscous drag term which scales between the two phase viscosities: $\xi \propto 2/D(-z\mu_{\text{dex}}/2 + z\mu_{\text{f.gel}}/2)$. For a Stokes drag,

$$\xi = 3\pi D\mu(z). \tag{10.3}$$

The capillary force is analogous to a spring, with constant $K = 2\pi\gamma$, where the factor 2π remains from integrating the contact line force around the particle circumference. This model was fitted to the data, allowing T_D to vary. The success of fitting an exponential curve to the data is best illustrated using a semilog plot, in which time is plotted against the logarithm of the distance from equilibrium. Exponential decay behaviour then presents as a straight line. An example plot for 1 µm, 4 µm and 10 µm Sulphate latex in the 10% / 10% fish gelatin / dextran system is shown in Figure 10.7, and the resulting time constants T_D are shown in Table 10.2.

Table 10.2: Exponential decay time constants T_D for various particle sizes adsorbing to the interface of a 10% / 10% fish gelatin / dextran , as measured from particle trajectories using Equation 10.1, and as calculated using Equations 10.2 and 10.3.

D	T_D Measured	T_D Calculated
1 µm	$0.01 - 0.03$	0.004
4 µm	$0.13 - 0.16$	0.017
10 µm	$0.5 - 0.7$	0.050

It can be seen that the fit is good for the first 0.2 s for the 1 µm particle, 0.4 s for the 4 µm particle, and up to 2 s for the 10 µm. For larger times, the adsorption dynamics become much slower. This is consistent with the very long relaxation to equilibrium of particles at the oil/water interface, observed by Kaz et al. [62]. This can be explained by pinning of the contact line on surface defects, which will be explored in Section 10.2.2.

Moreover, surprisingly the TD that we measure are consistently at least one order of magnitude larger than those calculated, though they scale with the particle radius in the expected way. We will return to this in Section 10.2.2.2, and propose some hypotheses in the discussion (Section 10.3).

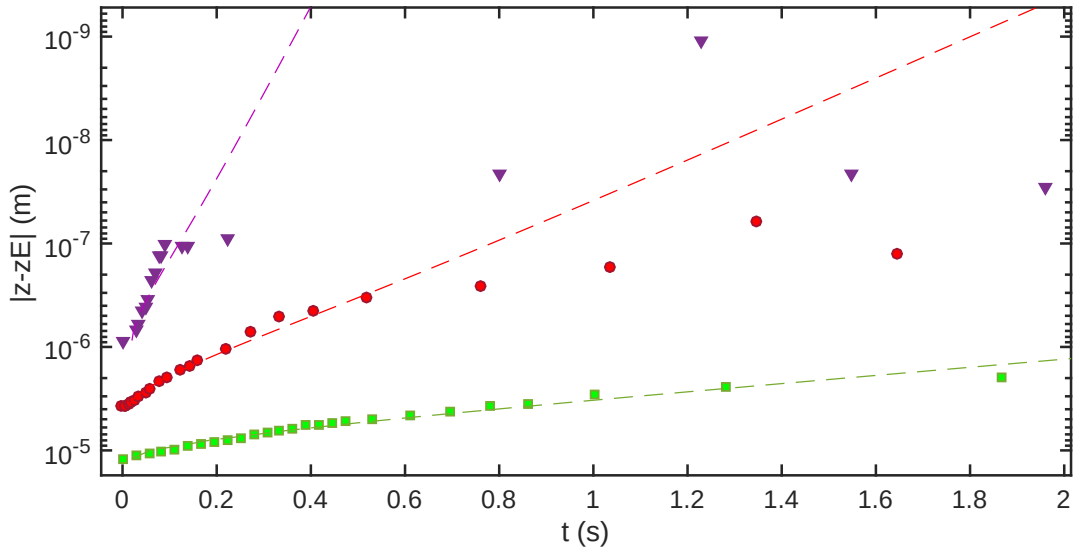

Figure 10.7: Trajectories of adsorption of Sulphate latex particles (points), normalised by particle size. Purple triangles, red circles and green squares represent 1 µm, 4 µm and 10 µm particles respectively. Dashed lines represent fits to Equation 10.1, which applies to the early times in the trajectory.

10.2.2 Contact Line Hopping Models

To account for the slow relaxation dynamics captured at the oil/water interface by Kaz et al., Colosqui et al [21]. propose a model based on forward and backward hopping of a contact line over a series of defects, as introduced in 3.1.3.2. In this model, the snap-in dynamics are characterised by an exponential behaviour before a crossover point, after which a logarithmic behaviour is observed. This logarithmic relaxation is represented by Equation 3.12, reproduced here as Equation 10.4.

$$\langle z \rangle = z_E + L_H \log \frac{1 + A_H \exp(-t/T_H)}{1 - A_H \exp(-t/T_H)} \tag{10.4}$$

In this equation, the characteristic hop length L_H is given by $L_H = \frac{2k_BT}{Kl}$, the trajectory amplitude A_H by $A_H = \tanh \frac{1}{2}\Delta z/L_H$ and the characteristic hop time T_H by:

$$T_H = T_D \left(\frac{L_H}{l}\right) \frac{2\pi}{\sqrt{|\Phi^2 - 1|}} \exp\left(\frac{\Delta U}{k_BT} + \frac{1}{4}\frac{l}{L_H}\right) \tag{10.5}$$

where Φ is given by $\pi\Delta U/\gamma l^2$. The exponential decay time T_D, discussed in the previous section, is featured in this hop time. There are two unknown fitting parameters for this model, both relate to the surface of the particle. The first is ΔU, which represents the energy required to overcome a defect on the particle surface, which scales with the surface tension γ and the defect area A_d:

$$\Delta U \propto \gamma A_d \tag{10.6}$$

The second is l, which represents the mean distance the contact line moves before being pinned by a defect somewhere on the particle. This distance is given by:

$$l = \frac{A_d}{2\pi R} \tag{10.7}$$

In their paper introducing this model, Colosqui et al. verify it through fitting to the experimental data of Kaz et al. Imposing a energy barrier $\Delta U = 15 - 30 k_B T$, they obtain $l \sim 0.5 - 1 \times 10^{-12}$m, corresponding to a defect area A_d of $\sim 3\,\mathrm{nm}^2$, and a characteristic hopping time T_H of $\sim 10^3$s. However, in their paper the authors do not show the fit graphically, do not discuss the sensitivity of the fit to the fitting parameters, and do not explicitly write the T_D used.

Our goal in the following sections is to use this model to fit our data (Section 10.2.2.3). But first, we explore the influence of the parameters involved on the particle dynamics predicted by the model (Section 10.2.2.1), and revisit the fitting of the experimental data of Kaz et al to gain more confidence in the fitting procedure (Section 10.2.2.2).

10.2.2.1 Influence of surface tension, exponential decay time and particle radius

Influence of surface tension

To explore the influence of surface tension to the model, we choose other parameters that are similar to those in the experiments of Kaz et al., ie. a 1.8 µm particle adsorbing to an interface, with equilibrium contact angle set at 70° measured inside the oil phase. The surface tension is varied from the oil/water value of $\gamma = 40\,\mathrm{mN/m}$, down to that observed in our water/water system at $\sim 100\,\mu\mathrm{N/m}$.

In varying the surface tension, the typical decay time T_D varies. For a $\sim 1\,\mu$m particle adsorbing to the oil/water interface T_D is expected to be $\sim 0.1\,\mu$s [21]. This, from Equation 10.2 gives a drag coefficient ξ of $10^{-7} \times 0.04$ kg s^{-1}, which is then used to calculate new values of T_D as the surface tension changes.

Additionally, the energy ΔU for the contact line to pass over a defect will decrease with decreasing surface tension. We must choose a value for the area of a defect A_d, which is set at $10\,\mathrm{nm}^2$ as was measured for Sulphate latex particles from the experimental data of Kaz et al. by Rahmani et al. [62, 90]. We then vary the surface tension between 40 mN/m and 0.1 mN/m, picking an initial value for ΔU as $27 k_B T$. The influence of surface tension on the model for these parameters is then shown in Figure 10.8.

As the surface tension is reduced, the logarithmic regime disappears. We observe then only the fast exponential regime. This is due in part to the dependency of ΔU upon the surface tension - for low γ, dU becomes of the same order as $k_B T$ and can no longer pin the interface if other parameters remain the same.

Influence of particle radius

Figure 10.9a shows the influence of particle size upon trajectories that we obtain using Colosqui's model (Equation 10.4) for particles of diameter 1 µm, 1.8 µm, 4 µm and 10 µm. Surface tension of 40 mN/m was used, and viscous drag parameter ξ was scaled with R as $\xi = 0.01R$, typical for measurements at the oil/water interface.

The effect of increasing particle radius is to enlarge the trajectories in z, and delay the relaxation to equilibrium. The initial separation from equilibrium Δz increases for larger particles, and though

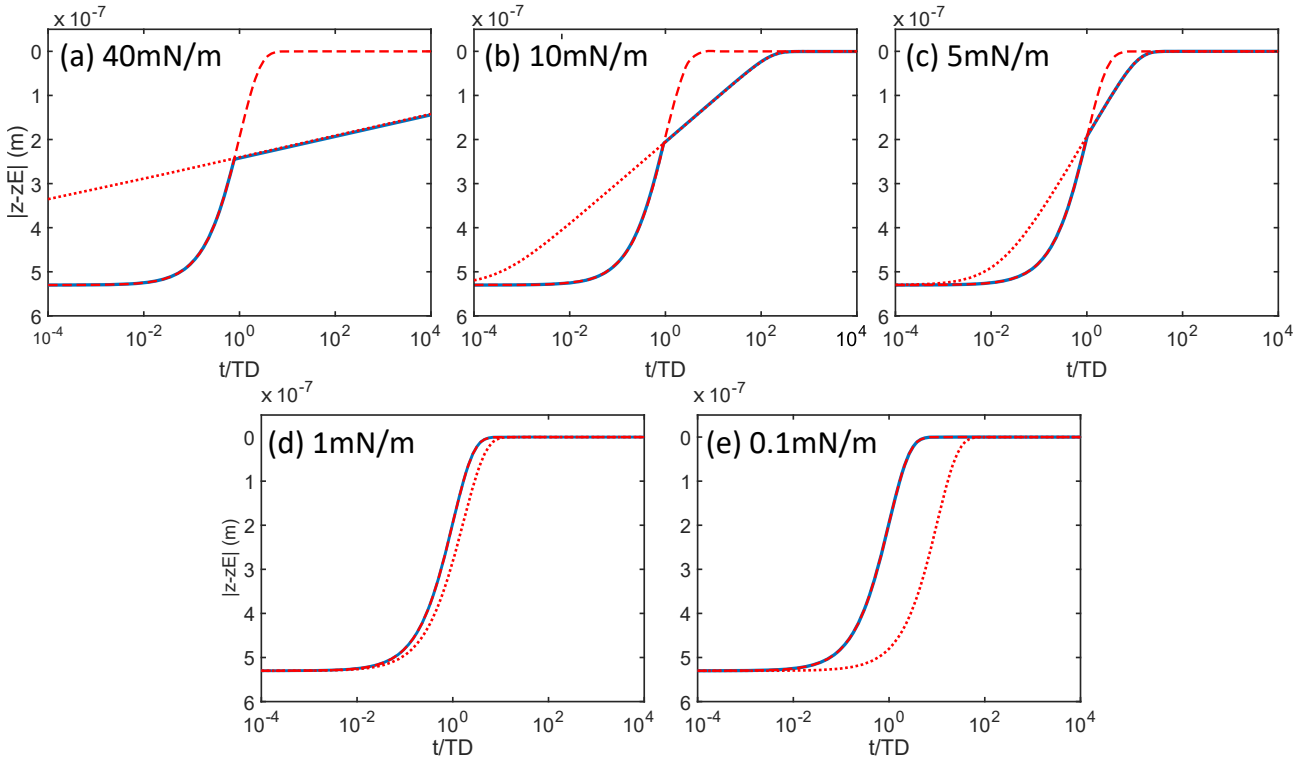

Figure 10.8: Logarithmic regime (dotted red lines), provided by Equation 10.4, and exponential regime (dashed red lines) from Equation 10.1 for a variety of surface tension values, with the resulting particle trajectory indicated by the solid blue lines. Time axis is rescaled by exponential time T_D for purpose of comparison. $\gamma = 40\,\mathrm{mN\,m^{-1}}$, $10\,\mathrm{mN\,m^{-1}}$, $5\,\mathrm{mN\,m^{-1}}$, $1\,\mathrm{mN\,m^{-1}}$ and $0.1\,\mathrm{mN\,m^{-1}}$ represented by a, b, c, d and e respectively.

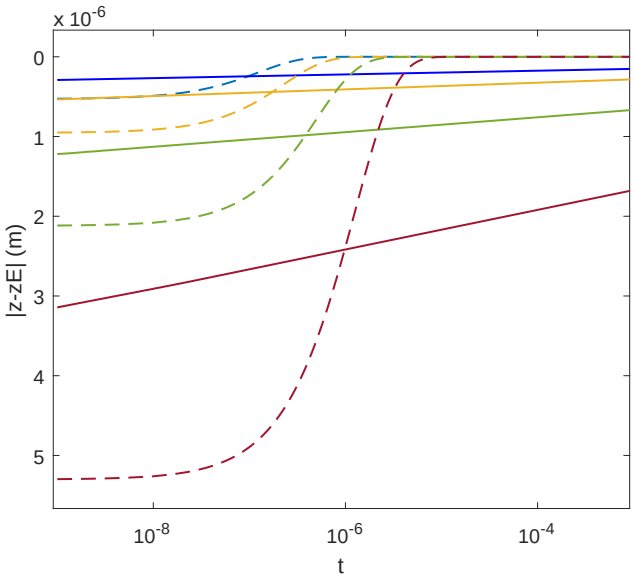

(a) Influence of size upon adsorption trajectories, given by Equations 10.1 (dashed lines) and 10.4 (solid lines). Plots increase in size from top to bottom, with diameters 1 µm, 1.8 µm,4 µm and 10 µm being represented by blue, yellow, green and red lines respectively

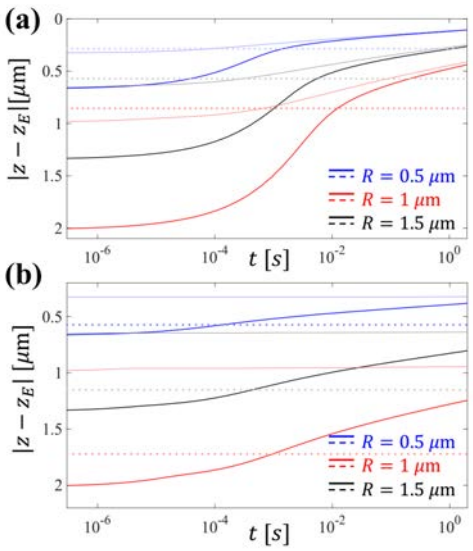

(b) Top: Theoretical Carboxylate particle trajectories, Bottom: Sulphate particle trajectories, from [90]. Dotted lines represent height of crossover from exponential to logarithmic regime.

Figure 10.9: Influence of size upon logarithmic adsorption trajectory model.

the gradient of the logarithmic regime also increases (meaning a greater particle velocity), this increase is not sufficient to prevent delaying reaching equilibrium.

From the same group as Colosqui et al., Rahmani et al. obtain exactly the same trend for smaller particles using their more advanced model, as shown in Figure 10.9b, reproduced from [90].

Influence of viscous drag coefficient ξ

The role of the viscous drag coefficient ξ is solely to determine the exponential decay time T_D. The value used to approximate Kaz et al.'s experimental data is, as mentioned above, $4 \times 10^{-9}\mathrm{kg\,s^{-1}}$. In our water/water system, R can be up to 1 order of magnitude larger than the particles used by Kaz et al., and the liquid viscosity 2 orders of magnitude larger, so overall ξ could be 3 orders of magnitude larger. The influence of ξ increased up to 3 orders of magnitude is shown in Figure 10.10. The effect of ξ is simply to shift the curves in time.

10.2.2.2 Fitting the Colosqui model to the data of Kaz et al.

In Section 10.2.1, we show that the snap-in dynamics can be modelled with an exponential relaxation (Equation 10.1), though the characteristic time T_D is an order of magnitude larger than that predicted by Stokes. In the present section, we aim to determine which T_D can be obtained from the experimental data of Kaz et al, and compare this to Stokes. To do this, we notice that T_D features in Equation 3.15 for the characteristic hopping time, which is determined by parameters ΔU and l, which can be obtained through a fit to the data.

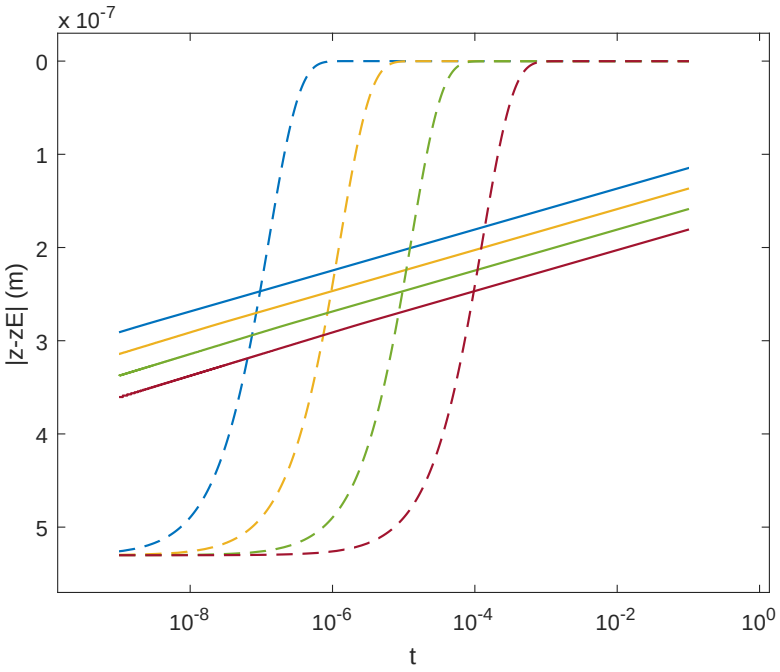

Figure 10.10: The influence of viscous drag term ξ upon particle trajectories given by Equation 10.4 (solid lines). Initial exponential behaviour given by Equation 10.1 (dashed lines). ξ values shown, from left to right, 4×10^{-9}, 4×10^{-8}, 4×10^{-7}, 4×10^{-6}kg s^{-1}.

In Figure 10.11, we reproduce the data for a 1.8 µm Sulphate particle at the oil/water interface from Figure 3.7, reproduced from Ref [62] (black circles). A fit to Equation 10.4 is shown as the dotted line, with fitting parameters taken from Colosqui et al. as $\Delta U = 27 k_B T$ and $l = 5.0 \times 10^{-13}$ m, corresponding to $A_d \approx 3\,\mathrm{nm}^2$. Additionally, a T_H of $\sim 10^3$s is provided by the authors, which then corresponds to a T_D of 0.1 µs. This is smaller than the Stokes value of 0.7 µs.

As these values of ΔU and l give an entirely logarithmic trajectory, the fit is not very sensitive to T_D compared to ΔU and l, so this fitting cannot tell us whether their T_D is anomalous or not.

At the oil/water interface, T_D values are likely too small to ever be experimentally observed by particle tracking techniques. However in our case, both regimes can be observed. The next section applies the model of Colosqui et al. to our data.

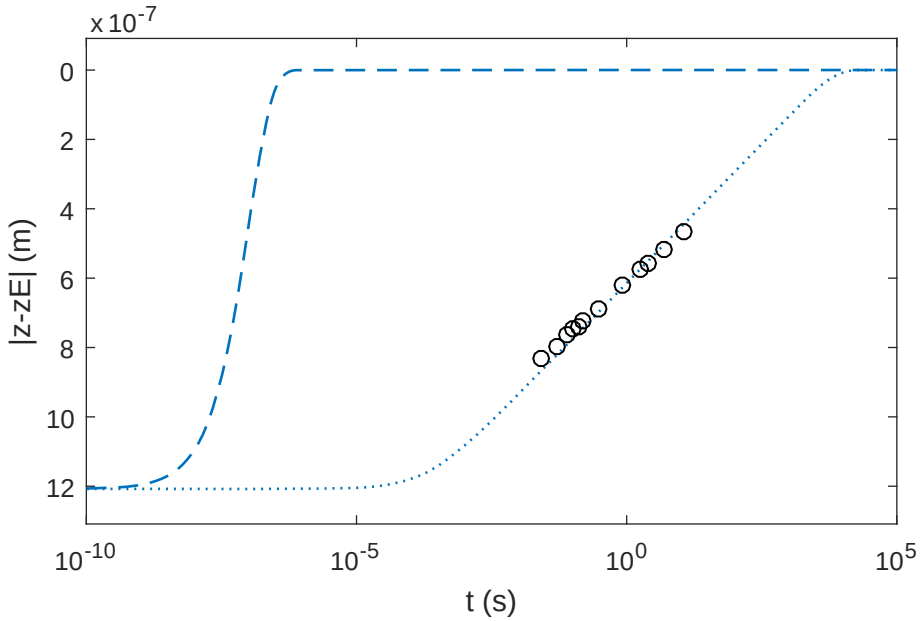

Figure 10.11: Fitting of Equation 10.4 (dotted line) to the data of Kaz et al. tracking the adsorption of a 1.8 µm diameter Sulphate latex particle (black circles, from Figure 3a of Reference [62]), using parameters specified in [21]. The exponential regime, given by Equation 10.1 is shown as the dashed line, however only logarithmic behaviour is observed in this trajectory.

10.2.2.3 Fitting the Colosqui model to our data

In this section, we will fit the Colosqui model to the dynamics of relaxation close to equilibrium, given by Equation 10.4. The initial 'snap-in' dynamics with exponential behaviour will still be fitted to an exponential as above, given by Equation 10.1.

The influence of particle radius, polymer concentration and salt concentration upon the model is explored. The fitting parameters of the model, ΔU and $A_d = 2\pi Rl$ are reported. As these are surface properties, little influence of the solution properties or particle size is expected.

Additionally, the model requires as a parameter the exponential decay time T_D. Given the assumption that the particles follow this behaviour for the initial part of their motion (ie. the snap-in), T_D is calculated through a fit to this initial exponential curve.

Influence of particle size

Figure 10.12 shows a sample trajectory and fit for particles with diameter 1 µm, 4 µm and - due to polydispersity within the '10 µm' particles - 12 µm. In each case, a crossover is observed from the exponential curve to the logarithmic. The values of the surface parameters ΔU and A_d from these fits, as well as the measured exponential decay time T_D are shown in Table 10.3. The ranges reflect multiple tracked particles. The spread of results is not unexpected, as large variation in trajectories can be seen also at the oil/water interface (see Figures 1d & 3b of Ref [62]). The ranges observed in ΔU and A_d overlap well for each particle size as should be expected for particles with the same surface characteristics. This agreement is an indication that surface effects truly play a role in the relaxation of the particles.

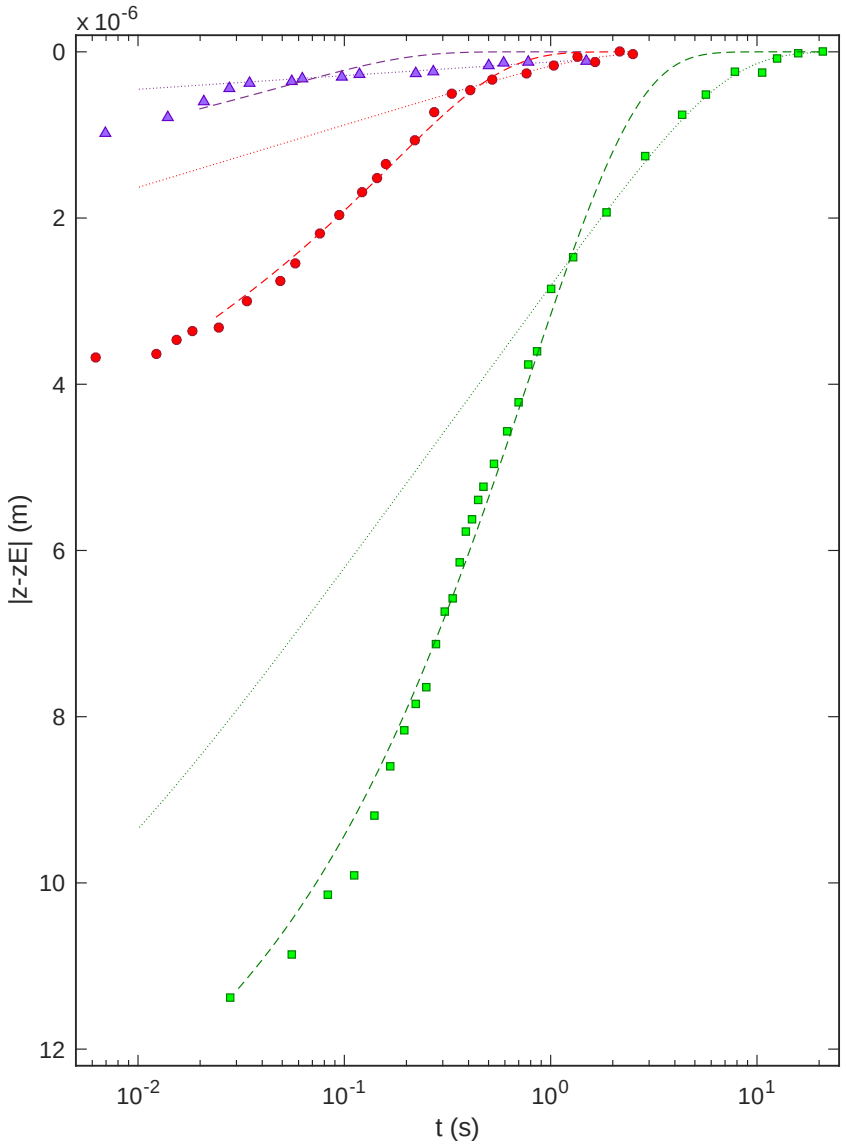

Figure 10.12: Fitting of Equations 10.4 (dotted lines) and 10.1 (dashed lines) for 1 µm, 4 µm and 12 µm Sulphate Latex particles adsorbing to the dextran / fish gelatin interface, shown by purple triangles, Red circles and green squares respectively.

Table 10.3: Fitting parameters of Equations 10.4 and 10.1 for 1 µm, 4 µm and 10 µm Sulphate Latex particles adsorbing to the dextran / fish gelatin interface.

	1 µm	4 µm	10 µm
$\Delta U(k_{\mathrm{B}}T)$	$1-4$	$1-3$	$2-5$
A_d nm^2	$350-550$	$200-500$	$300-700$
T_D s	$0.01-0.03$	$0.13-0.16$	$0.5-0.7$

The low values of ΔU observed, in the range $1-4k_{\mathrm{B}}T$, are consistent with the very low surface tension of this system. The A_d values are almost two orders of magnitude larger than those measured for the oil/water interface. Strikingly, the square root of A_d, representing the width of a defect, is in the range $14-22$ nm, which is around double the radius of gyration of the polymers, $2R_g \sim 20$ nm.

This introduction of the polymer lengthscale could be explained in many different ways. We know from Section 8.2 that gelatin adsorbs onto the surfaces of the latex particles. One possibility is that gelatin adsorbs from the dextran-rich phase, and pins the contact line. Alternatively, the gelatin adsorption could occur at the contact line, as the particle enters the fish gelatin rich phase, causing pinning (illustrated in Figure 10.15). To investigate these possibilities we added salt, as higher salt concentration purifies the phases so would remove the gelatin in the dextran-rich phase.

Influence of salt

In the low-salt system, some fish gelatin diffuses in the dextran phase, and adsorbs onto the particle surfaces (demonstrated in Section 8.2). Upon the addition of salt, this diffusing fish gelatin within the dextran-rich phase is removed. This may have an influence on relaxation dynamics if the adsorption of fish gelatin plays a role in interface pinning.

Figure 10.13 compares the relaxation dynamics of 4 µm Sulphate latex particles in the stock salt concentration of 20mM to those with 85mM salt concentration. Table 10.4 gives the fitting parameters for each system for several tracking trajectories.

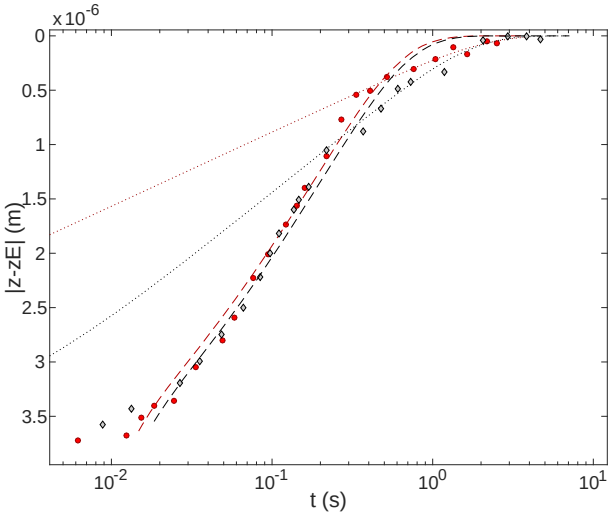

Figure 10.13: Influence of salt concentration. Fitting of Equations 10.4 (dotted lines) and 10.1 (dashed lines) for 4 µm Sulphate Latex particles adsorbing to the dextran / fish gelatin interface. Red circles show stock salt concentration of 20mM, blue squares 85mM salt.

The parameters of the fits match very closely, excepting a small increase in ΔU, which is

Table 10.4: Fitting parameters of Equations 10.4 and 10.1 for 4 µm Sulphate Latex particles adsorbing to the dextran / fish gelatin interface, with and without added salt.

Salt concentration:	20mM	85mM
$\Delta U(k_\mathrm{B}T)$	$1-3$	$2.5-4$
A_d nm^2	$200-500$	$200-500$
T_D s	$0.13-0.16$	$0.16-0.19$

Table 10.5: Fitting parameters of Equations 10.4 and 10.1 for 4 µm Sulphate Latex particles adsorbing to the dextran / fish gelatin interface at different polymer concentrations.

	8%/8%	10%/10%
$\Delta U(k_\mathrm{B}T)$	$1-2$	$1-3$
A_d nm^2	$600-800$	$200-500$
T_D s	$0.19-0.24$	$0.13-0.16$

expected due to the increased surface tension. As Figure 10.13 shows, the increased viscosity of the fish gelatin phase with added salt leads to a small increase in T_D, moving the curves to the right. There may also be a small difference in z_C, the crossover height from exponential to logarithmic behaviour.

Influence of polymer concentration

Reducing polymer concentration affects both the surface tension and the viscosity to a similar degree, resulting in largely similar dynamics, as shown in Figure 10.14. The energy per defect ΔU shown in Table 10.5 is reduced slightly for the 8% / 8% fish gelatin / dextran system due to the lower surface tension. The A_d observed is larger for the lower concentration.

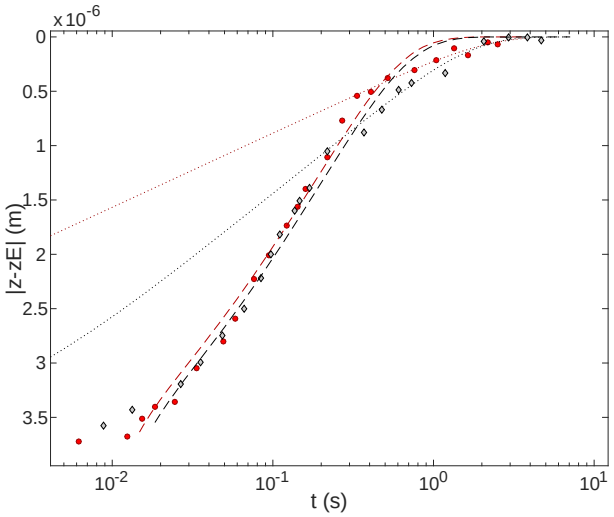

Figure 10.14: Influence of polymer concentration. Fitting of Equations 10.4 (dotted lines) and 10.1 (dashed lines) for 4 µm Sulphate Latex particles adsorbing to the dextran / fish gelatin interface. Red circles show 10% / 10% fish gelatin / dextran , grey diamonds show 8% / 8% fish gelatin / dextran .

10.3 Discussion

To summarise our data for particle trajectories, we find two unexpected features: at short times we observe an exponential regime with a characteristic time T_D, though the T_D we measure is an order of magnitude larger than the one predicted by equilibrating the capillary force with viscous drag force given by Stokes. At longer times, we observe a slower logarithmic regime, delaying the relaxation to equilibrium.

Considering first this slow logarithmic relaxation, this is similar to recently published experimental and theoretical studies, and is typical of contact line pinning by defects on the particle surface. This is unexpected - in our low surface tension system we do not expect any pinning of the contact line. According to literature models, this indicates that the size of the defects has to be much larger than in the standard case of studies at the oil/water interface. By fitting our data to Colesqui's model from the literature, we find defect areas of the order of $400\,\mathrm{nm}^2$, corresponding to a typical size of the order of 20 nm. Strikingly the size is of the order of magnitude of a polymer molecule. Scanning electron microscopy images (Figure 7.1), with resolution down to 10 nm, should be able to see physical defects on the particle surface of this lengthscale, and none are visible. This further suggests the influence of polymers in pinning.

Additionally, we know from Zeta Potential and Total Organic Carbon measurements that gelatin adsorbs on the latex particles, even in the presence of dextran. We therefore hypothesise that the adsorption of gelatin on the particles pins the contact line.

Further results show that the salt concentration does not influence the trajectory significantly, neither does the surface chemistry or the polymer concentration. At high salt concentration, there is no gelatin in the dextran rich phase. Therefore we suggest that gelatin from the gelatin-rich phase adsorbs at the contact line, pinning it in place. This hypothesis is illustrated in Figure 10.15.

A somewhat conflicting result is the difference in relaxation trajectory upon reducing the polymer concentration. For the 8% / 8% fish gelatin / dextran system, the defect area measured of the order of $700\,\mathrm{nm}^2$, corresponding to a typical size of 26 nm. This increase in lengthscale for a lower concentration suggests an alternative hypothesis for the origin of this lengthscale in the model. In a water/water system, a reduction in tie line length results in a broader interface, as Vis et al. showed theoretically [109], and Aarts et al. showed experimentally with a demixing polymer/colloid system [3]. This increase in our typical pinning size for a decrease in tie line length is consistent with this, suggesting that the minimum hop length of the interface due to pinning is given by its width.

To account for the large T_D we measure, we suggest one possible hypothesis: the adsorption of gelatin at the contact line may increase the local fish gelatin concentration, and hence the bulk viscosity μ, which scales with a power law in concentration. Indeed then from Stokes, $T_D = 6\pi R\mu/\gamma$. At the scale of several nanometres, adsorption of gelatin may strongly increase the viscosity and increase T_D, as illustrated in Figure 10.15. Far from the particle, the polymer concentration c_{far} would vary as shown from theory in Section 4.2.3. However, close to the particle surface the gelatin concentration c_{near} would be much higher in the gelatin-rich phase. Elastic behaviour should not be responsible as fish gelatin remains Newtonian at high concentrations.

However, one open question concerns the fact the fact that the gelatin solution is likely sufficiently concentrated to be the semi-dilute regime, meaning it will be entangled. As a result, the

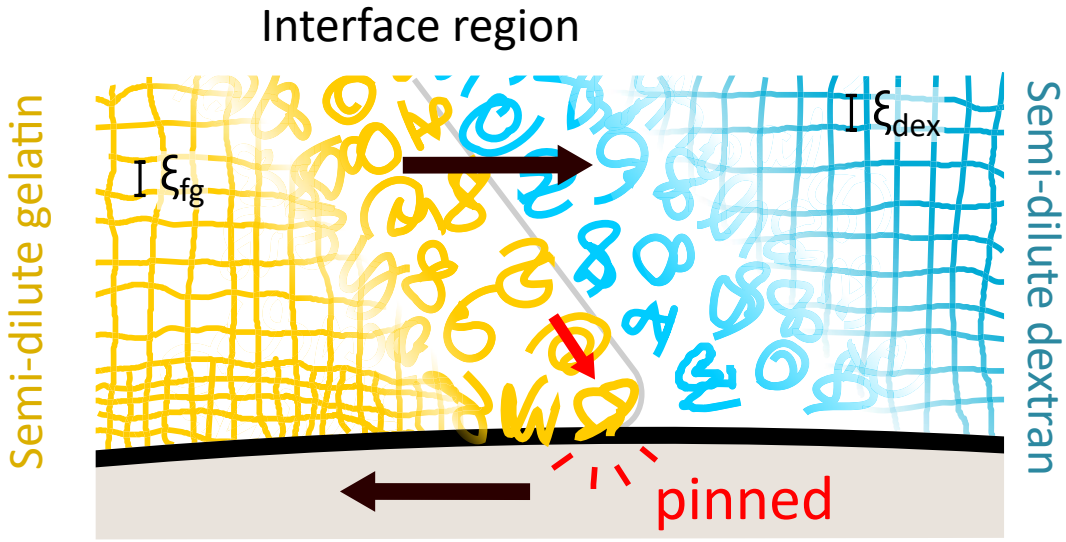

Figure 10.15: Hypothesis explaining the origin of pinning of the advancing contact line between the fish-gelatin-rich phase and the dextran-rich phase. Polymers shown as individual polymers in the depleted zone near the interface, and as a semidilute mesh of size ξ_{fg} and ξ_{dex} further from the interface. Fish gelatin at the interface adsorbs onto the surface of the particle as the dextran phase recedes. This adsorption pins the contact line as the molecule can no longer move across the particle surface. This is analogous to molecular kinetic wetting theories for oil/water or air/water contact line pinning, with polymers acting like solvent molecules.
Close to the particle surface in the fish-gelatin-rich phase, adsorption increases the concentration locally, decreasing the mesh size ξ_{fg}.

typical relevant length scale for the particles' interaction with the polymer is the correlation length ξ_{fg}, which is much smaller than the size of the polymer molecules, or the lengthscale given by our logarithmic behaviour. Though it is worth noting that in the region of the interface local polymer concentration is lower, so individual polymers may play a role here.

In spite of the slow exponential dynamics, it is clear with reference to any plotted particle trajectory (for instance Figure 10.12) that the overall dynamics of adsorption and relaxation are in fact much faster in the water/water system than the oil/water system due to the much reduced role of pinning at low surface tension. Although a transition to a logarithmic regime is indeed visible, its timescale is much faster due to a small pinning potential ΔU. The typical time to approach equilibrium of a 4 µm particle in the water/water system is on the order of 10 seconds. For a 10 µm equilibrium may still be reached in less than 100 seconds. This is drastically faster than the near-equilibrium motion of particles at the oil/water interface, which may take days to reach their equilibrium contact angle.

Conclusions

In Part III, we have demonstrated that although spherical colloidal particles are poor emulsion stabilisers for aqueous two-phase systems (ATPSs), they can reveal much as model particles about the dynamics and behaviour of colloidal particles within these systems.

In Chapter 8, we demonstrated that particles in a fish gelatin/dextran system invariably have a strong preference for the fish gelatin phase. We showed fish gelatin adsorbs to the particles in large quantities irrespective of surface charge due most likely to the hydrophobic interaction, and that dextran does not adsorb. We also showed that this adsorption can drive spontaneous capillary-driven aggregation of particles dispersed in a dextran-rich phase in contact with a fish-gelatin-rich phase through interdiffusion of the two polymer phases, though that addition of salt stops this interdiffusion.

Chapter 9 explored the ability of a variety of spherical colloidal particles to stabilise a fish gelatin/dextran system, varying the pH from acidic (5.8) to alkali (pH 10.2), the emulsification method (stirring vs. shaking vs. Ultra-Turrax), the particle size (from 0.4 µm to 1.5 µm), and the particle surface chemistry, though ultimately we conclude that within these conditions stabilisation is not possible. Spherical particles however are an excellent candidate as a model system to study colloidal dynamics within these systems.

In Chapter 10, we have demonstrated that the dynamics of spherical colloidal particles adsorbing to a model interface in an aqueous two-phase system (ATPS) can be tracked with confocal microscopy. The resulting trajectories show two regimes of motion - firstly a fast exponential snap-in phase, and secondly a slower logarithmic relaxation. This is consistent with published experimental and theoretical results for the oil/water interface [21,62,90,117]. In these works, the transition from exponential to logarithmic relaxation marks a point where the capillary force driving the particle towards equilibrium becomes weak compared to the energy required for the contact line to overcome surface defects, and thermally activated hopping of the contact line dominates.

This work is remarkable however in being the first time the exponential regime of the adsorption trajectory has been captured with particle tracking techniques, given that in an oil/water system, the large surface tension makes this part of the motion orders of magnitude faster. We observed that the characteristic time of this motion was an order of magnitude slower than that expected from a balance of Stokes drag and capillary forces, but that it scales as expected with the particle radius. We saw little influence of the salt content, or the polymer concentration.

Additionally, in applying the model of Colosqui et al. to the logarithmic relaxation to equilibrium due to surface defects, we found that a good fit was found for defects of area $\sim 400\,\mathrm{nm}^2$, the order of the polymer size. We tentatively suggest that adsorption of polymer onto the particle surfaces at the contact line causes this pinning, though other phenomena could be at play. The pinning

energies found were typically of order $1 - 4k_{\mathrm{B}}T$. This is consistent with the low surface tension of the system, and scaled appropriately when the surface tension was increased.

Commenting now on the timescales involved for adsorption of colloidal particles in the fish gelatin/dextran system, we found that despite the slow exponential dynamics, the low pinning energy of the low surface tension system lead to much faster relaxation dynamics than at the oil/water interface, with particles as large as 10 µm expected to reach their equilibrium positions in around a minute or less. In conclusion therefore, we can propose that particles at fish gelatin/dextran interfaces do experience pinning, but to a lesser extent than at oil/water interfaces.

Part IV

Conclusions and Perspectives

Conclusions and Perspectives

Microgels in thin liquid films

In the first part of this thesis, we investigated the drainage dynamics of thin liquid foam films stabilised by microgels using the thin film balance setup. We found that the conformation of microgels, and similarly their packing state at the interface, could be calculated from the thickness of the thin film. By examining different microgel concentrations, we discovered that irrespective of the time allowed for adsorption, a low concentration of microgels lead to microgels being spread at the interface. Conversely, a high concentration of microgels lead to a dense, thick layer of slightly compressed microgels. Comparing microgels of different crosslinking density, we found that the hard microgels both spread and compress slightly less than soft microgels.

Further, we were able to measure the adhesion between films, which gives an indication of the extent of bridging between the interfaces. Again both crosslinking density and concentration had an influence upon this - at high concentrations adhesion and bridging were seldom observed, indicating that a compressed bilayer of microgels was formed. At higher crosslinking density though bridging was sometimes still observed. At low concentration both crosslinking densities made adhesive films, though by measuring the contact angle in the plateau border we demonstrated that the hard microgel films are more adhesive.

The final observation we highlight is the development in low concentration films of hard microgels of extremely thin zones, entirely depleted of microgels. These zones, only a hundred nanometres thick, represent a fairly extreme form of bridging, and may be responsible in part for the poor mechanical stability of emulsions formed from hard microgels.

Overall, our work was very consistent with the results of studies into emulsions stabilised by microgels of different cross-linking densities, reproducing the adhesive films, the increased bridging, and the poorer stability, while providing insight into the dynamic origin of these behaviours.

Perspectives

This work has shown that the thin film pressure balance is a powerful technique for studying thin liquid film dynamics in air. Exploiting the incompressibility of microgels to calculate the microgel packing at the interface based on the thickness of the film offers a very quick and easy method for measuring adsorption dynamics when compared to cryo-SEM studies of bare interfaces. This may allow a fruitful study of a greater range of microgel concentrations to gain a better understanding of

the dependence of the adsorption kinetics upon particle concentration, with the additional benefit of being able to measure adhesion within the very same films.

Although the results we obtained correspond very well to results for emulsions, a productive study would be to compare the drainage dynamics obtained when immersing the thin film balance in oil.

Particles at water/water interfaces

In the first part of this project, we attempted to stabilise a fish gelatin/dextran system with spherical colloidal particles. This was not successful due to the small contact angle the particle made with the interface, combined with the very low surface tension of such systems meaning that the shear of emulsification was enough to push particles dispersed in dextran entirely through the interface to their preferred phase, the fish gelatin. The adsorption of fish gelatin then likely rendered the particles unable to re-adsorb to the interface. This work highlights the importance of good surface coverage and of ensuring that the stabilisers are as resistant as possible to being removed from the interface by shear, which is consistent with the results of Vis et al. stabilising such systems with flat hexagonal platelets.

However, the model spherical particles are very suitable for studying adsorption dynamics at the water/water interface, which has not previously been reported. Using a model interface, confocal microscopy tracking revealed that dynamics of adsorption follow established models for adsorption at the oil/water interface. Two remarkable observations were made in comparison to the models. Firstly, the dynamics begin with a fast 'snap-in' stage which follows an exponential trajectory. This stage of dynamics was theoretically predicted but far too fast to be experimentally captured at the oil/water interface with particle tracking. Its capture demonstrates the powerful ability of water/water interfaces to act as model interfaces to observe surface-tension-driven processes that occur far too quickly to capture at the oil/water interface. In fact, the exponential decay we observe is an order of magnitude slower than that predicted. We propose one hypothesis that the adsorption of fish gelatin results in a much larger local viscosity around the particle.

Secondly, again in line with the theoretical model and experiments at the oil/water interface, a slower relaxation to the equilibrium took over in a later stage of the trajectory that was logarithmic in its decay. The theory indicates that this logarithmic relaxation is caused by pinning of the contact line on nanoscale defects on the surface of the particles, which are overcome through the thermal motion of the interface. It is remarkable that this could be observed for an interface of such low surface tension. As a fitting parameter, the size of defects for this system was revealed to be on the order of the polymer size. This suggests that although the logarithmic behaviour is the same in this system, the origin is slightly different. We hypothesise that adsorption of fish gelatin onto the particle at the contact line pins its advance, though the true origin remains an open question.

Perspectives

To explain our slow exponential dynamics, and the presence of logarithmic dynamics, in each case we propose a hypothesis based around polymer adsorption. The clear step to verify this, and to provide a more complete picture of adsorption in water/water systems, would be to observe particle

adsorption dynamics in a system chosen such that the polymer does not adsorb onto the particles. If unexpectedly slow exponential snap-in dynamics are still observed, this would be evidence that slower exponential dynamics are a general feature of particle adsorption at interfaces.

An additional important study would be to examine the adsorption dynamics of particles of different shapes. Two studies successfully stabilised water-in-water emulsions using anisotropic particles, and an understanding of adsorption dynamics and/or contact line pinning could play an important role in optimising such systems.

Appendix A

Film Refractive Index Calculation

A.1 PNiPAM Concentration

The largest difference in refractive index in the system will be between films with the highest and lowest concentration of PNiPAM monomer per unit volume. The highest concentration of monomer may occur for a 1% film of soft microgels that are highly packed, with negligible gaps between microgels in each layer. Given that the microgels are incompressible however, this concentration will be the same as that in a bulk PNiPAM gel – approximately 10% PNiPAM, 90% water. The refractive index of NiPAM at 20 °C is 1.495 [85], compared to 1.333 for water. With a linear mixing estimation, the refractive index of the total system will be 1.348.

To estimate whether there is any significant change for a real film, we examine the most extreme case. For the lowest concentration of microgels in a film, the 0.1% soft microgel films with a dimple will have microgels spread at the interfaces, a microgel layer of 400 nm in a 6000 nm film. This would result in a refractive index of 1.334 (as opposed to the 1.348 assumed). This difference of 1% is smaller than other experimental errors for dimple size calculations.

Real films will seldom have a pure water filled region during the period of drainage we are interested in, hence the refractive index will only vary minutely from the maximum value offered above.

A.2 Wavelength dependency

The interferometric measurement of thickness used in this study relies upon precise measurement of wavelength. Therefore the wavelength dependence of the refractive index of the water in the system is more important for accurate analysis than the negligible microgel concentration dependence. This is accounted for in the MATLAB analysis script used to find thicknesses. The temperature of water was taken as 21.5 °C, and the values for the refractive index were taken from Reference [23].

Appendix B

Microgel Counting

To understand the conformation of microgels in the system, such as their packing state at the interface, we must know how many microgels are present. Since microgels are very difficult to observe directly within an air/water/air thin film, we must use various geometrical arguments to put limits on their number.

The maximum number of microgels accessible to the thin film is determined by the volume of the thick film formed at the beginning of the experiment, as shown in Figure B.1. The volume within a radius of $w = 0.5\,\text{mm}$ from the centre is taken as accessible to the film, whose final radius is invariably 0.4 mm.

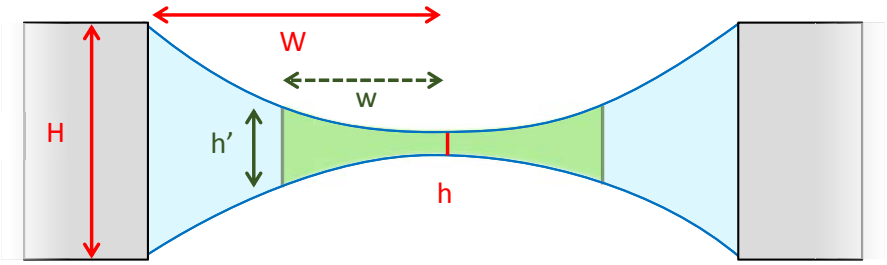

Figure B.1: Cross-section of thick initial film, modelled as two spherical caps. Volume considered in film particle counting shown in green. W is the width of the film holder, and H is its height. w is the width of the volume considered in the calculation. h is the central thickness of the film, and h' is its thickness at the edge of the volume considered.

B.1 Geometry

Assuming the film to have to form of a spherical cap. Volume of spherical cap of width $2w$ and height $\frac{1}{2}(h' - h)$

$$V_C = \pi \frac{h' - h}{12} \left(3w^2 + \frac{1}{4}(h' - h)^2 \right) \tag{B.1}$$

Total volume of the film section shown:

$$V = \pi w^2 h' - 2V_C \tag{B.2}$$

The result from measured and stated values for the total volume of the film: $V = 1.05 \times 10^{-10}\,\mathrm{m}^3$.

To calculate the surface area of film, it is simply the sum of two spherical caps:

$$S = 2\pi\left(\frac{1}{4}(h' - h)^2 + w^2\right) \tag{B.3}$$

The result for the surface area of the film is then: $S = 1.62 \times 10^{-6}\,\mathrm{m}^2$

B.2 Microgel Counting: Thick Film

The number of microgels per unit volume was measured at 0.01%wt concentration using fluorescent microgels in a confocal microscope, and is given by $n_{0.01} = 1.76 \times 10^{16}\,\mathrm{m}^{-3}$. Table B.1 shows the number of microgels within the film if all microgels within the volume were to diffuse to the surface and adsorb within the allotted time, calculated by multiplying the particles per unit volume to the volume of the thick film shown above.

B.3 Microgel Counting: Thin Film

As the microgels are incompressible, and microgels are not observed being ejected from the film upon application of pressure, the volume of the thin film cannot be smaller than the volume of microgels adsorbed to the thick film before the application of pressure. This puts an upper bound on the surface packing at each concentration. Assuming perfect packing with no gaps, the maximum number of microgels of radius R, per unit area of thin film with thickness t is given by

$$N_{\max} = \frac{t}{\frac{4}{3}\pi R^3} \tag{B.4}$$

Where t is, for 1.5% BIS microgels, 1200 nm at 1.0%wt concentration and 350 nm and 0.1%wt. For 5% BIS microgels, t is 900 nm at 1.0%wt concentration, and 400 nm at 0.1% concentration. However, due to the later formation of depleted zones thinning the film in the 5%BIS case, 400 nm may be an overestimation. Multiplying $N_{\max}$ by the area of the film gives the maximum number of microgels adsorbed to the surfaces of the film before pressure is applied, according to conservation of volume. If this number is smaller than the number in the thick film calculated above, then not all microgels in the film adsorb to the surfaces.

B.4 Microgel Counting: Film Surface

The minimum number of microgels on the surface required to reach a given compression state can be calculated as follows, assuming microgels pack as close-packed hexagons:

$$N_S = \frac{S}{\pi R^2} \times \text{layers} \tag{B.5}$$

S is the surface area of the system given above. R represents microgel radius at surface for the given compression state, which for 1.5% BIS microgels (hydrodynamic radius 385 nm) is taken as 600 nm for spread conformation and 385 nm for compressed conformation. For 5% BIS microgels

(hydrodynamic radius 325 nm), the R is taken as 500 nm for the spread state and 325 nm for the compressed state. 'layers' represents monolayer or bilayer, = 1 or 2 respectively.

B.5 Comparison

Table B.1: Comparison of the number of microgels in the system at each concentration to the number required at the interface for each compression state.

Crosslinker	Total Microgels Available		Microgels in thin film of radius 0.5 mm	
(mol%)	1%	0.1%	1%	0.1%
1.5	1.85×10^8	1.85×10^7	3.94×10^6	1.15×10^6
5	1.85×10^8	1.85×10^7	4.92×10^6	2.18×10^6
Crosslinker	Microgels Required Flattened		Microgels Required Compressed	
(mol%)	Monolayer	Bilayer	Monolayer	Bilayer
1.5	1.30×10^6	2.59×10^6	3.15×10^6	6.29×10^6
5	1.82×10^6	3.64×10^6	4.42×10^6	8.83×10^6

Table B.1 demonstrates that the surface concentrations are different for the two concentrations, and for the different cross-linking densities, showing adsorption kinetics influence packing density. At 0.1%, the number of microgels in the thin film is slightly less than the number in a flattened monolayer with microgels radii 500 nm. Hence the microgels are highly flattened to beyond this radius. At 1.0%, the number of microgels in the thin film is not quite enough for a full compressed bilayer. However, if on a single interface there are small gaps between compressed microgels due to circle packing, this would lower the number of microgels required for microgels to compress.

Appendix C

Total Organic Carbon Calibration

Figures C.1 and C.2 show calibration curves created through measuring the carbon content of a range of concentrations of polymer solution with Total Organic Carbon measurements. Through these curves, carbon content measurements can be converted to weight% concentration values. The measured Area is demonstrably linear with the polymer concentration in both cases.

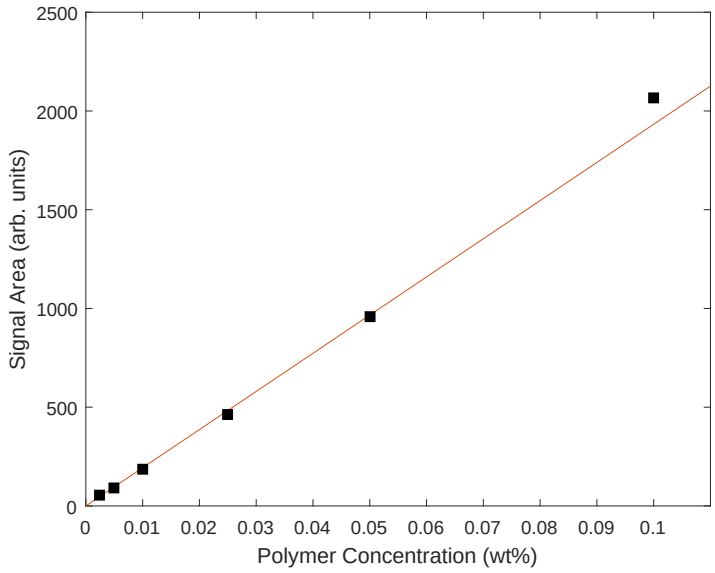

Figure C.1: Calibration curve for Total Organic Carbon measurements of dextran concentration.

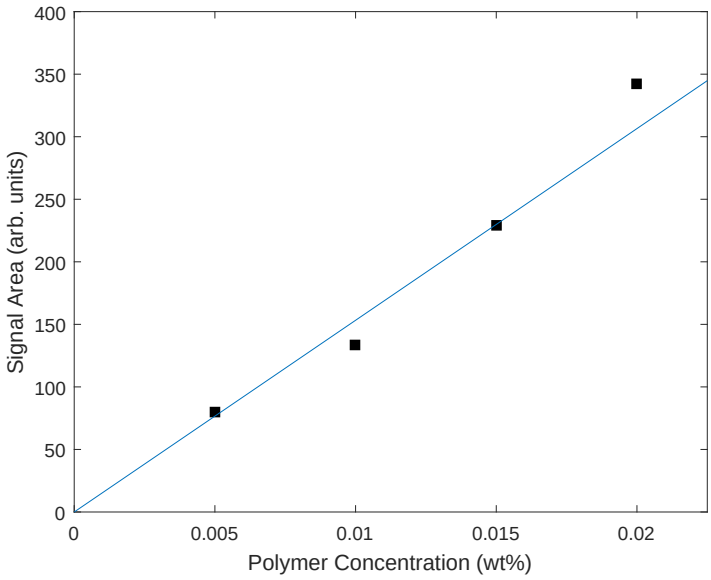

Figure C.2: Calibration curve for Total Organic Carbon measurements of fish gelatin concentration.

List of Figures

List of Tables

Bibliography

[1] D G a L Aarts and H N W Lekkerkerker. Confocal scanning laser microscopy on fluid–fluid demixing colloid–polymer mixtures. *Journal of Physics: Condensed Matter*, 16(38):S4231–S4242, 2004. 49, 51, 53, 151

[2] Dirk G A L Aarts and Henk N. W. Lekkerkerker. Droplet coalescence: drainage, film rupture and neck growth in ultralow interfacial tension systems. *Journal of Fluid Mechanics*, 606:275–294, 2008. 117

[3] Dirk G a L Aarts, Matthias Schmidt, and Henk N W Lekkerkerker. Direct visual observation of thermal capillary waves. *Science (New York, N.Y.)*, 304(5672):847–850, 2004. 9, 49, 50, 135, 151

[4] S. Arditty, C. P. Whitby, B. P. Binks, V. Schmitt, and F. Leal-Calderon. Some general features of limited coalescence in solid-stabilized emulsions. *European Physical Journal E*, 11(3):273–281, 2003. 26, 150

[5] Sho Asakura and Fumio Oosawa. Surface Tension of High-Polymer Solutions On Interaction between Two Bodies Immersed in a Splution of Macromolecules. *The Journal of Chemical Physics*, 22(May 2016):1255–1256, 1954. 48

[6] Stuart G Ash, Douglas H Everett, and Clay Radke. Thermodynamics of the effects of adsorption on interparticle forces. *Journal of the Chemical Society, Faraday Transactions 2: Molecular and Chemical Physics*, 69:1256–1277, 1973. 16

[7] N P Ashby and B P Binks. Pickering emulsions stabilised by Laponite clay particles. *Physical Chemistry Chemical Physics*, 2(24):5640–5646, 2000. 27

[8] Phil Attard, D John Mitchell, and Barry W Ninham. Beyond Poisson–Boltzmann: images and correlations in the electric double layer. I. Counterions only. *The Journal of chemical physics*, 88(8):4987–4996, 1988. 16

[9] Phil Attard, D John Mitchell, and Barry W Ninham. Beyond Poisson–Boltzmann: Images and correlations in the electric double layer. II. Symmetric electrolyte. *The Journal of chemical physics*, 89(7):4358–4367, 1988. 16

[10] Gireeshkumar Balakrishnan, Taco Nicolai, Lazhar Benyahia, and Dominique Durand. Particles trapped at the droplet interface in water-in-water emulsions. *Langmuir*, 28(14):5921–5926, 2012. 56

[11] V. Bergeron and C. Radke. Equilibrium Measurements of Oscillatory Disjoining Pressures in Aqueous Foam Films. *Langmuir*, 1(19):3020–3026, 1992. 18

[12] Vance Bergeron. Forces and structure in thin liquid soap films. *J. Phys. Condens. Matter*, 11(19):R215–R238, 1999. 17, 18, 19, 150

[13] Bastian Brugger, Brian a. Rosen, and Walter Richtering. Microgels as stimuli-responsive stabilizers for emulsions. *Langmuir*, 24(21):12202–12208, 2008. 38

[14] Bastian Brugger, Stephan Rütten, Kim Ho Phan, Martin Moller, and Walter Richtering. The colloidal suprastructure of smart microgels at oil- Water interfaces. *Angewandte Chemie - International Edition*, 48(22):3978–3981, 2009. 38

[15] Bastian Brugger, Jan Vermant, and Walter Richtering. Interfacial layers of stimuli-responsive poly-(N-isopropylacrylamide-co-methacrylicacid) (PNIPAM-co-MAA) microgels characterized by interfacial rheology and compression isotherms. *Physical chemistry chemical physics : PCCP*, 12(43):14573–8, 2010. 38, 41

[16] S. Cappelli, Q. Xie, J. Harting, A. M. de Jong, and M. W J Prins. Dynamic wetting: Status and prospective of single particle based experiments and simulations. *New Biotechnology*, 32(5):420–432, 2015. 85

[17] Longquan Chen, Lars-Oliver Heim, Dmytro S. Golovko, and Elmar Bonaccurso. Snap-in dynamics of single particles to water drops. *Applied Physics Letters*, 101(2012):031601, 2012. 31, 150

[18] Benjamin Chu and Peter Josef William Debye. *Molecular forces: Based on the Baker lectures of Peter JW Debye*. Interscience Publishers, 1967. 16

[19] John H Clint and Spencer E Taylor. Particle size and interparticle forces of overbased detergents: a Langmuir trough study. *Colloids and surfaces*, 65(1):61–67, 1992. 94

[20] Yann Cohin, Maelle Fisson, Kévin Jourde, Gerald G. Fuller, Nicolas Sanson, Laurence Talini, and Cécile Monteux. Tracking the interfacial dynamics of PNiPAM soft microgels particles adsorbed at the air-water interface and in thin liquid films. *Rheologica Acta*, 52(5):445–454, 2013. 38, 40, 71, 73, 75

[21] Carlos E. Colosqui, Jeffrey F. Morris, and Joel Koplik. Colloidal adsorption at fluid interfaces: Regime crossover from fast relaxation to physical aging. *Physical Review Letters*, 111(2):1–5, 2013. 34, 35, 36, 85, 118, 126, 127, 131, 137, 150, 153

[22] R G Cox. The dynamics of the spreading of liquids on a solid surface. Part 1. Viscous flow. *Journal of Fluid Mechanics*, 168:169–194, 1986. 33

[23] Masahiko Daimon and Akira Masumura. Measurement of the refractive index of distilled water from the near-infrared region to the ultraviolet region. *Applied optics*, 46(18):3811–3820, 2007. 68, 144

[24] Rilton A. de Freitas, Taco Nicolai, Christophe Chassenieux, and Lazhar Benyahia. Stabilization of Water-in-Water Emulsions by Polysaccharide-Coated Protein Particles. *Langmuir*, 32(5):1227–1232, feb 2016. 47, 57

[25] Didi Derks, Dirk G A L Aarts, Daniel Bonn, Henk N W Lekkerkerker, and Arnout Imhof. Suppression of thermally excited capillary waves by shear flow. *Physical Review Letters*, 97(3):1–4, 2006. 9, 49

[26] Omkar S. Deshmukh, Dirk van den Ende, Martien Cohen Stuart, Frieder Mugele, and Michel H.G. Duits. Hard and soft colloids at fluid interfaces: Adsorption, interactions, assembly & rheology. *Advances in Colloid and Interface Science*, 222:215–227, 2015. 38

[27] Omkar Suresh Deshmukh, Armando Maestro, Michel .H.G. Duits, Dirk van den Ende, Martien a Cohen-Stuart, and Frieder Mugele. Equation of state and adsorption dynamics of soft microgel particles at air-water interface. *Soft Matter*, 9:2731–2738, 2014. 38, 40

[28] Mathieu Destribats, Mayalen Eyharts, Véronique Lapeyre, Elisabeth Sellier, Imre Varga, Valérie Ravaine, and Véronique Schmitt. Impact of pNIPAM microgel size on its ability to stabilize pickering emulsions. *Langmuir*, 30(7):1768–1777, 2014. 41

[29] Mathieu Destribats, Véronique Lapeyre, Elisabeth Sellier, Fernando Leal-Calderon, Valérie Ravaine, and Véronique Schmitt. Origin and control of adhesion between emulsion drops stabilized by thermally sensitive soft colloidal particles. *Langmuir*, 28(8):3744–3755, 2012. 8, 38, 41, 42, 71, 75, 82, 151

[30] Mathieu Destribats, Véronique Lapeyre, Mélanie Wolfs, Elisabeth Sellier, Fernando Leal-Calderon, Valérie Ravaine, and Véronique Schmitt. Soft microgels as Pickering emulsion stabilisers: role of particle deformability. *Soft Matter*, 7(17):7689, 2011. 8, 38, 39, 64, 65, 150

[31] Mathieu Destribats, Mélanie Wolfs, Florent Pinaud, Véronique Lapeyre, Elisabeth Sellier, Véronique Schmitt, and Valérie Ravaine. Pickering emulsions stabilized by soft microgels: Influence of the emulsification process on particle interfacial organization and emulsion properties. *Langmuir*, 29(40):12367–12374, 2013. 38

[32] Daniel C Dewey, Christopher a Strulson, David N Cacace, Philip C Bevilacqua, and Christine D Keating. Bioreactor droplets from liposome-stabilized all-aqueous emulsions. *Nat. Commun.*, 5(May):4670, 2014. 56, 57, 85

[33] Marijke W. Edelman, Erik Van Der Linden, and R. Hans Tromp. Phase separation of aqueous mixtures of poly(ethylene oxide) and dextran. *Macromolecules*, 36(20):7783–7790, 2003. 47

[34] Jan Christer Eriksson and Borislav V. Toshev. Disjoining pressure in soap film thermodynamics. *Colloids and Surfaces*, 5(3):241–264, 1982. 16

[35] Philip Finkle, Hal D Draper, and Joel H Hildebrand. The theory of emulsification1. *Journal of the American Chemical Society*, 45(12):2780–2788, 1923. 26

[36] Hassan Firoozmand, Brent S. Murray, and Eric Dickinson. Interfacial structuring in a phase-separating mixed biopolymer solution containing colloidal particles. *Langmuir*, 25(3):1300–1305, 2009. 56

[37] D. Forciniti, C.K. Hall, and M.-R. Kula. Influence of polymer molecular weight and temperature on phase composition in aqueous two-phase systems. *Fluid Phase Equilibria*, 61(3):243–262, 1991. 47

[38] EXW Foxboro. Conductivity Ordering Guide, 1999. 87

[39] David J. French, Phil Taylor, Jeff Fowler, and Paul S. Clegg. Making and breaking bridges in a Pickering emulsion. *Journal of Colloid and Interface Science*, 441:30–38, 2015. 27, 82

[40] Stefan Frijters, Florian Günther, and Jens Harting. Effects of nanoparticles and surfactant on droplets in shear flow. *Soft Matter*, 8(24):6542, 2012. 27, 28, 150

[41] Karen Geisel, Katja Henzler, Peter Guttmann, and Walter Richtering. New insight into microgel-stabilized emulsions using transmission X-ray microscopy: Nonuniform deformation and arrangement of microgels at liquid interfaces. *Langmuir*, 31(1):83–89, 2015. 38

[42] Karen Geisel, Lucio Isa, and Walter Richtering. Unraveling the 3D localization and deformation of responsive microgels at oil/water interfaces: A step forward in understanding soft emulsion stabilizers. *Langmuir*, 28(45):15770–15776, 2012. 38, 40, 150

[43] Karen Geisel, Lucio Isa, and Walter Richtering. The compressibility of ph-sensitive microgels at the oil-water interface: Higher charge leads to less repulsion. *Angewandte Chemie - International Edition*, 53(19):4905–4909, 2014. 40

[44] Karen Geisel, Walter Richtering, and Lucio Isa. Highly Ordered 2D Microgel Arrays: Compression versus Self-Assembly. *Soft Matter*, 10:7968–7976, 2014. 38, 80

[45] Karen Geisel, Andrey A. Rudov, Igor I. Potemkin, and Walter Richtering. Hollow and Core-Shell Microgels at Oil-Water Interfaces: Spreading of Soft Particles Reduces the Compressibility of the Monolayer. *Langmuir*, 31(48):13145–13154, 2015. 41, 81

[46] R F Giese, P M Costanzo, and C J Van Oss. The surface free energies of talc and pyrophyllite. *Physics and Chemistry of Minerals*, 17(7):611–616, 1991. 94

[47] V.Ya. Grinberg and V.B. Tolstoguzov. Thermodynamic incompatibility of proteins and polysaccharides in solutions. *Food Hydrocolloids*, 11(2):145–158, 1997. 47

[48] Asen Hadjiiski, Roumiana Dimova, Nikolai D Denkov, Ivan B Ivanov, and Rajendra Borwankar. Film trapping technique: precise method for three-phase contact angle determination of solid and fluid particles of micrometer size. *Langmuir*, 12(26):6665–6675, 1996. 94

[49] H C Hamaker. The London—van der Waals attraction between spherical particles. *physica*, 4(10):1058–1072, 1937. 17

[50] Tomohito Hanazawa and Brent S. Murray. Effect of oil droplets and their solid/liquid composition on the phase separation of protein-polysaccharide mixtures. *Langmuir*, 29(31):9841–9848, 2013. 57

[51] Arjan S Heeres, Carolina S F Picone, Luuk A M van der Wielen, Rosiane L Cunha, and Maria C Cuellar. Microbial advanced biofuels production: overcoming emulsification challenges for large-scale operation. *Trends in biotechnology*, 32(4):221–9, apr 2014. 25, 150

[52] Man hin Kwok and To Ngai. A confocal microscopy study of micron-sized poly(N-isopropylacrylamide) microgel particles at the oil-water interface and anisotopic flattening of highly swollen microgel. *Journal of Colloid and Interface Science*, 461:409–418, 2016. 38

[53] Shilin Huang, Kornelia Gawlitza, Regine von Klitzing, Laurent Gilson, Johannes Nowak, Stefan Odenbach, Werner Steffen, and Günter K. Auernhammer. Microgels at the water/oil interface: In-situ observation of structural ageing and two-dimensional magnetic bead microrheology. *Langmuir*, page acs.langmuir.5b01438, 2015. 40, 75

[54] Robert J Hunter. Foundations of colloid science, vol. I. *vol II*, pages 992–1052, 1987. 17

[55] Ivan Ivanov. *Thin liquid films*, volume 29. CRC Press, 1988. 71

[56] E. A G Jamie, R. P A Dullens, and D. G A L Aarts. Surface effects on the demixing of colloid-polymer systems. *Journal of Physical Chemistry B*, 115(45):13168–13174, 2011. 49

[57] E. A G Jamie, R. P A Dullens, and D. G A L Aarts. Tuning the demixing of colloid–polymer systems through the dispersing solvent. *Journal of Physics: Condensed Matter*, 23(19):194115, may 2011. 48, 49

[58] E. A G Jamie, R. P A Dullens, and D. G A L Aarts. Spinodal decomposition of a confined colloid-polymer system. *Journal of Chemical Physics*, 137(20), 2012. 48, 49

[59] Jean-Luc Joye, George J. Hirasak, and Clarence a. Miller. Asymmetric Drainage in Foam Films N4.1. *MRS Proceedings*, 366(20):3174–3179, 1994. 69, 72, 81

[60] Jean Luc Joye, George J Hirasaki, and Clarence a Miller. Dimple formation and behavior during axisymmetrical foam film drainage. *Langmuir*, 8(12):3083–3092, 1992. 69, 72, 81

[61] Jean-Luc Joye, George J. Hirasaki, and Clarence A. Miller. Numerical Simulation of Instability Causing Asymmetric Drainage in Foam Films. *Journal of Colloid and Interface Science*, 177(2):542–552, feb 1996. 22

[62] David M. Kaz, Ryan McGorty, Madhav Mani, Michael P. Brenner, and Vinothan N. Manoharan. Physical ageing of the contact line on colloidal particles at liquid interfaces. *Nature Materials*, 11(2):138–142, 2011. 9, 30, 85, 118, 125, 127, 131, 132, 137, 150, 153

[63] Louis Keal, Véronique Lapeyre, Valérie Ravaine, Véronique Schmitt, and Cécile Monteux. Drainage dynamics of thin liquid foam films containing soft PNiPAM microgels: influence of the cross-linking density and concentration. *Soft Matter*, 2016. 64

[64] H.A. Kramers. Brownian motion in a field of force and the diffusion model of chemical reactions. *Physica*, 7(4):284–304, apr 1940. 36

[65] Peter R Lang and Yi Liu, editors. *Soft Matter at Aqueous Interfaces*. Lecture Notes in Physics. Springer, 2016. 45, 48

[66] H. N W Lekkerkerker, V. W A De Villeneuve, J. W J De Folter, M. Schmidt, Y. Hennequin, D. Bonn, J. O. Indekeu, and D. G A L Aarts. Life at ultralow interfacial tension: Wetting, waves and droplets in demixed colloid-polymer mixtures. *European Physical Journal B*, 64(3-4):341–347, 2008. 48, 151

[67] Zifu Li, Karen Geisel, Walter Richtering, and To Ngai. Poly(N-isopropylacrylamide) microgels at the oil–water interface: adsorption kinetics. *Soft Matter*, 9(41):9939, 2013. 40

[68] Zifu Li, Walter Richtering, and To Ngai. Poly(N-isopropylacrylamide) microgels at the oil–water interface: temperature effect. *Soft Matter*, 10(33):6182, jun 2014. 38

[69] E. M. Lifshitz. The Theory of Molecular Attractive Forces between Solids. *Soviet Physics*, 2(1):73–83, 1956. 17

[70] Emil Manev, Roumen Tsekov, and Boryan Radoev. Effect of thickness non-homogeneity on the kinetic behaviour of microscopic foam film. *Journal of Dispersion Science and Technology*, 18(6-7):769–788, 1997. 22

[71] Pascal Massé, Elisabeth Sellier, Véronique Schmitt, and Valérie Ravaine. Impact of electrostatics on the adsorption of microgels at the interface of pickering emulsions. *Langmuir*, 30(49):14745–14756, 2014. 38

[72] Hadi Mehrabian, Jens Harting, and Jacco H. Snoeijer. Soft particles at a fluid interface. *Soft Matter*, 12:1–17, 2016. 38

[73] James Mingins and Alexei Scheludko. Attachment of spherical particles to the surface of a pendant drop and the tension of the wetting perimeter. *Journal of the Chemical Society, Faraday Transactions 1: Physical Chemistry in Condensed Phases*, 75:1–6, 1979. 94

[74] Hélène Monteillet, Marcel Workamp, Jeroen Appel, J. Mieke Kleijn, Frans A. M. Leermakers, and Joris Sprakel. Ultrastrong Anchoring Yet Barrier-Free Adsorption of Composite Microgels at Liquid Interfaces. *Advanced Materials Interfaces*, 1(7):n/a–n/a, oct 2014. 38

[75] Cécile Monteux, Gerald G Fuller, and Vance Bergeron. Shear and dilational surface rheology of oppositely charged polyelectrolyte/surfactant microgels adsorbed at the air-water interface. Influence on foam stability. *The Journal of Physical Chemistry B*, 108(42):16473–16482, 2004. 27

[76] Cécile Monteux, Claire Marliére, Pauline Paris, Nadège Pantoustier, Nicolas Sanson, and Patrick Perrin. Poly(N-isopropylacrylamide) microgels at the oil-water interface: Interfacial properties as a function of temperature. *Langmuir*, 26(17):13839–13846, 2010. 38

[77] Karol J Mysels and Malcolm N Jones. Direct measurement of the variation of double-layer repulsion with distance. *Discussions of the Faraday Society*, 42:42–50, 1966. 18, 65

[78] To Ngai, Helmut Auweter, and Sven Holger Behrens. Environmental responsiveness of microgel particles and particle-stabilized emulsions. *Macromolecules*, 39(23):8171–8177, 2006. 38, 64

[79] To Ngai, Sven Holger Behrens, and Helmut Auweter. Novel emulsions stabilized by pH and temperature sensitive microgels. *Chemical communications (Cambridge, England)*, (3):331–333, 2005. 38

[80] Bach T. Nguyen, Taco Nicolai, and Lazhar Benyahia. Stabilization of water-in-water emulsions by addition of protein particles. *Langmuir*, 29(34):10658–10664, 2013. 56, 57, 151

[81] Bach T. Nguyen, Wenkai Wang, Brian R. Saunders, Lazhar Benyahia, and Taco Nicolai. pH-responsive water-in-water pickering emulsions. *Langmuir*, 31(12):3605–3611, 2015. 8

[82] K. N. Nordstrom, E. Verneuil, W. G. Ellenbroek, T. C. Lubensky, J. P. Gollub, and D. J. Durian. Centrifugal compression of soft particle packings: Theory and experiment. *Physical Review E - Statistical, Nonlinear, and Soft Matter Physics*, 82(4):1–8, 2010. 68, 78

[83] Bum Jun Park, Daeyeon Lee, and Eric M. Furst. *CHAPTER 2. Interactions and Conformations of Particles at Fluid-Fluid Interfaces*. Number 3. 2015. 24, 150

[84] Karthik R. Peddireddy, Taco Nicolai, Lazhar Benyahia, and Isabelle Capron. Stabilization of Water-in-Water Emulsions by Nanorods. *ACS Macro Letters*, 5(3):283–286, 2016. 59, 60, 151

[85] Martine Philipp, Ralitsa Aleksandrova, Ulrich Müller, Martin Ostermeyer, Roland Sanctuary, Peter Müller-Buschbaum, and Jan K Krüger. Molecular versus macroscopic perspective on the demixing transition of aqueous PNIPAM solutions by studying the dual character of the refractive index. *Soft matter*, 10(37):7297–7305, 2014. 68, 144

[86] Spencer Umfreville Pickering. CXCVI.—emulsions. *Journal of the Chemical Society, Transactions*, 91:2001–2021, 1907. 7, 23

[87] Florent Pinaud, Karen Geisel, P Massé, Bogdan Catargi, Lucio Isa, Walter Richtering, Valérie Ravaine, and Véronique Schmitt. Adsorption of microgels at an oil-water interface: correlation between packing and 2D elasticity. *Soft Matter*, 10:6963–6974, 2014. 38, 40, 41, 68, 80, 81, 150

[88] Markus Preuss and Hans-Jürgen Butt. Measuring the contact angle of individual colloidal particles. *Journal of colloid and interface science*, 208(2):468–477, 1998. 94

[89] Boryan P. Radoev, Alexei D. Scheludko, and Emil D. Manev. Critical thickness of thin liquid films: Theory and experiment. *Journal of Colloid And Interface Science*, 95(1):254–265, 1983. 22

[90] Amir M. Rahmani, Anna Wang, Vinothan N. Manoharan, and Carlos E. Colosqui. Colloidal particle adsorption at liquid interfaces: Capillary driven dynamics and thermally activated kinetics. page 8, 2016. 36, 37, 127, 129, 137, 154

[91] W Ramsden. Separation of Solids in the Surface-Layers of Solutions and'Suspensions'(Observations on Surface-Membranes, Bubbles, Emulsions, and Mechanical Coagulation).–Preliminary Account. *Proceedings of the royal Society of London*, 72:156–164, 1903. 7, 23

[92] Stéphane Reculusa and Serge Ravaine. Synthesis of colloidal crystals of controllable thickness through the Langmuir-Blodgett technique. *Chemistry of materials*, 15(2):598–605, 2003. 23

[93] O Reynolds. On the Theory of Lubrication and Its Application to Mr. Beauchamp Tower's Experiments, Including an Experimental Determination of the Viscosity of Olive Oil. *Philosophical Transactions of the Royal Society of London*, 177(January):157–234, 1886. 21

[94] Walter Richtering. Responsive emulsions stabilized by stimuli-sensitive microgels: Emulsions with special non-pickering properties. *Langmuir*, 28(50):17218–17229, 2012. 38, 64

[95] Michael Rubinstein and Ralph H. Colby. Polymer physics, 2003. 46, 47, 151

[96] Véronique Schmitt and Valérie Ravaine. Surface compaction versus stretching in Pickering emulsions stabilised by microgels. *Current Opinion in Colloid and Interface Science*, 18(6):532–541, 2013. 38, 41

[97] Peter R. Sperry, Harold B. Hopfenberg, and Noreen L. Thomas. Flocculation of latex by water-soluble polymers: Experimental confirmation of a nonbridging, nonadsorptive, volume-restriction mechanism. *Journal of Colloid And Interface Science*, 82(1):62–76, 1981. 48

[98] F. Spyropoulos, P. Ding, W. J. Frith, I. T. Norton, B. Wolf, and A. W. Pacek. Interfacial tension in aqueous biopolymer-surfactant mixtures. *Journal of Colloid and Interface Science*, 317(2):604–610, 2008. 53

[99] Markus Stieger, Walter Richtering, Jan Skov Pedersen, and Peter Lindner. Small-angle neutron scattering study of structural changes in temperature sensitive microgel colloids. *The Journal of chemical physics*, 120(13):6197–6206, 2004. 38, 39, 150

[100] Cosima Stubenrauch, Dimo Kashchiev, and Reinhard Strey. Phase diagrams of nonionic foam films: construction by means of disjoining pressure versus thickness curves. *Journal of colloid and interface science*, 280(1):244–255, 2004. 72

[101] Cosima Stubenrauch and Reinhard Strey. Phase diagrams of nonionic foam films: New interpretation of disjoining pressure vs thickness curves. *Langmuir*, 20(13):5185–5188, 2004. 72

[102] Robert W Style, Lucio Isa, and Eric R Dufresne. Adsorption of soft particles at fluid interfaces. *Soft Matter*, 11(ii):1–8, 2015. 38

[103] S Tcholakova, N D Denkov, and A Lips. Comparison of solid particles, globular proteins and surfactants as emulsifiers. *Physical Chemistry Chemical Physics*, 10(12):1608–1627, 2008. 26, 27

[104] Roumen Tsekov. The R(4/5)-problem in the drainage of dimpled thin liquid films. *Colloids and Surfaces A: Physicochemical and Engineering Aspects*, 141(2):161–164, 1998. 22

[105] Roumen Tsekov. Drainage of foam films. *Nato Asi Series E Applied Sciences*, 354:1–7, 1999. 22

[106] Steven Vandebril, Jan Vermant, and Paula Moldenaers. Efficiently suppressing coalescence in polymer blends using nanoparticles: role of interfacial rheology. *Soft Matter*, 6(14):3353–3362, 2010. 27

[107] R Varoqui and Ph Dejardin. Hydrodynamic thickness of adsorbed polymers. *The Journal of Chemical Physics*, 66(10):4395–4399, 1977. 104

[108] Aletta Adriana Verhoeff, Francois Lavergne, Denis Bartolo, Dirk G. a. L. Aarts, and Roel P. a. Dullens. Optical trapping of interfaces at ultra-low interfacial tension. *Soft Matter*, pages 3100–3104, 2015. 49, 50, 151

[109] Mark Vis. *Interfacial Thermodynamics of Coexisting Aqueous Polymer Solutions*. 2015. 52, 54, 55, 96, 97, 105, 135, 151, 152

[110] Mark Vis, Ben H. Erné, and Robert H. Tromp. Chemical physics of water–water interfaces. *Biointerphases*, 11(1):018904, 2016. 51

[111] Mark Vis, Joeri Opdam, Ingo S J Van 't Oor, Giuseppe Soligno, René Van Roij, R Hans Tromp, and Ben H Erné. Water-in-water emulsions stabilized by nanoplates. *ACS Macro Letters*, 4(9):965–968, 2015. 8, 58, 59, 151

[112] Mark Vis, V. F. D. Peters, R. Hans Tromp, and B. H. Erné. Donnan Potentials in Aqueous Phase Separated Polymer Mixtures. *Langmuir*, (May), 2014. 47, 53, 87, 98

[113] Mark Vis, Vincent F D Peters, Edgar M Blokhuis, Henk N W Lekkerkerker, and Ben H Ern. Effects of Electric Charge on the Interfacial Tension Between Coexisting Aqueous Mixtures of Polyelectrolyte and Neutral Polymer. pages 1–30, 2015. 47, 87

[114] Mark Vis, Vincent F. D. Peters, Edgar M. Blokhuis, Henk N. W. Lekkerkerker, Ben H. Erné, and R. Hans Tromp. Decreased Interfacial Tension of Demixed Aqueous Polymer Solutions due to Charge. *Physical Review Letters*, 115(7):078303, 2015. 47, 53, 98, 151

[115] Mark Vis, Vincent F D Peters, Ben H. Erné, and R. Hans Tromp. Ion entropy in phase-separated aqueous mixtures of polyelectrolyte and neutral polymer. *Macromolecules*, 48(8):2819–2828, 2015. 47, 52

[116] Anna Wang, David M Kaz, Ryan McGorty, and Vinothan N Manoharan. Relaxation dynamics of colloidal particles at liquid interfaces. *4th International Symposium on Slow Dynamics in Complex Systems*, 343(2013):336–343, 2013. 30, 31, 150

[117] Anna Wang, Ryan McGorty, David M. Kaz, and Vinothan N. Manoharan. Contact-line pinning controls how quickly colloidal particles equilibrate with liquid interfaces. page 24, jul 2016. 9, 33, 115, 137

[118] Boris Y Zaslavsky. *Aqueous two-phase partitioning: physical chemistry and bioanalytical applications*. CRC Press, 1994. 47

[119] Ju Zhang and Robert Pelton. Poly (N-isopropylacrylamide) Microgels at the Air-Water Interface. *Langmuir*, 15(11):8032–8036, 1999. 38, 40